Development Of Stress Analysis By Holographic Interferometry.

DEVELOPMENT OF STRESS ANALYSIS BY HOLOGRAPHIC INTERFEROMETRY

by

Paul Marie de Larminat

A Dissertation

Presented to the Graduate Committee

of Lehigh University

in Candidacy for the Degree of

Doctor of Philosophy

in

Applied Mechanics

Lehigh University

1975

Approved and recommended for acceptance as a dissertation in partial fulfillment of the requirements for the degree of Doctor of Philosophy.

February 21, 1975
(date)

R. P. Wei (Professor in Charge)

Accepted March 10, 1975
(date)

Special committee directing the doctoral work of Mr. Paul Marie de Larminat

Professor T. E. Chen, Chairman

Professor F. P. Beer

Professor E. E. Bergmann

Professor G. C. Sih

Professor R. P. Wei

A mes parents, en signe de gratitude pour la constance de leur aide materielle et morale durant toute mon education.

ACKNOWLEDGMENTS

The author gratefully acknowledges the patient guidance and instruction of his advisor, Professor Robert P. Wei. Gratitude is also expressed to the members of the author's special committee: Professor F. P. Beer, Professor E. E. Bergmann, Professor T. E. Chen and Professor G. C. Sih, for their contributions during the course of this work. The able technician support provided by Mr. C. D. Miller was very helpful and is gratefully acknowledged. The author also wishes to thank the machine shop staff for building part of the equipment.

Finally, the author acknowledges the National Science Foundation for providing his research assistantship during most of the time devoted to this study, under a Departmental Development Grant to the Department of Mechanical Engineering and Mechanics.

TABLE OF CONTENTS

LIST OF TABLES

LIST OF FIGURES

ABSTRACT

Holographic interferometry is a technique for measuring small displacements, using holographic wavefront reconstruction. It can be used for stress analysis, by measuring strain-induced displacements. Theoretically, this can be done with either reflecting or transparent specimens. However, the use of non-transparent objects is often limited by unwanted rigid body displacements of the object, induced in the loading process. These displacements can alter the fringe patterns and often cause the fringes to disappear completely. A technique of compensation for this deterioration of the fringe pattern therefore is needed and is developed in this work. It is shown that the influence of rigid-body displacements can be eliminated almost completely by translations of the hologram and by rotations of the object illumination beam. The resulting fringes are then related to strains only.

As an application of this method, the out-of-plane component of the surface displacement is measured around a circular hole in a plate loaded in tension in its plane. The experimental results are compared to those obtained theoretically from the two-dimensional generalized plane stress analysis, and from a three-dimensional analysis. Both theories give the same results away from the hole. But they differ significantly close to the hole boundary, where three-dimensional effects are induced. The experimentally measured displacement is found to be in good agreement with both theories

away from the hole. Close to the hole, a large departure from the two-dimensional analysis and good agreement with the three-dimensional theory are observed.

The results obtained by reflection holographic interferometry are then compared to the results of transmission holographic interferometry. The comparison of these results is shown to provide a measurement of the through-the-thickness average value of the normal stress σ_z. This technique is applied to the circular hole problem. The experimental results thereby obtained again match well the three-dimensional analysis, but depart from the two-dimensional one close to the hole.

The application of holographic interferometry to fracture mechanics problems is finally considered. As an example of application, the out-of-plane surface displacement is measured along the crack line extension in an aluminum single-edge cracked specimen. This result is compared to a transmission test performed on a thin plexiglas model of the aluminum sample.

CHAPTER I. INTRODUCTION

Holography is a wavefront reconstruction technique that is best known for its spectacular application to the production of three-dimensional pictures. The principle of holography was devised in 1948 by D. Gabor [1] as a way to improve electron microscopy. Because of the lack of coherent light sources, it had very little use for many years. A very strong revival of holography began in the 1960's when the first lasers were developed which provided powerful sources of highly coherent light. The first "off axis" holograms were obtained in 1962 by Leith and Upatnieks [2] initiating a considerable amount of research in this field. The possibility of using holograms as optical elements in interferometers was soon recognized. The first applications were made by Hildebrand and Haines [3] for measurements of static displacements, and Powell and Stetson [4] for vibration measurements. Holographic interferometry has also been used increasingly as a tool for stress analysis in the past few years. Most of these applications have been made with transparent materials [5,6,7]. The method has also been used with non-transparent specimens [8 to 12]. In spite of its great potential, however, the use of this technique for nontransparent objects is limited by its sensitivity to extraneous rigid body motions of the object to be studied. When a stress analysis experiment is performed, rigid body displacements of the specimen are

generally induced by the loading process. In some cases, these rigid body displacements can be much larger than the displacements produced by strains in the specimen. The data of interest (those related to strain) can then become difficult or impossible to retrieve. Rigid motion has only a minor effect when large strain-related displacements can be obtained with a relatively low driving force. One can make rigid body displacements negligible or relatively easy to take into account under this condition, through appropriate design of the loading system. Typical examples are the measurement of the normal component of displacements for thin plates or beams in bending [8, 12], and of the in-plane displacements of thin specimens having a low elastic modulus [9,10,11]. When the components of displacements to be measured remain very small, even with a large driving force, then rigid body displacements severely limit the application of the technique. An example is the measurement of the change in thickness of a thin plate subjected to in-plane loading. Because of the small thickness of the plate, the strain in the thickness direction results in a very small displacement normal to the specimen surface. The influence of the large rigid body displacement is thus dominant in the fringe pattern that is obtained. The information related to the strain-induced displacement can then become difficult or impossible to retrieve. In these cases, it would be desirable to devise a technique that would permit one to compensate for the rigid body displacements without altering the information related to the strains.

A technique for altering fringe patterns to make data processing easier was demonstrated by E. Champagne [13]. It has been applied successfully by Kersch [14] for qualitative nondestructive testing applications. Following the same basic principle, a fringe compensation technique is developed in this work for quantitative strain analysis. This technique is applied to the aforementioned problem of thickness change of a thin plate loaded in its plane. Fundamental results of holographic interferometry are first recalled. Then, the principles of the fringe compensation devices are presented. The technique is tested by the quantitative analysis of the out-of-plane surface displacement around a circular hole in a plate loaded in uniaxial tension in its plane. This example is chosen because of the availability of complete analytical solutions to the problem, which provide bases of comparison with the experimental results.

The experimental results obtained by reflection holographic interferometry with fringe compensation can also be compared with the results of transmission holographic interferometry. As a first approximation, the interference fringes can be interpreted physically as lines of equal change in thickness of the specimen, in transmission as well as in reflection. However, a departure from this approximation occurs in transmission. This departure can be attributed to the influence of the normal stress σ_z on the index of refraction of the material, through the stress-optical effect. This fact suggests that an evaluation of σ_z (averaged through the thickness) may be obtained by comparing the fringe orders in reflection and transmission.

The analysis of the fringes is thus made in transmission holographic interferometry. The validity of the results is checked in the example of the circular hole. The analysis of the fringe orders in transmission and reflection is then further developed into a form that would permit a direct estimation of $\bar{\sigma}_z$ in terms of the fringe orders. The experimental results obtained by this method are also compared to the analytical results in the circular hole example. In cases where $\bar{\sigma}_z$ cannot be estimated explicitely, a method is also developed to determine at least the regions where $\bar{\sigma}_z$ is approximately equal to zero, which is a necessary condition for a generalized plane stress analysis of thin plates to be valid.

The potential applications of holographic interferometry to fracture mechanics are explored in the last chapter. Holography is first compared to other techniques, and especially to photoelasticity, as far as applications to crack problems are concerned. Brief examples of application to fracture mechanics are then presented. The profile of the normal surface displacement is estimated along the crack line extension in an aluminum single-edge cracked specimen. An attempt is also made to estimate the extent of the region where generalized plane stress conditions prevail, in conjunction with the use of an auxiliary transparent specimen.

CHAPTER II. BASIC PRINCIPLES OF HOLOGRAPHIC INTERFEROMETRY

A. Introduction

Before the fringe compensation technique and stress analysis methods are presented, the basic principles of holographic interferometry are first outlined. The bases for the analysis of fringes will be presented in terms of static displacements. Two very different approaches can be used to study holographic interferometry. One approach uses the diffraction theory and the concepts of physical optics, and the other is more related to geometric optics. The two methods are entirely consistent and give the same results. The geometrical approach is principally used here because of its greater simplicity of use and physical interpretation. Although the geometric optics concepts are emphasized, a brief introduction to diffraction theory is also given. The Huyghens-Fresnel principle [15] is used as a basis for the equations of holography. The formulas for the Fraunhofer diffraction through a circular aperture are also presented, because of their importance for the understanding of speckle patterns [16]. These speckle patterns are shown to be related to the visibility and depth of localization of the fringes. On the other hand, the purely geometrical concept of "homologous rays" is used for the interpretation of the fringes and the determination of the fringe orders.

B. The Huyghens-Fresnel Principle [15]

The basic physical principle used to account for diffraction phenomena in general and particularly for holography is the Huyghens-Fresnel principle. This principle can be stated as follows:

> "Given a light source A inside a closed surface S, this light source induces at any point M on the surface a light vibration characterized by a phase and amplitude. Each elementary part of the surface S around a point M can be considered as a derived light source with the phase and amplitude created at M by the primary source A. Then the light vibrations propagating from A outside S are identical to those that would be created by all the derived sources distributed on the surface S."

C. Basic Equations of Holography

The hologram, or three-dimensional picture of an object, is obtained in the following way: The laser beam is split into two parts. One is used to illuminate the object in front of a photographic plate (figure 1). The other part is called the "reference beam", and is used to illuminate the plate directly.

The plate is exposed and developed. Then it is set back in its original place and illuminated with the reference beam alone, and the object is removed. The light from the reference beam is diffracted by the hologram plate, yielding a reconstruction of the beam that was previously coming from the object. A virtual image of the original object is thus produced; an observer looking through the plate can see this virtual image behind the hologram as a three-dimensional picture of the object.

1. Relation to Huyghens-Fresnel Principle

The light vibration coming from the object can be defined by its time-independent complex amplitude:

$$U = u \exp(i\phi) \qquad \text{(II-1)}$$

where ϕ is the spatial phase of the light wave. The holographic process can be explained on the basis of the Huyghens-Fresnel principle. The "object beam" and "reference beam" are mutually coherent and give a high spatial frequency stationary interference phenomenon in the region in space where they overlap. If a high resolution photographic plate is set in this interference volume, it records interference fringes on its surface that can be considered as a generalized diffraction grating. When the plate is illuminated by the reference beam after processing, the light from this beam is diffracted by the "holographic grating". It will be shown that the amplitude and phase of the diffracted light emerging from the hologram are identical to those for the incident light coming from the object onto the plate during the recording process. Thus, the hologram in the reconstruction step can be considered as a set of derived sources on the plate surface, identical to the ones that were created on this surface by the source in the recording step. So according to the Huyghens-Fresnel principle, the diffracted light wave emerging from the plate is identical to the one that was originally coming from the object that is being optically reconstructed. The foregoing physical concepts may be formalized by the following simplified analysis.

2. Elementary Analysis [16]

Let A_o and A_r be the scalar complex amplitudes of the light at a point on the plate coming from the object and reference beams, respectively. The total amplitude at this point is

$$A = A_o + A_r$$

The intensity of light (I) resulting from a complex amplitude A is given by

$$I = A A^*$$

where A* is the complex conjugate of A. So, the intensity becomes

$$I = (A_r + A_o)\ (A_r^* + A_o^*)$$

$$I = A_r A_r^* + A_o A_o^* + A_o A_r^* + A_r A_o^* \qquad \text{(II-2)}$$

By definition, the first two terms are the intensities of the reference and object beam, respectively. Therefore,

$$I = I_r + I_o + A_r A_o^* + A_o A_r^* \qquad \text{(II-3)}$$

If a photographic plate has been exposed to this light, then after processing, the amplitude transmittance (t) of the plate is approximately a linear function of the intensity during the exposure**:

$$t \propto I_o + I_r + A_r A_o^* + A_o A_r^* \qquad \text{(II-4)}$$

**Assuming, for this discussion, that a "positive" print is used.

when the developed hologram is re-illuminated with the reference beam, the transmitted complex amplitude (A_t) then becomes:

$$A_t = tA_r \tag{II-5}$$

$$A_t \propto (I_o + I_r) A_r + A_r A_o^* A_r + A_o A_r^* A_r$$

$$A_t \propto (I_o + I_r) A_r + A_r A_o^* A_r + I_r A_o \tag{II-6}$$

Examination of equation II-6 shows that no useful information is stored in the first term. It is just a part of the reference beam that is transmitted straight through the plate. The second term represents a wave diffracted in an oblique direction, and is also without any practical interest. The last term is the one of interest. Its phase and amplitude distribution in the plane of the plate are proportional to A_o, therefore this term reconstructs the original object wave. According to the Huyghens-Fresnel principle, this term gives the optical reconstruction of the object.

D. Holographic Interferometry: Measurement of Static Displacements

1. Real Time Interferometry

Once the wavefront from the object is reconstructed through the holographic process, it can be used for interferometric purposes. The hologram is processed and set back in its original position. The light diffracted from the reference beam yields a virtual image of the object that can be seen through the hologram. Instead of being removed in the viewing process, the original real object can be left

in the system. Then, the real and reconstructed objects are seen simultaneously through the hologram exactly superimposed. If the real object is then given a little displacement or deformation, a small change is introduced in the optical path of the light coming from the real object; interference fringes can then be produced by optical comparison of the real and reconstructed beams.

A hologram interferometer can thus be considered as a dual output optical system [17]. One of the output waves is the reconstructed wave which is equivalent to the wave that was coming from the undisturbed object at the time of recording. The other output wave is the one that is coming from the real displaced object at the time of observation. The fringes that are produced give information about the present state of the object at the time of observation as compared to the "frozen" state when the hologram was recorded. This procedure is thus called "real time" interferometry.

2. Double Exposure Interferometry

The same type of experiment can be carried out in a slightly different way -- the hologram can be recorded in two steps. A first exposure is made for half the nominal exposure time with the object in a given state. Then the object is deformed or displaced and a second "half-exposure" is made on the same holographic plate. In the viewing process, the hologram reconstructs simultaneously the object in both the original and the displaced (deformed) states. This procedure yields the same type of interference fringes as in real time interferometry and is called "double exposure" interferometry. Either method can be used for the measurement of static displacements.

E. Diffraction Phenomena

Diffraction phenomena occur whenever a wave is not free to propagate in empty space but has to pass through a finite aperture. To define the optical disturbance beyond the aperture, it is then necessary to use the Huyghens-Fresnel principle; the value of the optical disturbance at a point P is related to its value over the whole aperture, created by the source S (figure 2). This relation is expressed mathematically by the Kirchoff integral formula [18, page 108]:

$$U_P = -\frac{1}{4\pi} \iint_A \left(U \, \mathrm{grad}_n \frac{e^{ik\rho}}{\rho} - \frac{e^{ik\rho}}{\rho} \mathrm{grad}_n U\right) dA \qquad \text{(II-7)}$$

where U_P is the value at the point P of a scalar quantity such that $U^2 = I$ (intensity)

k = spatial frequency = $\frac{2\pi}{\lambda}$

$\mathfrak{n}$ = the unit vector normal to the aperture

$\mathfrak{L}$ = the vector from P to the point of integration on the aperture

The finite aperture of viewing systems sets a limit to their optical resolution. This limit is caused by diffraction phenomena, and can be quantified through the use of the Kirchoff integral formula. An example of this study is given in the simple, but common case of diffraction through a circular aperture illuminated by a parallel beam. The results obtained in this case are used to obtain an order-of-magnitude estimate of the resolution of an optical system with a

circular aperture for imaging a point source at a finite distance.

1. Optical Resolution of an Imaging System

The purpose of an imaging system is to yield a one-to-one correspondence between points in the object and image spaces. However, this correspondence would be possible only for a perfect lens having an infinite aperture. For a finite size lens, the light from one point on the object is diffracted by the aperture and most of the light from the source is scattered over a finite sized zone of the image plane called the "Airy disk". This imaging of a point source onto a finite sized zone limits the resolving power of the system. The size of this zone will be considered for the case of illumination by a parallel beam, which is identical to light coming from a point source at infinity.

2. Fraunhofer Diffraction by a Circular Aperture [18, page 117]

The aforementioned diffraction phenomena can be given a simple mathematical formulation in the case of a collimated beam that is diffracted through a circular aperture of radius R. The light coming from a point source on the axis of the aperture is collimated by a lens in front of the aperture. A second lens behind the aperture focuses the light onto the image focal plane (figure 3). For a focal plane at a sufficiently large distance from the aperture and an image point P angularly close to the axis, the Kirchoff integral formula reduces to the simple form:

$$U_P = C \iint_A e^{ik\rho} \, dA \qquad \text{(II-8)}$$

The integration is taken over the area (A) of the aperture. Equation II-8 can be derived also directly from the Huyghens-Fresnel principle.

The light diffracted at a point P in the image plane is now considered (figure 3). The point P is defined by the angle Θ, such that parallel rays of light at an angle Θ from the optical axis would be focused onto the point P. Then, from equation II-8, the light intensity at P can be shown to be [18]:

$$I = I_o \left[\frac{2J_1 (kR \sin \Theta)}{kR \sin \Theta} \right] \qquad \text{(II-9)}$$

where J_1 is the Bessel function of the first kind, order one, and I_o is the maximum intensity (at $\Theta = 0$). Plotting the intensity I/I_o versus $kR \sin \Theta$ (figure 4) it is seen that the intensity distribution of light in the image focal plane gives a bright disk surrounded by rings of rapidly decreasing intensities. The bright central area is called the Airy disk. The angular radius of the Airy disk (from the lens center) is Θ_A and is given by the first zero of the Bessel function:

$$kR \sin \Theta = 3.832$$

Taking $k = \frac{2\pi}{\lambda}$ and $R = \frac{D}{2}$, then

$$\sin \Theta_A = \frac{3.832}{kR} = \frac{3.832}{\frac{2\pi}{\lambda} \frac{D}{2}}$$

$$\sin \Theta_A = \frac{1.22\lambda}{D} \qquad \text{(D = diameter of aperture)} \qquad \text{(II-10)}$$

This result can now be used to estimate the apparent diameter of a point source at a finite distance, when it is viewed through an optical system of finite aperture.

3. Imaging of a Point Source at a Finite Distance [19]

A point source S is imaged through a lens of finite aperture (D) onto the associated focal plan (figure 5). The light from S is diffracted over the surface of the Airy disk of angular radius Θ_A. Assuming the source is far enough for equation II-8 to be applicable, then, $\Theta_A = \frac{1.22\lambda}{D}$ from equation II-10. If f is the focal length of the lens, p and p' the image-to-lens and object-to-lens distances, respectively, then:

$$\frac{1}{f} = \frac{1}{p} + \frac{1}{p'} ,$$

The magnification of the lens is M, where $M = \frac{p'}{p}$

$$p' = f\ (1 + M)$$

The apparent radius of the source is $r_A = p'\Theta_A$ (figure 5). Substitution yields

$$r_A = \Theta_A\ f\ (1 + M)$$

$$r_A = 1.22\lambda\ (1 + M)\ \frac{f}{D}$$

Since F = f/D is the numerical value of the lens aperture (ratio of the focal length to the aperture of the lens), the apparent radius of the source becomes:

$$r_A = 1.22\lambda\ (1 + M)\ F \qquad \text{(II-11)}$$

This influence of the finite aperture of the system on the imaging of a source will now be related to the "granular" aspect of objects illuminated with laser light. This granularity is often referred to as "speckle pattern".

F. Speckle Patterns

1. Objective Speckle

Let a diffusing object be illuminated with a coherent (laser) light. The roughness of the surface makes every point of the object behave as minute independent light sources with a random phase distribution. However, the phase difference between any two points on the surface is time-invariant. Therefore, all these independent sources give a stationary interference pattern in the field of the diffused light. A photographic plate placed in this field would record a stationary fluctuation of light intensity, with a high spatial frequency, which is called the "speckle pattern". This pattern is called "objective" because it is independent of any imaging system. It appears as a juxtaposition of bright spots on the photographic plate. At a sufficient distance from the object, the phase distribution is a function of the angle (figure 6) and the approximate size of the spots is $S = \lambda\ell/D'$ where ℓ is the distance from the object to the plane of observation and D' is the diameter of the illuminated area [19].

2. Observed Speckle

The objective speckle pattern has a high spatial frequency. However, when the object is observed through an imaging system (eye, camera objective), its surface exhibits a granular appearance with a much lower spatial frequency. This new speckle pattern is called the "observed" one and its characteristics depend on the imaging system that is used. The size of the "grains" is approximately equal to the size of the Airy disk corresponding to the imaging of a point source on the object surface when viewed through the imaging system. It is recalled that this size is:

$$r_A = 1.22\lambda\ (1 + M)\ F \qquad \text{(II-12)}$$

A conclusion of great practical importance is that the size of the speckles increases when the aperture of the viewing lens is reduced. This property will be shown to be connected to the visibility of the object displacement interference fringes.

G. Influence of the Imaging System -- Visibility of the Fringes

The object is viewed through an imaging system in two different states simultaneously. In each of these states the object

would produce a given observed speckle pattern in the image plane of the viewing system. These speckle patterns are approximately similar, but they can be slightly shifted with respect to one another by a vector $\underset{\sim}{d}$. The fringes come into focus in regions where the images of these two speckle patterns are superimposed on the image plane. This condition is satisfied when the lens is focused on the surface where the fringes are localized in the object space. However, when the object is strained and displaced, this surface of localization can have a complicated shape and it often becomes impossible to have all of this surface in focus; the fringe visibility is then reduced over some parts of the field. This visibility is defined by:

$$V = \frac{I_{max} - I_{min}}{I_{max} + I_{min}}$$

Where I_{max} is the light intensity at the center of bright fringes, and I_{min} at the center of dark ones. The visibility depends on the correlation of the speckle patterns on a given region. It has been seen that the average size of the speckle grains is approximately the size of the Airy disk that would be observed when a point-source localized on the object is viewed through the imaging system. The apparent size of this disk on the object is, from equation II-12

$$d_o = 2r_A \simeq 2.4\lambda\,(1+M)\,F \qquad \text{(II-13)}$$

If the relative displacement of both speckle patterns is d, the fringe visibility is maximum (unity) when d = 0; it decreases as (d/d_o) increases and goes to zero when $(d/d_o) \geq 1$. Then the speckle

patterns are no longer correlated and the fringes disappear. For a given relative displacement of the object, the speckles shift depends on the lens focusing and the speckle size depends on the aperture F of the lens. In practice, the fringe visibility increases when the lens aperture is reduced, the ratio d/d_o being then increased. The focusing is then adjusted to get the best possible visibility in the region of interest. However, the fringes are no longer resolved by the system when the speckle grain size approaches the spatial frequency of the fringes. In practical cases, a compromise must thus be found between the resolution of the system and the area over which fringes are visible.

H. Concept of Homologous Rays

In the real-time interferometric procedure, it has been shown that the optical comparison of the real light wave from the object, and of the holographically reconstructed one, can produce some interference fringes. The existence and visibility of these fringes has been related to the observed speckle patterns. The question now arises as to how to relate these fringes to the relative displacement of the real and reconstructed objects. The physically simple concept of "homologous rays" was proposed in 1968 by Vienot et al. [20] to answer this question through the use of geometric optics concepts. A very complete and more sophisticated analysis was made by Sten Walles [21], using the theory of diffraction. By a completely different method, this theory confirms Vienot's approach which is now going to be presented.

The fringe formation process is closely related to the speckle pattern of the two waves that are to interfere. The amplitude and phase of the light wave reflected by a scattering object have been shown to be randomly distributed with a high spatial fluctuation frequency which causes the speckle patterns that were discussed previously. The wavefronts, or surfaces of equal phase, are very complicated. However, Vienot assumed that when the object is slightly moved, the new wavefronts still have a great similarity with the undisturbed ones (figure 7). They are simply rotated and translated with the object.

With the object in a position "1", a direction of observation x_1 is defined. M_1 and P_1 are two points on the axis x_1, respectively, on the object surfaces and on a diffracted wavefront Σ_1. The object is moved into a position "2", with the corresponding wavefront Σ_2. Let M_2 be the point corresponding to M_1 on the object and P_2 corresponding to P_1 on the new wavefront Σ_2, then, M_1P_1 and M_2P_2 are called "homologous rays". Only couples of homologous rays can give an interference phenomenon. This interference will occur in the region where both homologous rays intersect; this is the only place in space where the speckle patterns of both scattered waves have a similar shape. In this region, the phase difference between both waves has a relatively small spatial frequency variation related to the object displacement. At any other place in space, the phase difference is randomly distributed and no constructive interference can occur.

1. Relations Between Homologous Rays

Although homologous rays or waves have been defined, no relation between them has been defined so far in terms of the displacement of the object. A model introduced by B. Howell [22] can be used very conveniently for that purpose. The scattering surface is considered as a juxtaposition of infinitely many minute mirrors randomly oriented. So, whatever direction of observation is chosen, it is always possible to find some of these mirrors that will reflect the light from the illumination source into the direction of observation (figure 8). Only rays of lights reflected on corresponding facets in two different states of the object can interfere. Indeed, these rays are the "homologous" ones according to Vienot's definition [20]. This approach also lets one see that these homologous rays are shifted and rotated according to the simple laws of geometric reflection. Homologous rays can thus be easily constructed from the geometry of the system defined by the position of the source, direction of observation and positions of the object. The place where interference occurs can be easily determined at the point of intersection of the corresponding rays. Conversely, when a static displacement is to be determined from the interference fringes, the localization of the fringes can be determined by this method. They can be focused on with a short depth-of-field viewing instrument. It is also possible to use paralax effects to determine the localization of the fringes, as was proposed by Aleksandrov and Bonch-Bruevich [23]. The localization of the fringes being defined, the fringe order can be determined through the use of the same concepts.

2. Order of Interference [24]

The order of interference can be defined only at a point where interference occurs. This happens in regions of localization as previously defined, such as at the point I in figure 8. It also happens at points such as F in figure 9, where F is the image of I through an imaging system. In figure 9, the optical distance along a line such as SPCF is called $\ell_{(SPCF)}$. The optical path difference along two different trajectories of the light from the source S to the point of interference F is called δ:

$$\delta = \ell_{(SQDF)} - \ell_{(SPCF)} \tag{II-14}$$

Then the fringe order at the point F is

$$N = \frac{\delta}{\lambda} \tag{II-15}$$

Since F is the image of I through the lens, a property of the imaging system is that two different optical paths from the object to the image point be equal:

$$\ell_{(IPCF)} = \ell_{(IQDF)} = L$$

$$\ell_{(SQDF)} = SQ + L - IQ$$

$$\ell_{(SPCF)} = SP + L - IP$$

$$\delta = SQ - SP - IQ + IP \tag{II-16}$$

The unit vectors along AP, IP, SQ, IQ are designated as $\underset{\sim}{i}_1$, $\underset{\sim}{i}_2$, $\underset{\sim}{i}_3$ and $\underset{\sim}{i}_4$, respectively. Since

$$\underset{\sim}{IP} = \underset{\sim}{IS} + \underset{\sim}{SP}$$

$$IP = \underset{\sim}{i}_2 \cdot \underset{\sim}{IS} + \underset{\sim}{i}_2 \cdot \underset{\sim}{SP} = \underset{\sim}{i}_2 \cdot \underset{\sim}{IP}$$

$$\underset{\sim}{IQ} = \underset{\sim}{IS} + \underset{\sim}{SQ}$$

$$IQ = \underset{\sim}{i}_4 \cdot \underset{\sim}{IS} + \underset{\sim}{i}_4 \cdot \underset{\sim}{SQ} = \underset{\sim}{i}_4 \cdot \underset{\sim}{IQ}$$

then,

$$\delta = (\underset{\sim}{i}_3 \cdot \underset{\sim}{SQ}) - (\underset{\sim}{i}_1 \cdot \underset{\sim}{SP}) - (\underset{\sim}{i}_4 \cdot \underset{\sim}{IS} + \underset{\sim}{i}_4 \cdot \underset{\sim}{SQ}) + (\underset{\sim}{i}_2 \cdot \underset{\sim}{IS} + \underset{\sim}{i}_2 \cdot \underset{\sim}{SP})$$

Letting

$$\underset{\sim}{i}_3 = \underset{\sim}{i}_1 + \Delta\underset{\sim}{i}_1 \qquad \text{and} \qquad \underset{\sim}{i}_4 = \underset{\sim}{i}_2 + \Delta\underset{\sim}{i}_2$$

$$\delta = \underset{\sim}{i}_1 \cdot \underset{\sim}{SQ} + \Delta\underset{\sim}{i}_1 \cdot \underset{\sim}{SQ} - \underset{\sim}{i}_1 \cdot \underset{\sim}{SP} - \underset{\sim}{i}_2 \cdot \underset{\sim}{IS} - \Delta\underset{\sim}{i}_2 \cdot \underset{\sim}{IS} - \underset{\sim}{i}_2 \cdot \underset{\sim}{SQ}$$

$$- \Delta\underset{\sim}{i}_2 \cdot \underset{\sim}{SQ} + \underset{\sim}{i}_2 \cdot \underset{\sim}{IS} + \underset{\sim}{i}_2 \cdot \underset{\sim}{SP}$$

$$= (\underset{\sim}{i}_1 - \underset{\sim}{i}_2)\ (\underset{\sim}{SQ} - \underset{\sim}{SP}) + \Delta\underset{\sim}{i}_1 \cdot \underset{\sim}{SQ} - \Delta\underset{\sim}{i}_2\ (\underset{\sim}{IS} + \underset{\sim}{SQ})$$

Hence

$$\delta = (\underset{\sim}{i}_1 - \underset{\sim}{i}_2)\ (\underset{\sim}{SQ} - \underset{\sim}{SP}) + \Delta\underset{\sim}{i}_1 \cdot \underset{\sim}{SQ} - \Delta\underset{\sim}{i}_2 \cdot \underset{\sim}{IQ} \qquad \text{(II-17)}$$

When the distances from the object to the source S and to the lens are large enough compared to the displacement PQ, then $\Delta\underset{\sim}{i}_1 \cdot \underset{\sim}{SQ}$ =

$\Delta \underset{\sim}{i}_2 \cdot \underset{\sim}{IQ} = 0$, and this path difference is reduced to

$$\delta = (\underset{\sim}{i}_1 - \underset{\sim}{i}_2)(\underset{\sim}{SQ} - \underset{\sim}{SP}) = (\underset{\sim}{i}_1 - \underset{\sim}{i}_2) \cdot \underset{\sim}{PQ} \qquad \text{(II-18)}$$

3. Determination of Static Displacement

Along with the localization of the fringes, the formula giving the fringe order can be used to determine the components of displacements of an object. Many different techniques have been proposed to process the results according to particular cases to be studied. The particular configuration of normal directions for both illumination and viewing will be studied in detail in the next chapter.

I. Conclusions

The applications of holographic interferometry to measurements of small displacements and deformations have been steadily developed in the past few years. The major advantages of this technique are its great sensitivity, resolution power, and ability to yield whole field measurements, in contradiction to some other measurement techniques which can only provide discrete data. Although it is an advantage in itself, the sensitivity of the technique makes its use often delicate. Very severe requirements are imposed onto the experimental system. The most important one is that it be highly vibration free. When very small displacements are to be measured, some difficulties also arise from unwanted displacements that tend to interfere with the one to be measured. This problem is especially acute in strain analysis. It can be solved, in some cases, by the fringe compensation technique presented in the next chapter.

CHAPTER III. FRINGE COMPENSATION TECHNIQUE

A. Purpose of Fringe Compensation

As stated in the introductory chapter, the purpose of the technique is to eliminate the rigid body displacements influence from the fringe pattern obtained during strain analysis by holographic interferometry. Holographic interferometry provides an optical comparison between the reconstructed object in its initial state and the real object at a different load. This loaded state can be considered as being reached in two imaginary steps (figure 10); the object would first be rigidly displaced and then strained in this new position. A surface point P would be displaced to Q in the rigid displacement, then to Q' by straining. Then:

$$\underset{\sim}{PQ'} = \underset{\sim}{PQ} + \underset{\sim}{QQ'} \qquad \text{(III-1)}$$

The displacement vector of interest for stress analysis is $\underset{\sim}{QQ'}$. The purpose of fringe compensation is to introduce optical modifications in the system for eliminating the influence of $\underset{\sim}{PQ}$ from the fringe pattern.

For this goal to be achieved, the first imaginary step (displacement without straining) is first considered alone. This rigid displacement would induce some fringes that could be interpreted through the use of equation II-18, where $\underset{\sim}{i_1}$ and $\underset{\sim}{i_2}$ are given by the initial geometry of the system. It will be shown that these fringes could be cancelled by an adjustment of the optical system geometry.

The fringe order would thereby be reset to zero over the entire surface of the specimen. The second imaginary step (i.e., pure straining) would then be performed. The resultant fringes would then be attributable to strain only. For a first approximation, these fringes could be interpreted again through equation II-18. However, the vector $\underset{\sim}{i}_1$ involved in this equation represents the unit vector in the direction of illumination. This direction would be changed in the compensation technique. This modification in the direction of illumination must be taken into account in the analysis of the fringes, which will be done in the following analysis.

B. Initial Geometry of the System

The displacement to be measured is normal to the surface of the specimen. To maximize the sensitivity to this component of the displacement vector $\underset{\sim}{PQ}$ in equation II-18, a normal direction for both illumination and viewing was selected. A semi-reflecting plate (beam-splitter) must be used for that illumination and for viewing. Both the illumination beam and the reference beam used in the holographic process are collimated; this is a necessary feature for the fringe compensation technique that is used. The complete system is illustrated schematically in figure 11. A photograph of the actual set-up is shown in figure 12. The initial vectors $\underset{\sim}{i}_1$ and $\underset{\sim}{i}_2$ are indicated in figure 13; $\underset{\sim}{i}_1$ is normal to the surface of the specimen, and $\underset{\sim}{i}_2$ makes a small angle θ with the normal. The angle θ depends on the distance r from the optical axis of the viewing system, and on the distance L between the object and the viewing lens.

$$\theta \simeq \tan \theta = r/L \qquad \text{(III-2)}$$

The rigid body motion is defined by its three translational and three rotational components. If one defines Oz as the direction of the optical axis, the three translations can be reduced to one component along Oz, and another in the plane of the specimen. Similarly, one can choose to consider only two rotations, one about Oz and the other about an axis in the plane of the specimen.

C. Compensation for Translations

When a collimated reference beam is used, the fringes caused by translation of the real object can be readily eliminated by an equal translation of the hologram. The reference wave is plane and the hologram is translated parallel to itself. Thus, the object is always reconstructed at the same position with respect to the hologram and is translated together with it without any distortion. Only a uniform phase difference is introduced, which produces no fringes. The plate holder is thus mounted on a micro-positioner giving translations along three mutually perpendicular axes. The rigid body translations of the object are simply eliminated by giving the hologram a translation equal to that of the object.

D. Compensation for Rotations

1. Rotation about the Axis Oz

By the use of normal incidence for illumination and viewing, the system is made theoretically insensitive to this component of the rotation. From figure 13, it is seen that the displacement of

the point P in a rotation about Oz is perpendicular to both $\underset{\sim}{i}_1$ and $\underset{\sim}{i}_2$. So, the scalar product in equation II-18 gives a zero path difference. However, it will be seen later that a slight change in the direction of $\underset{\sim}{i}_1$ is introduced in correcting for the other rotations, so that this result no longer holds rigorously. Nevertheless, the sensitivity to a rotation about Oz remains very low. In practical cases, no further correction is required, provided that the optical axis Oz properly matches the initial direction of illumination $\underset{\sim}{i}_1$.

2. Rotation about an Axis Perpendicular to Oz

It is now supposed that the rotation about Oz and the translations have been corrected, so that the point on the real object and its homologous point on the reconstructed one coincide on the optical axis of the system. Then, only a rotation about an axis $O\xi$ perpendicular to Oz remains, and the fringes caused by this rotation are to be eliminated. The procedure for this compensation is considered below.

In figure 14, the axis $O\xi$ is taken to be perpendicular to the plane of the figure. For a point P that is moved to Q in the displacement, the path difference due to the rotation is:

$$\delta_P = (\underset{\sim}{i}_1 - \underset{\sim}{i}_2) \cdot \underset{\sim}{PQ} \qquad \text{(III-3)}$$

The triangle OPQ for the computation of δ is shown in more detail in figure 15. The path difference related to the pair of points (P,Q) is:

$$\delta_P = SQ + QR \qquad \text{(III-4)}$$

$$\delta_P = OP\left[\sin\varphi + 2\sin\frac{\varphi}{2}\cos\left(\theta + \frac{\varphi}{2}\right)\right] \qquad \text{(III-5)}$$

Setting OP = r, and considering the fact that φ and θ are small angles, then

$$\delta_P = r\left\{\varphi + 2\frac{\varphi}{2}\left[1 - \frac{\left(\theta + \frac{\varphi}{2}\right)^2}{2} + \ldots\right]\right\} \qquad \text{(III-6)}$$

or

$$\delta_P \simeq 2\varphi r \qquad \text{(III-7)}$$

Approximate compensation of these fringes introduced by rotation of the object about Oξ may be made by a rotation of the illumination wave by an angle α about the same axis. This is actually achieved by granting the beam-splitter two degrees of freedom in rotation about two perpendicular axes in its plane. The illumination beam can thus be made to rotate about any axis in the plane of the specimen. The illumination beam being parallel, O and P can be considered as illuminated by two identical sources S_1 and S_1' with the following conditions (figure 16): OS_1 and PS_1' are oriented along the direction of illumination; S_1S_1' is perpendicular to this direction, and OS_1 is equal to the distance, called ℓ_1, between O and the real source. Likewise, when the object is rotated by an angle φ, and the illumination beam by α, another pair of sources S_2 and S_2' can be defined. S_2 and S_2' are in the new direction of illumination, S_2S_2' is perpendicular to this direction, and $OS_2 = \ell_2$ is the new optical distance between O and the real source.

In the new real-time interferometric process the fringes corresponding to the point O are located at some point J on the optical axis OC (figure 16). The fringes correspcnding to the couple of points P,Q are located at a point I on the line PC. The fringe order for the point O is computed from the optical path difference:

$$\delta_o = S_1O - OJ - (S_2O - OJ) \qquad \text{(III-8)}$$

$$\delta_o = S_1O - S_2O = \ell_1 - \ell_2 \qquad \text{(III-9)}$$

The optical path difference for the pair of points P and Q is computed from equation II-16 which is modified according to the new geometry.

$$\delta_P = (S_1'P - PI) - (S_2'Q - QI) \qquad \text{(III-10)}$$

$$\delta_P = (S_1'P - PM - MI) - (S_2'N + NQ - QI)$$

Since $MI = QI$ and $PQ = 2OP \sin \varphi/2 = 2r \sin \varphi/2$, then

$$\delta_P = [\ell_1 - 2r \sin \varphi/2 \cos (\theta + \varphi/2)]$$

$$-[(\ell_2 - r \sin \alpha) + 2r \sin \varphi/2 \cos (\theta - \varphi/2)]$$

$$\delta_P = \ell_1 - \ell_2 + r \sin \alpha - 2r \sin \frac{\varphi}{2} [\cos (\theta + \frac{\varphi}{2}) + \cos (\theta - \frac{\varphi}{2})]$$

$$\delta_P = \ell_1 - \ell_2 + r \sin \alpha - 4r \sin \frac{\varphi}{2} \cos \theta \cos \frac{\varphi}{2} \qquad \text{(III-11)}$$

$$\delta_P = \ell_1 - \ell_2 + r (\sin \alpha - 2 \cos \theta \sin \varphi) \qquad \text{(III-12)}$$

The new number of fringes between O and P is $\left(\frac{\delta_P - \delta_O}{\lambda} \right)$. Using equations III-9 and III-12:

$$\delta_P - \delta_O = r \, (\sin \alpha - 2 \cos \theta \sin \varphi) \qquad \text{(III-13)}$$

The desired correction is achieved when $(\delta_P - \delta_O) = 0$ for any r. Close to the optical axis, $\cos \theta \simeq 1$. So, the correction is obtained by adjusting the tilt of the beam splitter so that:

$$\alpha = 2\varphi$$

Since cos θ is not exactly equal to unity over the whole field, a small error is made in the correction. This error has to be estimated in terms of the distance r after setting $\alpha = 2\varphi$. In equation III-13, the remaining path difference is called ϵ_δ.

$$\epsilon_\delta = r \, [\sin 2\varphi - 2 \cos \theta \sin \varphi]$$

For $\theta \simeq r/L << 1$, ϵ_δ may be given approximately by:

$$\epsilon_\delta \simeq r \left[\sin 2\varphi - 2 \sin \varphi \left(1 - \frac{r^2}{2L^2}\right)\right]$$

or, for very small values of φ,

$$\epsilon_\delta \simeq \frac{r^3 \varphi}{L^2} \qquad \text{(III-14)}$$

The corresponding fringe order is called ϵ_N:

$$\epsilon_N = \frac{\epsilon_\delta}{\lambda} = \frac{r^3}{\lambda L} \varphi$$

To estimate this error (ϵ_N) the value of the angle of rigid rotation of the specimen (φ) must be known. It can be derived in two different ways. The first method consists of recording the tilt angle α of the beam splitter that is required to compensate for the rotation φ of the specimen. Then, according to equation III-14, $\varphi = \alpha/2$. The second method to determine φ consists of counting the number of fringes N_P prior to compensation, between the origin O and a point P. This number is:

$$N_P = \frac{\delta_P}{\lambda}$$

According to equation III-7, $\delta_P \simeq 2\varphi r$. Thus,

$$\varphi \simeq \frac{\lambda N_P}{2r} \qquad \text{(III-15)}$$

The error on the fringe order after correction is usually very small. Its order of magnitude can be evaluated for the following typical example. At a distance r = 0.5 in. (12.7 mm) from the optical axis, where the fringe order prior to correction would be N_P = 50 fringes and with L = 10 in. (254 mm), the correction error would be:

$$\epsilon_N = \frac{50 \times (0.5)^2}{(10)^2 \times 2} \simeq 0.06 \text{ fringe}$$

Because of simplifications in its development, the foregoing error analysis holds only for points along the axis Or, which is perpendicular to the axis of rotation Oξ in the plane of the specimen.

However, this analysis can be readily extended to an arbitrary axis Or'. The rotations φ and α about $O\xi$ are then decomposed along the axes Or' and $O\xi'$ (normal to Or'). The same results are obtained showing that the compensation is valid over the whole field.

E. Compensation for an Unknown Rigid Body Displacement

When the fringes are to be eliminated without any prior knowledge of the nature of the displacement, an apparent ambiguity occurs. Lateral translation and rotation about an axis in the plane of the specimen both give the same type of fringes represented by straight parallel and equidistant lines. This ambiguity, however, can be eliminated by considering the location of the fringes. For rotation, the fringes appear very close to the surface, whereas for translation, they are located at infinity. For combined rotation and translation, the fringes are located at some distance from the object. The procedure for a good correction consists of first reaching a state where very few broad fringes localized very close to the surface are left. This is controlled by focusing the viewing lens on the object surface and checking that the fringes are clear over the whole field even with a large lens aperture. This state cannot be reached unless the translations are properly corrected. Then the few remaining fringes are nulled by a small, final angle correction.

F. Case of Strains Combined with a Known Displacement

The rigid body displacement is assumed to be known and to have been corrected as indicated previously. Then the object is

strained in its displaced position which induces new displacements from Q to Q' (figures 10 and 17). The new optical path difference is (figure 17):

$$\delta'_P = (S'_1P + PC) - (S''_2Q' + Q'C) \qquad \text{(III-16)}$$

$$\delta'_P = [(S'_1P + PC) - (S'_2Q + QC)] + [(S'_2Q + QC) - (S''_2Q' + Q'C)] \qquad \text{(III-17)}$$

The first term in square brackets results from the rigid displacement alone and has the value δ_P given by equation III-12. The second term is the usual term of interference for the displacement QQ' with the direction of illumination $\underset{\sim}{i}'_1$ along S'_2Q, and can be computed from equation II-18:

$$(S'_2Q + QC) - (S''_2Q' + Q'C) = (\underset{\sim}{i}'_1 - \underset{\sim}{i}_2) \cdot \underset{\sim}{QQ}'$$

Equation III-17 thus becomes:

$$\delta' = (\ell_1 - \ell_2) + r(\sin\alpha - 2\cos\theta\sin\varphi) + (\underset{\sim}{i}_1 - \underset{\sim}{i}_2) \cdot \underset{\sim}{QQ}' \qquad \text{(III-18)}$$

The strain-related displacement can be resolved into its components along the r and z axes:

$$\underset{\sim}{QQ}' = u_r \underset{\sim}{i}_r + w \underset{\sim}{i}_z$$

The in-plane displacement component perpendicular to $\underset{\sim}{i}_r$ is neglected since it induces no fringes. Based on the following dot products of unit vectors:

$$\underset{\sim}{i}_1' \cdot \underset{\sim}{i}_r = -\sin\alpha$$

$$\underset{\sim}{i}_1 \cdot \underset{\sim}{i}_z = -\cos\alpha$$

$$\underset{\sim}{i}_2 \cdot \underset{\sim}{i}_r = -\sin\theta$$

$$\underset{\sim}{i}_2 \cdot \underset{\sim}{i}_z = \cos\theta$$

the term $(\underset{\sim}{i}_1' - \underset{\sim}{i}_2) \cdot \underset{\sim}{QQ}'$ in equation III-18 can be written as follows:

$$(\underset{\sim}{i}_1' - \underset{\sim}{i}_2) \cdot \underset{\sim}{QQ}' = u_r\,(-\sin\alpha + \sin\theta) + w\,(-\cos\alpha - \cos\theta) \qquad \text{(III-19)}$$

From equations III-18 and III-19, the path difference is then given by:

$$\delta' = (\ell_1 - \ell_2) + r\,(\sin\alpha - 2\cos\theta\sin\varphi) + u_r\,(\sin\theta - \sin\alpha)$$

$$- w\,(\cos\theta + \cos\alpha) \qquad \text{(III-20)}$$

For initially normal directions of illumination and viewing of the specimen and for small rigid-body rotation and angular compensation:

$$\cos\theta \simeq \cos\alpha \simeq 1$$

$$\sin\theta \simeq r/L$$

$$\sin\alpha \simeq \alpha$$

$$\sin\varphi \simeq \varphi$$

Then, equation III-20 becomes:

$$\delta' = (\ell_1 - \ell_2) + r\,(\alpha - 2\varphi) + u_r\,(\frac{r}{L} - \alpha) - 2w \qquad \text{(III-21)}$$

The fringe order is $N = \delta'/\lambda$. The constant term $(\ell_1 - \ell_2)$ can be dropped since it introduces only a uniform fringe order shift. In equation III-21, the term αu_r can be considered to be negligibly small. Thus, the fringe order is given by:

$$N = \frac{1}{\lambda}\left[- 2w + r\,(\alpha - 2\varphi + \frac{u_r}{L}) \right] \qquad \text{(III-22)}$$

When the rigid body displacements are perfectly corrected, equation III-14 is satisfied:

$$\alpha - 2\varphi = 0$$

Furthermore, if the radial displacement u_r does not have a greater order of magnitude than w, then:

$$u_r \frac{r}{L} << w \qquad \text{(III-23)}$$

The fringe order in equation III-22 then simply gives an evaluation of the displacement component normal to the surface; that is:

$$N = - \frac{2w}{\lambda} \qquad \text{(III-24)}$$

This relation shows that the fringes are lines of equal normal displacement. The zero order fringe usually cannot be determined; thus, the absolute displacement w remains unknown. The difference in

elevation between any two points, however, is known through the difference in fringe order. The slope of the surface in any direction is thus given at every point through the directional gradient of the fringe order at that point. If the distance along a line of interest is measured by s, we have:

$$\frac{dw}{ds} = \frac{\lambda}{2} \frac{dN}{ds} \qquad \text{(III-25)}$$

In order for the absolute displacement to be determined over the whole field, it must be known at some point on the surface. In the case of a thin plate subjected to remote loading in its plane, for instance, the displacement may be deduced from the known stress "at infinity". The stress σ_z through the thickness is considered to be zero away from regions of stress concentrations. The absolute displacement normal to the surface in these regions is readily obtained from the equations of elasticity. Then, a simple fringe count, together with the use of equation III-24, gives the normal displacement at any point on the surface.

G. Case of Strains Combined with an Unknown Displacement

This is usually the case that is encountered in practical applications. For pure rigid body motion, the criterion for exact angle correction is that the fringe order is nulled over the whole field. This criterion is now useless since some of the fringes are produced by strains. Equation III-21 is still used to compute the fringe order, but equation III-14 cannot be assumed to be satisfied. Keeping the approximation of equation III-23, we have:

$$N = \frac{1}{\lambda} [- 2w + r(\alpha - 2\varphi)]$$

This relation shows that the fringes still give a "map" of the lines of equal normal displacement. The plane of reference, however, is no longer perpendicular to the optical axis; it is inclined by a small unknown angle $(\alpha - 2\varphi)$ about an unknown axis $O\xi$ in the plane of the specimen. This angle must be made as small as possible. A variety of methods can be used to achieve this goal. The most convenient methods take advantage of the symmetry of the system, if any, or of special boundary conditions. It is also possible to use an auxiliary mirror.

1. Symmetry of the Sample

Whenever the specimen and the associated loading have an axis of symmetry, the fringe pattern also should be symmetric with respect to this axis. The illumination beam is then adjusted accordingly. The remaining uncorrected rotation would be about an axis perpendicular to the axis of symmetry. If there are two axes of symmetry, the double symmetry of the fringe pattern ensures a complete correction of the rigid-body rotation. This is the case for a rectangular specimen, with a central hole, loaded in remote tension that is used to illustrate the technique.

2. Special Boundary Conditions

In many cases the stresses are known to be uniform over some parts of the specimen. This is typically the case for a plate under simple remote tension, where a uniform tensile stress is considered

to be applied "at infinity". Then the normal displacement w is constant where the stresses are uniform. The illumination beam is thus adjusted to get a constant fringe order over these regions of the specimen. This technique is used for the second illustrative example - a specimen with a single-edge notch crack loaded in remote tension. Since only one axis of symmetry is present, an addition condition is needed to cancel $(\alpha - 2\varphi)$.

3. Use of an Auxiliary Mirror

If neither of the previous techniques can be used, an auxiliary mirror can be fixed on the surface through a three-point base. This base defines a plane of reference. The adjustment is made to cancel the fringes from the mirror. Then the fringes on the sample give a measurement of the normal displacements with respect to the above reference plane.

H. Applications of the Technique

The technique developed in this chapter was used to obtain the normal displacement component in the strain analysis of thin plates with in-plane loading. Examples of the fringe patterns that were obtained are shown in figure 18. Figure 18-a was obtained from a rectangular strip in tension with a central hole. Figure 18-b was obtained with an aluminum single-edge notched plate. These pictures give only a qualitative idea of the results that can be obtained. A quantitative analysis of the interferogram of figure 18-a is given in the next chapter. The interferograms of figure 18 give qualitative

evidence of the efficiency of the fringe compensation in the production of reflection holographic interferograms. Both were indeed obtained after compensation of rigid body displacements that were large enough to cause the fringes to disappear completely prior to compensation.

CHAPTER IV. NORMAL SURFACE DISPLACEMENT AROUND A CIRCULAR HOLE IN A PLATE

A. Introduction

In the last chapter, a fringe compensation technique for reflection holographic interferometry was presented. The purpose of this technique was to eliminate from the interferograms the influence of the rigid body displacements of the object. The equations to be used for interpretation of the fringes were derived in detail for the special case where the quantity to be measured is the normal, or out-of-plane, component of the surface displacement. Two fringe patterns obtained with this compensation technique were shown, one around a circular hole, the other around the tip of a notch in an aluminum plate. The first interferogram is analyzed numerically in the present chapter. The specimen was made of polymethylmethacrylate (PMMA) painted on its front surface to make it reflecting. The geometry of the specimen is shown in figure 19. The diameter (2a) of the hole is equal to the thickness of the specimen (figure 19). The optical and mechanical properties of PMMA are given in table 1.

The data were processed to obtain the displacement component w normal to the surface along two diameter extensions Ox and Oy, and around the circle $r = a\sqrt{2}$. The component w gives the average value of the transverse strain component ϵ_z through the thickness.

The experimental results were compared to the classical two-dimensional, generalized plane stress analysis. A discrepancy was found close to the hole boundary, which is accounted for by comparison to the three-dimensional analysis made by Alblas [25]. To avoid ambiguity in the following study, the difference must be stated clearly between this complete three-dimensional analysis, and the two-dimensional generalized plane stress analysis. This difference will be first recalled, and the results of both analyses will be presented. Then, the data processing procedure will be explained, including the various steps related to the fringe compensation. The experimental results will be given along the x and y axes (figure 19) and around a circle of radius $a\sqrt{2}$ around the hole.

B. Analytical Results

The analysis that is most commonly used in the study of thin plate problems is based on the assumption of generalized plane stress. In this analysis, the transverse stress σ_z is assumed to be zero everywhere and the in-plane stresses σ_x and σ_y are assumed to be independent of the z-coordinate. Although this stress analysis involves only the two coordinates x and y, it implies also some displacements in the z-direction. Their computation is straightforward, since the strain in the z-direction is uniform and is equal to:

$$\epsilon_z = -\frac{\nu}{E}(\sigma_x + \sigma_y) \qquad \text{(IV-1)}$$

The z-component of the surface displacement for a plate of thickness h (refered to the mid-plane of the plate) is thus:

$$W = -\frac{h\nu}{2E}(\sigma_x + \sigma_y) \qquad \text{(IV-2)}$$

On the other hand, the three-dimensional solution takes into account the existence of a non-zero transverse stress σ_z, and a change in σ_x and σ_y through the thickness of the specimen. Physically, the conditions of generalized plane stress can be expected to be satisfied for thin plates, away from stress concentrations. But a three-dimensional analysis is necessary in regions close to stress concentrations. Both solutions, however, should be equivalent in the far field. This is what actually occurs in the case of a circular hole in a plate under tension. The two-dimensional solution is found in any textbook on the theory of elasticity. A three-dimensional analysis is proposed by Alblas [25]. When the results of both methods are compared, a discrepancy is observed close to the hole boundary, which is referred to as "three-dimensional effect", or "thickness effect" due to the hole. According to the Alblas analysis, this thickness effect vanishes when the distance from the hole boundary is greater than $r \simeq 2a$. The results of the two and three-dimensional analysis then become identical. This property will be assumed to be true for the data processing. Its consistency will be checked a posteriori from the experimental results. The results of both theories will now be presented in terms of the out-of-plane surface displacement they predict, since this is the quantity that is measured experimentally.

For convenience in the presentation of the results, the surface displacement is characterized by the quantity:

$$\frac{W_\infty - W}{W_\infty} \qquad \text{(IV-3)}$$

where W_∞ is the normal surface displacement in the area of uniform stress "at infinity". The derivations, given in Appendix I, provide the following results:

1. Two-Dimensional Analysis

$$\frac{W_\infty - W}{W_\infty} = \frac{2a^2}{r^2} \cos 2\theta \qquad \text{(IV-4)}$$

2. Three-Dimensional Analysis

$$\frac{W_\infty - W}{W_\infty} = \left[\frac{2a^2}{r^2} - \frac{1}{\nu} \eta \left(\frac{r}{a} \right) \right] \cos 2\theta \qquad \text{(IV-5)}$$

In this expression, $\eta\,(r/a)$ is a quantity introduced by Alblas [25] to define the average value (through the thickness) of the stress σ_z in the z-direction, $(\bar{\sigma}_z)$:

$$\eta \left(\frac{r}{a} \right) = \frac{\bar{\sigma}_z}{\sigma_\infty \cos 2\theta} \qquad \text{(IV-6)}$$

where

$$\bar{\sigma}_z = \int_{-\frac{h}{2}}^{\frac{h}{2}} \sigma_z \, d_z$$

The quantity $\eta\,(r/a)$ is plotted versus r/a in figure 20 which is a reproduction of figure 3 in reference 25.

C. Fringe Compensation and Data Processing

The normal surface displacement W is given approximately by equation III-24:

$$N = -2W/\lambda$$

For better accuracy, equation III-22 must be used; hence,

$$N = \frac{1}{\lambda}\left[-2W + r\left(\alpha - 2\varphi + \frac{u_r}{L}\right)\right]$$

$$-\frac{2W}{\lambda} = N - \frac{r}{\lambda}(\alpha - 2\varphi) - \frac{ru_r}{\lambda L} \qquad \text{(IV-7)}$$

Theoretically, the fringe order N should be determined at any point by counting the number of fringes from the one of zero order. Unfortunately, there is usually no way to determine this "zeroth" order fringe a priori. The fringe order N is thus defined within an unknown additive constant η_c. If the fringes are counted from a fringe "at infinity", then the relative fringe order is defined as:

$$N' = N - N_\infty$$

where N_∞ is the fringe order corresponding to the state of uniform stresses away from the hole. Equation IV-7 can thus be rewritten as:

$$-\frac{2W}{\lambda} = N' + N_\infty - \frac{r}{\lambda}(\alpha - 2\varphi) - \frac{ru_r}{\lambda L}$$

$$-\frac{2W}{\lambda} = (N' + \eta_c) + N_\infty - \frac{r}{\lambda}(\alpha - 2\varphi) - \frac{ru_r}{\lambda L} - \eta_c \qquad \text{(IV-8)}$$

The quantity that is readily available from the fringe pattern is:

$$N' + \eta_c = N^{(o)} \tag{IV-9}$$

The reference for $N^{(o)}$ is chosen arbitrarily such as $N^{(o)}$ is as close to zero as possible for the fringe "at infinity". For the remaining angle of tilt and radial displacement, corrective terms are defined as:

$$\eta_t = -\frac{r}{\lambda}(\alpha - 2\varphi) \tag{IV-10}$$

$$\eta_r = -\frac{ru_r}{\lambda L} \tag{IV-11}$$

Equation IV-8 thus becomes:

$$\frac{-2W}{\lambda} = N^{(o)} + N_\infty + \eta_t + \eta_r - \eta_c \tag{IV-12}$$

Starting from the initially given value of $N^{(o)}$ from the fringe pattern, the following quantities are defined:

$$N^{(1)} = N^{(o)} + \eta_t \tag{IV-13}$$

$$N^{(2)} = N^{(1)} + \eta_r \tag{IV-14}$$

$$N_r = N^{(2)} - \eta_c = -\frac{2W}{\lambda} - N_\infty \tag{IV-15}$$

The normalized normal displacement to be determined then becomes:

$$\frac{W_\infty - W}{W_\infty} = \left(\frac{N}{N_\infty}\right)_r \tag{IV-16}$$

In equations IV-10 through IV-15, the fringe order $N^{(o)}$ is determined directly from the interferogram (figure 18-a), which is projected onto radial graph paper for more accuracy in the location of the fringes. Then the terms η_t, η_r, and $(-\eta_c)$ are added, yielding the fringe orders $N^{(1)}$, $N^{(2)}$, and N_r. The principal steps for determining these quantities are summarized here, and are derived in more detail in Appendix II.

1. Correction for Tilt Angle: η_t

After correction of rigid body rotations of the specimen, by adjustment of the beam splitter (Chapter III.D.2), a slight uncorrected rotation $(\alpha - 2\varphi)$ may remain. The uncorrected rotation angles about the x and y axes are determined from the remaining asymmetry of the fringe pattern. These angles are called $(\alpha - 2\varphi)_x$ and $(\alpha - 2\varphi)_y$. In cartesian coordinates, the corrective term η_t becomes:

$$\eta_t\ (x,y) \;=\; -x\ \frac{(\alpha - 2\varphi)_y}{\lambda} \;-\; y\ \frac{(\alpha - 2\varphi)_x}{\lambda} \qquad \text{(IV-17)}$$

Numerically, it is found (Appendix II) that:

$$\frac{(\alpha - 2\varphi)_x}{\lambda} \;\approx\; 0.045$$

$$\frac{(\alpha - 2\varphi)_y}{\lambda} \;\approx\; -0.031 \qquad \text{(IV-18)}$$

2. Correction for Radial Displacement: η_r

This corrective term is given by equation IV-11:

$$\eta_r \;=\; -\frac{r u_r}{\lambda L}$$

The displacement is estimated from the two-dimensional theory which gives:

$$u_r(r,\theta) = \frac{\sigma_\infty}{2E}\left\{\left[1-\nu-(1+\nu)\cos 2\theta\right]r+\left[1+\nu-4\cos 2\theta\right]\frac{a^2}{r}+\left[(1+\nu)\cos 2\theta\right]\frac{a^4}{r^3}\right\} \qquad \text{(IV-19)}$$

The numerical value of η_r is computed from this expression along the lines where the data are processed. The results are reported in tables 2 and 3. These first two corrections (η_t and η_r), together with the original fringe order $N^{(o)}$, give the value of $N^{(2)}$, which will be used in the determination of η_c:

$$N^{(2)} = N^{(o)} + \eta_t + \eta_r \qquad \text{(IV-20)}$$

3. Correction for Uniform Shift (η_c)

Once all the corrections have been made, and assuming that the condition of generalized plane stress are indeed satisfied away from the hole (cf. Chapter IV.B), N_r should approach zero "at infinity". All the values of $N^{(2)}$ are thus shifted by an amount η_c such as this result can be achieved. Practically, the values of $N^{(2)}$ are first plotted in terms of r along the axes. Then the origin of the values of $N^{(2)}$ is simply shifted by the desirable amount, such that

$$N_r = \left[N^{(2)} - \eta_c\right]$$

approaches zero as r approaches infinity.

D. Determination of the Fringe Order at Infinity

From equations III-24 and IV-2, the fringe order at infinity is:

$$N_\infty = \frac{h\nu}{\lambda E} \times \frac{P}{2bh} = \frac{\nu P}{2b\lambda E} \qquad \text{(IV-21)}$$

Where P is the difference between the reference load at which the hologram is recorded and the current load when the picture of the interferogram is taken (see Chapter II.D.1). Numerically:

$$P = 175 \pm 5 \text{ lbs.} \qquad (779 \pm 22 \text{ N})$$

Using the mechanical properties and geometric data given in table 1 and figure 19, the fringe order at infinity is found to be

$$N_\infty = 3.5 \pm 0.5 \text{ fringes} \qquad \text{(IV-22)}$$

This result will be used in the data processing along the diameter extensions and around the circle $r = a\sqrt{2}$ in the following sections.

E. Experimental Results Along the Diameter Extensions

The data along the diameter extensions are determined as follows. The intersections of bright and dark fringes with the x and y axes are determined from figure 18-a. At these points, the fringe orders $N^{(o)}$ are equal to integer number of half-fringes. $N^{(o)}$ is plotted in terms of r along the four semi-axes (figure 21). The various corrective terms η_t, η_r, and η_c are then added to each one of these original data points. The first correction η_t is obtained from

equations IV-17 and IV-18, giving the fringe order $N^{(1)}$ according to equation IV-13. The corrective term η_r/N_∞ is given by table 2. After $N^{(1)}$ has been computed, the fringe order $N^{(2)}$ is given by:

$$\frac{N^{(2)}}{N_\infty} = \frac{N^{(1)}}{N_\infty} + \frac{\eta_r}{N_\infty}$$

The values of these quantities are also given in table 4 and $N^{(2)}/N_\infty$ is plotted versus a^2/r^2 in figure 22.

The correction term η_c is determined from the asymptotic behavior of the normal displacement for large values of $r(r/a \geq 2)$, where the two- and three-dimensional theories give the same results. Before this is done, however, a comment has to be made regarding the experimental data along the axes. The normal surface displacement that is measured is considered to be due only to change in thickness of the specimen, once the influence of rigid body motions has been eliminated. Other displacements, however, may also arise from possible bending of the specimen. Actually, there is a physical reason to expect a small amount of bending in the direction of loading of the plate: any slight misalignment of the loading frame grips introduces a bending moment in that direction (i.e., the y-axis). Because of the sensitivity of the measurement technique, this bending can introduce a significant perturbation in the remote data along the y-axis. There is no physical reason, however, for any significant bending in the x-direction. Thus, the far-field data along the x-axis can be considered to be more reliable than those along the y-axis. The far-field data along the x-axis are therefore used in the determination of η_c.

Two assumptions are made in the determination of η_c, and will be considered in more detail in the discussion of the results. The first one, already mentioned in Chapter IV.B, is that $\overline{\sigma}_z$ be equal to zero away from the hole, when r approaches infinity (or, a^2/r^2 approaches zero). In this case, equation IV-16 would give:

$$\left(\frac{N}{N_\infty}\right)_r \rightarrow 0 \quad \text{as} \quad |r| \rightarrow \infty \qquad \text{(IV-23)}$$

Equation IV-23, however, cannot be used directly because the range of distances where data are collected is bounded, and hence experimental point "at infinity" is, of course, not available. The most remote experimental points are at $r/a \simeq 3$ (or, $a^2/r^2 \simeq 0.1$). The second assumption is therefore needed. It is assumed that the experimental curve obtained for $N^{(2)}/N_\infty$ (figure 22) may be extrapolated from values of a^2/r^2 greater than 0.1, down to $a^2/r^2 = 0$. By making this extrapolation for the points along the x-axis, one obtains

$$\left.\frac{N^{(2)}}{N_\infty}\right|_{r\rightarrow\infty} \simeq 0.105 \qquad \text{(IV-24)}$$

From equations IV-15 and IV-23,

$$\left.\left(\frac{N}{N_\infty}\right)_r\right|_{r\rightarrow\infty} = \left.\frac{N^{(2)}}{N_\infty}\right|_{r\rightarrow\infty} - \frac{\eta_c}{N_\infty} = 0 \qquad \text{(IV-25)}$$

Substituting equation IV-24 into equation IV-25 gives:

$$\frac{\eta_c}{N_\infty} \simeq 0.105 \qquad \text{(IV-26)}$$

This result is finally used in equation IV-15 to determine N_r:

$$\left(\frac{N_r}{N_\infty}\right)_r = \left(\frac{N}{N_\infty}\right)_r = \frac{N^{(2)}}{N_\infty} - \frac{\eta_c}{N_\infty}$$

These results are reported together with the previous ones in table 4, and are also plotted in terms of a^2/r^2 in figure 23. Because of the aforementioned uncertainty associated with specimen bending, the remote points along the y-axis ($r/a > 1.4$) are not included in this graph (figure 23).

F. Data Around the Quarter Circle ($r = a\sqrt{2}$, $0 < \theta < \pi/2$)

Figure 18 is used to determine the angle θ in terms of the fringe order around the quarter circle. The results are given in table 5. The correction for tilt is given by equation IV-17:

$$\eta_t\ (x,y) = -x\ \frac{(\alpha - 2\varphi)_y}{\lambda} - y\ \frac{(\alpha - 2\varphi)_x}{\lambda}$$

Using the results of equations IV-18,

$$\eta_t\ (\theta) = \sqrt{2}\ [0.031 \cos\theta - 0.045 \sin\theta]$$

$$\eta_t\ (\theta) = 0.044 \cos\theta - 0.064 \sin\theta$$

For the radial displacement, the correction is given in table 3. Finally, the uniform shift η_c is the same as given in equation IV-26. The results of all the corrections are reported in table 5, and the final result is plotted in figure 24 together with the theoretical results of the two- and three-dimensional analyses.

G. Discussion of the Results

In figures 23 and 24, the experimental results are compared to the surface displacements computed from the two- and three-dimensional analyses. These analytical results are derived from equations IV-4 and IV-5, where $|\cos 2\theta| = 1$ along the axes, and $a^2/r^2 = 0.5$ around the quarter circle. Figure 23 shows that agreement with the plane stress analysis is good at large distances from the hole ($r/a > 2$). The experimental results, however, depart considerably from the two-dimensional theory when the hole boundary is approached. This discrepancy increases as the distance from the hole decreases, and reaches nearly fifty percent of the experimental result, at the hole boundary. In the region close to the hole, results from the three-dimensional analysis are in good agreement with the measured surface displacements. The maximum discrepancy between the experimental and the analytical results occurs at the hole boundary and is about seven percent when the three-dimensional analysis is used. The three-dimensional analysis results are also in good agreement with the experimental data at large distances away from the hole where both analyses give the same result. The three-dimensional analysis thus appears to give good results over the whole field; whereas the two-dimensional one fits with the experiment only at large distances from the hole. This conclusion is not surprising, since the generalized plane stress hypotheses, used in the two-dimensional solution, are quite doubtful close to the hole boundary.

In this conclusion, however, the hypotheses made to determine η_c in the data processing have to be remembered. The agreement that is observed in the far field indeed arises partly from the hypotheses. In order for the experimental curve to fit the analytical ones, it must have the two following features. The curve $(N/N_\infty)_r$ versus a^2/r^2 must be a straight line with a slope equal to two in the far field, and it must go through the origin. The first one of these features clearly does not depend on restrictive hypotheses. A straight line with a slope of two is actually obtained experimentally, prior to the determination of η_c (see figure 22). But the assumption for the determination of η_c thereafter is indeed that the $(N/N_\infty)_r$ curve goes through the origin. This hypothesis is not based on any experimental evidence from the present set of data, but only on the physical reason that the state of stress "at infinity" is expected to be $\sigma_x = \sigma_z = 0$ and $\sigma_y = \sigma_\infty$. This assumption, used in data processing will have to be kept in mind when the results of reflection and transmission tests are compared in Chapter VII. Prior to this comparison, however, the analysis of the fringes in transmission has to be examined and will be discussed in the next chapter.

CHAPTER V. TRANSMISSION HOLOGRAPHIC INTERFEROMETRY

A. Introduction

In transmission holography, the object beam is no longer reflected by the object as was shown in figure 1. Instead, a transparent object is used and the object beam now passes through that object as shown in figure 25. The principle of transmission holographic interferometry is otherwise basically the same as that for reflection. In the interferometric process, comparison is made between the optical paths of the object beam through the object in two differently stressed states. This optical path difference is now caused by the thickness change of the specimen due to strains, as well as by the change in its index of refraction produced by the stress-optical effect. It is noteworthy that in this process, rigid body displacements of the specimen are not nearly so disturbing as they were in reflection. If rigid body displacement of the object reduces the optical path behind the object, for instance, it also automatically lengthens the path by the same amount in front of the object. The influence of the displacement is thereby practically self-compensating. Thus, the transmission technique is much easier to use than the reflection technique, and has now become a fairly standard procedure [6,7]. It is often used in connection with photoelasticity as a means for the separation of stresses [6]. This technique has been thoroughly investigated with photoelastic materials in connection with generalized plane stress problem. In the

present study, the influence of non-zero σ_z stresses will be taken into account. However, a simplification is introduced by the use of Plexiglas (PMMA) instead of a highly birefringent (photoelastic) material. Although Plexiglas does exhibit a significant stress-optic effect, one stress-optic coefficient is sufficient to characterize it, instead of the two coefficients needed to describe photoelastic materials. The corresponding stress-optical law will be derived. Then, an interpretation of the fringes will be given for the case of illumination perpendicular to the surface of the specimen, as shown in the interferometer sketch (figure 26). A photograph of the complete experimental set-up is shown in figure 27.

B. Stress-Optical Law in Three Dimensions

1. Secondary Principal Stresses

The optical effect related to the transmission of light through stressed transparent objects is related to the concept of secondary principal stresses. In an arbitrary set of axes x,y,z, the state of stress is defined by the six stress components σ_x, σ_y, σ_z, τ_{xy}, τ_{xz}, τ_{yz}. The secondary principal stresses for a direction z are defined as the principal stresses resulting from the stress component in the plane perpendicular to the z-direction. Denoting them by σ_{1z} and σ_{2z},

$$\sigma_{1z} = \frac{\sigma_x + \sigma_y}{2} + \frac{1}{2}\sqrt{4\tau_{xy}^2 + (\sigma_x - \sigma_y)^2}$$

$$\sigma_{2z} = \frac{\sigma_x + \sigma_y}{2} - \frac{1}{2}\sqrt{4\tau_{xy}^2 + (\sigma_x - \sigma_y)^2} \qquad \text{(V-1)}$$

2. Propagation of Polarized Light Through a Birefringent Medium

When a beam of polarized light enters a birefringent material, it is resolved into two components polarized in orthogonal directions, and transmitted at different velocities. A photoelastic material has the property of becoming birefringent when it is stressed. When a polarized beam enters a stressed photoelastic medium, it is thus resolved into two perpendicularly polarized components. When the direction of the incident light beam is along the z-axis, the new directions of polarization correspond to the directions of the secondary principal stresses σ_{1z} and σ_{2z}. The velocity of propagation of the two components of light depend on the indices of refraction n_1 and n_2 for these two components. If σ_z is the normal stress in the z-direction, and n_o the index of refraction of the material in the unstressed (stress-free) state, then the stress-optical law gives [26]:

$$\begin{aligned} n_1 - n_o &= C_1 \sigma_{1z} + C_2 (\sigma_z + \sigma_{2z}) \\ n_2 - n_o &= C_1 \sigma_{2z} + C_2 (\sigma_z + \sigma_{1z}) \end{aligned} \qquad \text{(V-2)}$$

where C_1 and C_2 are the two stress-optical coefficients of the material. The behavior of the material will now be examined in cases where the values of C_1 and C_2 are practically equal.

3. Stress-Optical Law for Non-Birefringent Materials

The stress-optical coefficients C_1 and C_2 in equations V-2 are significantly different for materials used in photoelasticity [26]. Although stress-optically sensitive, plexiglas exhibits very

little birefringence. This means that the propagation of light through plexiglas has little or no effect on its polarization, and that the coefficients C_1 and C_2 in equations V-2 are almost equal. Assuming that:

$$C_1 = C_2 = C$$

then equations V-2 show that n_1 and n_2 are also equal, with a common value n, such that:

$$n - n_o = C\,(\sigma_{1z} + \sigma_{2z} + \sigma_z)$$

Using the definition of the secondary principal stresses σ_{1z} and σ_{2z} given in equations V-1, this becomes:

$$n - n_o = C\,(\sigma_x + \sigma_y + \sigma_z) \qquad \text{(V-3)}$$

This value of the index of refraction, together with the changes in thickness of the material due to the strains, will now be used to analyze the process of fringe formation.

C. Analysis of the Fringe Orders

The interference fringes introduced by stressing a plate of thickness h are now to be interpreted for the case of an incident light perpendicular to the specimen surface. The basis for this interpretation is the comparison of the optical paths through the specimen in its stressed and unstressed states. Each of the two paths will be first compared to the optical path length with the

sample completely removed; the latter value being used as a common reference. The difference between the two results that are thereby obtained gives the optical path difference between the stressed and unstressed states. Following this procedure, the optical path increment due to the presence of the unloaded specimen is:

$$d_1 = (n_o - 1)\, h = 2 \int_0^{\frac{h}{2}} (n_o - 1)\, dz$$

In the stressed state, the optical path increment is:

$$d_2 = 2 \int_0^{\frac{h}{2} + w(\frac{h}{2})} (n - 1)\, dz$$

where $w(h/2)$ is the out-of-plane surface displacement. The expression for d_2 may be rearranged as follows:

$$d_2 = 2 \int_0^{\frac{h}{2} + w(\frac{h}{2})} [n_o - 1 + (n - n_o)]\, dz$$

$$d_2 = 2 \left[\int_0^{\frac{h}{2}} (n_o - 1)\, dz + \int_0^{\frac{h}{2}} (n - n_o)\, dz \right.$$

$$\left. + \int_{\frac{h}{2}}^{\frac{h}{2} + w(\frac{h}{2})} (n_o - 1)\, dz + \int_{\frac{h}{2}}^{\frac{h}{2} + w(\frac{h}{2})} (n - n_o)\, dz \right]$$

The difference in optical path between the stressed and unstressed states is thus:

$$\delta = d_2 - d_1$$

$$\delta = 2\left[\int_0^{\frac{h}{2}} (n - n_o)\,dz + \int_{\frac{h}{2}}^{\frac{h}{2}+w(\frac{h}{2})} (n_o - 1)\,dz + \int_{\frac{h}{2}}^{\frac{h}{2}+w(\frac{h}{2})} (n - n_o)dz\right]$$

Since $(n - n_o)$ and $w(\frac{h}{2})$ are very small quantities, the third integral may be neglected in comparison to the first two integrals. The second integral is a simple product, since $(n_o - 1)$ is a constant. Therefore:

$$\delta = 2\int_0^{\frac{h}{2}} (n - n_o)\,dz + 2\,(n_o - 1)\,w(\tfrac{h}{2}) \qquad \text{(V-4)}$$

Substituting equation V-3 for $(n - n_o)$ into equation V-4, δ then becomes:

$$\delta = 2C\int_0^{\frac{h}{2}} (\sigma_x + \sigma_y + \sigma_z)\,dz + 2\,(n_o - 1)\;\; w(\tfrac{h}{2}) \qquad \text{(V-5)}$$

The surface displacement $w(\frac{h}{2})$ may be computed from the theory of elasticity; that is:

$$w(\tfrac{h}{2}) = \int_0^{\frac{h}{2}} \epsilon_z\, d_z = \int_0^{\frac{h}{2}} \tfrac{1}{E}\left[\sigma_z - \nu(\sigma_x + \sigma_y)\right] dz$$

$$w(\tfrac{h}{2}) = \int_0^{\frac{h}{2}} \left[\frac{1+\nu}{E} \sigma_z - \frac{\nu}{E} (\sigma_x + \sigma_y + \sigma_z) \right] dz$$

Using this expression for $w(\frac{h}{2})$, equation V-5 becomes:

$$\delta = 2 \int_0^{\frac{h}{2}} \left\{ \left[C - \frac{(n_o - 1)\ \nu}{E} \right] (\sigma_x + \sigma_y + \sigma_z) + \frac{(n_o - 1)(1+\nu)}{E} \sigma_z \right\} dz \qquad (V\text{-}6)$$

The sum of the principal stresses is called Σ:

$$\Sigma = \sigma_1 + \sigma_2 + \sigma_3 = \sigma_x + \sigma_y + \sigma_z$$

The average values of Σ and σ_z through the thickness of the plate are $\overline{\Sigma}$ and $\overline{\sigma}_z$; where:

$$\overline{\Sigma} = \frac{2}{h} \int_0^{\frac{h}{2}} \Sigma\ (z)\ dz$$

$$\overline{\sigma}_z = \frac{2}{h} \int_0^{\frac{h}{2}} \sigma_z\ (z)\ dz$$

Equation V-6 thus gives:

$$\delta = h \left\{ \left[C - \frac{(n_o - 1)\ \nu}{E} \right] \overline{\Sigma} + \frac{(n_o - 1)(1+\nu)}{E} \overline{\sigma}_z \right\} \qquad (V\text{-}7)$$

From equation II-15, the fringe order is:

$$N = \frac{\delta}{\lambda}$$

$$N = h \left\{ \left[\frac{C}{\lambda} - \frac{(n_o - 1)\,\nu}{\lambda E} \right] \bar{\Sigma} + \frac{(n_o - 1)(1 + \nu)}{\lambda E}\, \bar{\sigma}_z \right\} \qquad \text{(V-8)}$$

The stress state "at infinity" is defined by $\sigma_y = \sigma_\infty$, and $\sigma_x = \sigma_z = 0$. The corresponding fringe order "at infinity" is thus

$$N_\infty = F\, h\, \sigma_\infty \qquad \text{(V-9)}$$

where

$$F = \frac{C}{\lambda} - \frac{(n_o - 1)\,\nu}{\lambda E} \qquad \text{(V-10)}$$

A constant H is also defined as:

$$H = \frac{(n_o - 1)(1 + \nu)}{\lambda E} \qquad \text{(V-11)}$$

Equation V-8 then becomes:

$$N = h \left[F\, \bar{\Sigma} + H\, \bar{\sigma}_z \right] \qquad \text{(V-12)}$$

The constants F and H depend on the mechanical and optical properties of the material, and on the light wavelength. The constant H can be easily computed from readily available data. But the constant F involves the stress-optic coefficient C, wich is seldom used and may not be available. A calibration test is thus usually necessary to determine F. In the case of a plate under tension, the experimental data are obtained by counting fringes from the fringe

"at infinity". As in the case of reflection holographic interferometry, this procedure gives only the relative fringe order $(N - N_\infty) = N'$. It is convenient to normalize it with respect to N_∞. The relative normalized transmission fringe order will thus be defined as:

$$\left(\frac{N}{N_\infty} \right)_t = \frac{N - N_\infty}{N_\infty} \qquad \text{(V-13)}$$

Using equations V-9 and V-12, equation V-14 becomes:

$$\left(\frac{N}{N_\infty} \right)_t = \frac{\bar{\Sigma} - \sigma_\infty}{\sigma_\infty} + \frac{H}{F} \frac{\bar{\sigma}_z}{\sigma_\infty} \qquad \text{(V-14)}$$

which is the final form that will be used in the presentation of the results obtained in the circular hole problem. Before presenting these results, however, it is appropriate to check more closely the physical meaning of the equations that have been derived.

D. Physical Interpretation of the Fringes

From the fringe order equation V-12, it is seen that the fringes represent lines where the linear combination of the average stresses has a constant value. This definition of the fringes is more general than in the standard formulation for the separation of stresses in photoelasticity, where the problem is considered to be one of generalized plane stress. In which case $\sigma_z = 0$, and the in-plane stresses are considered to be constant through the thickness:

$$\bar{\sigma}_z = \sigma_z = 0$$

$$\bar{\Sigma} = (\bar{\sigma}_x + \bar{\sigma}_y + \bar{\sigma}_z) = \bar{\sigma}_x + \bar{\sigma}_y = \sigma_x + \sigma_y$$

$$\bar{\Sigma} = \sigma_1 + \sigma_2$$

Equation V-12, for generalized plane stress, is thus reduced to:

$$N = F h (\sigma_1 + \sigma_2) \qquad \text{(V-15)}$$

which gives the sum of the principal stresses. Since the photoelastic technique gives their difference $(\sigma_1 - \sigma_2)$, two independent equations are available to determine the principal stresses σ_1 and σ_2. In this procedure, the interference fringes are referred to as "isopach" lines, which are lines of constant change in thickness, and of constant sum of the principal stresses. However, this approach is valid only when the generalized plane stress conditions are realized. In particular, its legitimacy is questionable when stress concentrations in plates are to be studied, since a very significant departure from the generalized plane stress conditions usually occurs in these cases. Equation V-12 should then be used instead of V-15, which will be done in the following study of stress concentrations around a hole in a plate.

CHAPTER VI. ANALYSIS OF STRESSES AROUND A CIRCULAR HOLE BY TRANSMISSION HOLOGRAPHIC INTERFEROMETRY

A. Introduction

The transmission technique described in Chapter V was applied with the same Plexiglas sample used in the reflection test of Chapter IV. (This transmission test was in fact carried out before the reflection one, since for the latter experiment the specimen surface had to be painted). The interferometer that was used is illustrated in figures 26 and 27. The interferogram that was obtained is shown in figure 28. Equation V-14 was used for the interpretation of the fringes. The constants F and H in this equation were first determined; by direct computation for H, and by a calibration test for F. This value of F was used to compute the fringe order at infinity N_∞. Then, the data from the hologram were processed on the diameter extensions, along the x and y axes (figure 19).

B. Determination of the Constants F, H and N_∞

1. Determination of H

The coefficient H in equation V-14 is given by equation V-11. All the quantities on the right-hand side are known and reported in table 1. The constant H can thus be computed directly:

$$H = \frac{(n_o - 1)(1 + \nu)}{\lambda E} = (0.081 \pm 0.009) \text{ fringe - in./lb.} \qquad \text{(VI-1)}$$

$$= (0.79 \pm 0.08) \text{ fringe - m/N}$$

2. Determination of F

The coefficient F is given by equation V-10:

$$F = \frac{C}{\lambda} - \frac{(n_o - 1)\,\nu}{\lambda E}$$

Unlike H, however, F could not be computed directly, because the constant C is seldom used, and its numerical value was not available. A calibration test had thus to be made. For this test, a four-point bending specimen, made from the same PMMA sheet used for the circular hole specimen, was used (figure 29). The procedure is described in detail in Appendix III and gives the following result for the absolute value of F:

$$\begin{aligned} |F| &= (0.034 \pm 0.003) \quad \text{fringe - in./lb.} \\ &= (0.30 \pm 0.03) \quad \text{fringe - m/N} \end{aligned} \tag{VI-2}$$

Since it is physically impossible to determine the sign of fringe orders in the test, this procedure does not give the sign of F, which has to be determined separately. The sign is determined by considering equation V-10 again. The stress-optical coefficient C has basically a negative value [5]. The index of refraction n_o is always greater than unity. Therefore, both terms in the right-hand side of equation V-10 are negative, and F has to be negative. The final result for F is thus:

$$\begin{aligned} F &= -(0.034 \pm 0.003) \quad \text{fringe - in./lb.} \\ &= -(0.30 \pm 0.03) \quad \text{fringe - m/N} \end{aligned} \tag{VI-3}$$

3. Comparison with Other Reported Data for "F"

It would now be interesting to check this value of F against values of the same quantity obtained from other sources. As it was said previously, the value of C would be needed for a direct computation of F; but it is not available. It is recalled (see Chapter V.C) that the coefficient C has the common value of the stress-optic coefficients C_1 and C_2 in equations V-2, in the case of a material with little or no birefringence. In this case, which occurs for Plexiglas, $C_1 \simeq C_2$, and C can be taken approximately as:

$$C = \frac{C_1 + C_2}{2} \qquad \text{(VI-4)}$$

Values of C_1 and C_2 are reported by Nisida and Saito [5] for some Plexiglas illuminated with a light of wavelength $\lambda = 0.546$ μm (Mercury vapor lamp). These values may not be appropriate for the wavelength of light and Plexiglas used in the present test. However, they can be used to check the order of magnitude of the calibration test results. According to reference 5:

$$C_1 = -33.1 \text{ Brewsters}$$

$$C_2 = -28.2 \text{ Brewsters}$$

Taking $C = (C_1 + C_2)/2$, then

$$C = -30.65 \text{ Brewsters}.$$

It is recalled that:

$$1 \text{ Brewster} = 10^{-13} \text{ cm}^2/\text{dyne} = 0.6897 \times 10^{-8} \text{ in}^2/\text{lb}.$$

Using these numerical values, equation VI-1 gives:

$$F = -0.028 \text{ fringe - in./lb.} = -0.25 \text{ fringe - m/N}$$

which is seen to have the same order of magnitude as the calibration test result. The value of F given by equation VI-3 will thus be used to determine the fringe order at infinity (N_∞).

4. Determination of N_∞

The fringe order N_∞ is determined from equation V-9:

$$N_\infty = F h \sigma_\infty$$

The stress σ_∞ is determined from the difference P between the "reference" load (when the reference hologram was made), and the current load for producing the real-time interferogram (see Chapter II.D.1). In the present experiment, this difference was P = -350 lbs. The width of the specimen is 2b. Then:

$$\sigma_\infty = P/2 b h$$

$$N_\infty = \frac{FP}{2b}$$

Numerically:

$$F = -0.034 \text{ fringe - in./lb.} = -0.30 \text{ fringe - m/N}$$

$$P = -(350 \pm 5) \text{ lbs.} = -(1560 \pm 20) \text{ N}$$

$$b = (1.00 \pm 0.005) \text{ in.} = (25.40 \pm 0.13) \text{ mm}$$

Which gives:

$$N_\infty = (5.95 \pm 0.6) \text{ fringes} \qquad \text{(VI-5)}$$

This value of N_∞, together with the values of F and H given by equations VI-3 and VI-2, is now used to process the data along the diameter extensions.

C. Data Along the Diameter Extensions

The data processing procedure in transmission is much simpler than it is in reflection, since no correction for tilt angle or radial displacement is necessary. As it was done for the reflection interferogram (figure 21), the transmission fringe order is plotted in terms of the distance along the four semi-axes. Smooth curves are fitted through the experimental points. The average absolute value of the fringe orders along the four semi-axes is then determined for a number of values of r/a. The fringe order is then determined along each of the four semi-axes by interpolation from the fitted curves. The values of r/a chosen for this procedure are those where the reflection fringe order is already available (from Chapter IV), so that a comparison of reflection and transmission data can be made. The average values of the fringe order are then normalized with respect to N_∞, which gives the normalized fringe order $| (N/N_\infty)_r |$ in terms of the distance r/a. These results are reported in table 6. For convenience in making comparison with the analytical results, the fringe order is then plotted versus the inverse square of the distance (a^2/r^2) (figure 30).

D. Comparison with the Analyses and Discussion of the Results

In figure 30, the experimental results are compared to the fringe orders computed from the two- and three-dimensional analyses. These analytical results are obtained as follows.

1. Transmission Fringe Order from the Generalized Plane Stress Analysis

In the two-dimensional generalized plane stress analysis, $\bar{\sigma}_z$ is assumed to be zero. The transmission fringe order in equation V-15 thus becomes:

$$\left(\frac{N}{N_\infty}\right)_t = \frac{\bar{\Sigma} - \sigma_\infty}{\sigma_\infty} \qquad \text{(VI-6)}$$

Using the analytical stress distribution of equations A-1 in Appendix I, equation VI-6 gives:

$$\left(\frac{N}{N_\infty}\right)_t = \frac{2a^2}{r^2} \cos 2\theta \qquad \text{(VI-7)}$$

Along the axes, $|\cos 2\theta| = 1$, and the normalized fringe order becomes:

$$\left|\left(\frac{N}{N_\infty}\right)_t\right| = \frac{2a^2}{r^2} \qquad \text{(VI-8)}$$

2. Transmission Fringe Order from the Three-Dimensional Analysis

For comparison with the experimental results, the same approximation, as in the reflection case, is made regarding the three-dimensional theory. The average in-plane stresses are considered to be practically the same in the three-dimensional analysis as they are

in generalized plane stress. The significant difference between the two analyses comes from σ_z. The average value of σ_z through the thickness is given by equation A-8 in Appendix I:

$$\bar{\sigma}_z = [\sigma_\infty \cos 2\theta]\, \eta(r/a)$$

Using this expression for $\bar{\sigma}_z$ and the generalized plane stress expressions of equations A-1 for σ_x and σ_y, equation V-15 becomes:

$$\left(\frac{N}{N_\infty}\right)_t = \left\{\left[\frac{2a^2}{r^2} + \eta\left(\frac{r}{a}\right)\right] + \frac{H}{F}\,\eta\left(\frac{r}{a}\right)\right\} \cos 2\theta$$

Along the axes:

$$\left|\left(\frac{N}{N_\infty}\right)_t\right| = \frac{2a^2}{r^2} + \left(\frac{H}{F} + 1\right)\eta\left(\frac{r}{a}\right) \qquad \text{(VI-9)}$$

The values of F and H in equation VI-9 are given by equations VI-1 and VI-3. These values are substituted into equation VI-9, and the result is plotted in figure 30.

3. Discussion of the Results

The results obtained from this transmission test lead to conclusions somewhat similar to those of the reflection test. In the far field where the two- and three-dimensional analyses give identical results, the experiment is in very good agreement with this common analytical result. When the hole boundary is approached ($r/a < 2$), the experimental result departs increasingly from the two-dimensional analytical result. This discrepancy is maximum at the hole boundary, where it is about thirty percent of the experimental

result. In the region close to the hole, results from the three-dimensional analysis are in good agreement with the experimental data. The discrepancy that is observed does not exceed five percent.

These observations give further support to the validity of the generalized plane stress analysis in the far field only, and to the necessity of using a three-dimensional analysis close to the hole. This difference between the close and the far field is emphasized in the next chapter, where the stress $\bar{\sigma}_z$ is estimated by comparing the results of the reflection and transmission tests.

CHAPTER VII. COMBINATION OF REFLECTION AND TRANSMISSION HOLOGRAPHIC INTERFEROMETRY

A. Introduction

The fringe patterns obtained by reflection and transmission holographic interferometry have been presented and analyzed in Chapters IV and VI. As seen from figures 18-a and 28, the fringe patterns obtained with the two techniques look fairly similar. Indeed, the fringes are, in first approximation, lines of equal change in thickness in each case. In the reflection procedure, a systematic discrepancy arises from radial displacements due to strains and an accidental one from imperfect correction of rigid body displacements, as seen in Chapter IV. These discrepancies between the actual fringes and the lines of equal change in thickness are small close to the hole, and increase with the distance away from the hole. In the transmission technique, rigid body displacements and radial displacements have little or no influence, but a discrepancy comes from the variation in the index of refraction caused by stress in the thickness direction. This discrepancy increases as the distance to the hole decreases. The interpretation of the fringes is thus not quite the same in the two cases, and it is possible to take advantage of this difference to obtain some additional information about the stresses. As it will be shown, it is actually possible to evaluate separately the through-the-thickness average values of the z-stress ($\overline{\sigma}_z$), and of the sum of the principal stresses ($\overline{\sigma_x + \sigma_y + \sigma_z}$).

It will be shown first that the fringe orders in reflection and transmission, $(\frac{N}{N_\infty})_r$ and $(\frac{N}{N_\infty})_t$, can be expressed then provide two unknowns, $\bar{\sigma}_z$ and $(\overline{\sigma_x+\sigma_y+\sigma_z})$. These expressions then provide two independent equations that can be used to determine these two unknowns. This procedure will first be analyzed and applied numerically in the case of the circular hole. An attempt will then be made to develop a procedure to test the regions of a plate where the generalized plane stress hypotheses are valid. It appears that at least a necessary condition can be defined which is that $\bar{\sigma}_z$ be zero. The practical methods to test for this condition will be presented, and these methods will be applied to the circular hole problem. It will be seen at that stage that two conclusions are reached, from the comparison between the experimental results and the three-dimensional analysis: (1) the experiments confirms the analytical results regarding the distance from the hole where the plane stress analysis becomes valid; and (2) the experiment also confirms the trend predicted by the Alblas analysis for the stresses and displacements close to the hole.

In the last part of this chapter, attention will be focused on the region near the hole. The purpose of this part is to determine whether the results of the Alblas analysis are consistent with the experimental results. However, a new approach will be used in this section. Thus far, measurements were made over the whole range of distances from the hole boundary to the far field. The values of N_∞ used were determined independently and were then used in data processing as normalization factors to give $(N/N_\infty)_r$ and $(N/N_\infty)_t$.

The experimental data obtained by this first approach were found to be close to the analytical results. In the new approach, the analytical solution will be assumed to be exact in the far field; i.e., for $r/a > 2$. The value of N_∞ will be selected for each interferogram so that the experimental points best fit this far-field analytical solution. The values of N_∞ found by this method can be expected to be slightly different from the ones that were determined previously by independent computation or calibration. This procedure represents a "self-calibration" of the experiment, since the value of N_∞ is obtained from the fringe pattern data only. Uncertainties related to the previous independent determination of N_∞ are thus eliminated, and the value of N_∞ thereby obtained can be expected to be more accurate.

B. Measurements of Stresses from the Fringe Orders

In the approach used so far, the fringe order was analyzed in terms of average stresses for the transmission technique, and of surface displacement for reflection. An equation for the reflection fringe order in terms of the stresses will be derived first in this section. This new reflection equation, together with that for transmission, can then be solved to obtain the two quantities $\overline{\sigma}_z$ and $\overline{\Sigma} = \overline{(\sigma_x + \sigma_y + \sigma_z)}$. The expressions thereby obtained for the stresses will be presented, and their coefficients computed numerically for the material (PMMA) that was used. The quantities $\overline{\sigma}_z$ and $\overline{\Sigma}$ will finally be

evaluated along the x-axis by this method and compared to their predicted values from the two- and three-dimensional analyses.

1. Interpretation of the Fringes in Terms of the Stresses

a. Transmission Interferometry

The analysis of the transmission fringes is given in Chapter V in a form that is readily usable for the present purpose. From equation V-14, the normalized transmission fringe order is:

$$\left(\frac{N}{N_\infty}\right)_t = \frac{\bar{\Sigma} - \bar{\sigma}_\infty}{\sigma_\infty} + \frac{H}{F}\,\frac{\bar{\sigma}_z}{\sigma_\infty} \qquad \text{(VII-1)}$$

Where:

$$\bar{\Sigma} = \overline{(\sigma_x + \sigma_y + \sigma_z)} \qquad \text{(VII-2)}$$

b. Reflection Interferometry

In reflection, the analysis of Chapter IV has to be extended to provide a useful comparison with the results of the transmission technique. From equation IV-16, the reflection fringe order has been shown to be:

$$\left(\frac{N}{N_\infty}\right)_r = \frac{W_\infty - W}{W_\infty} \qquad \text{(VII-3)}$$

The normal surface displacements W and W_∞ can be computed in terms of the average stresses, from equations A-7 and A-8 in Appendix I:

$$W_\infty - W = \frac{h}{2E}\left[\bar{\sigma}_z - \nu(\bar{\sigma}_x + \bar{\sigma}_y - \sigma_\infty)\right] \qquad \text{(VII-4)}$$

$$W_\infty = -\frac{\nu h\,\sigma_\infty}{2E} \qquad \text{(VII-5)}$$

Equations VII-3, VII-4 and VII-5 yield:

$$\left(\frac{N}{N_\infty}\right)_r = \frac{\bar{\Sigma} - \sigma_\infty}{\sigma_\infty} - \frac{1+\nu}{\nu}\,\frac{\bar{\sigma}_z}{\sigma_\infty} \qquad \text{(VII-6)}$$

Equations VII-1 and VII-6 give two independent relations between the stress-related quantities $\bar{\sigma}_z$ and $\bar{\Sigma}$, in terms of the reflection and transmission fringe orders. Solving these two equations for $\bar{\sigma}_z$ and $\bar{\Sigma}$ gives:

$$\frac{\bar{\sigma}_z}{\sigma_\infty} = \left[\left(\frac{N}{N_\infty}\right)_t - \left(\frac{N}{N_\infty}\right)_r\right]\left[\frac{H}{F} + \frac{1+\nu}{\nu}\right]^{-1} \qquad \text{(VII-7)}$$

$$\frac{\bar{\Sigma} - \sigma_\infty}{\sigma_\infty} = \left[\frac{1+\nu}{\nu}\left(\frac{N}{N_\infty}\right)_t + \frac{H}{F}\left(\frac{N}{N_\infty}\right)_r\right]\left[\frac{H}{F} + \frac{1+\nu}{\nu}\right]^{-1} \qquad \text{(VII-8)}$$

The coefficients in these equations are now to be evaluated numerically.

2. Numerical Coefficients in the Equations

The constants F and H in equations VII-7 and VII-8 have been defined in Chapter V, by equations V-10 and V-11. Their numerical values have been given in equations VI-1 and VI-3. Using also the value of ν in table 1, equations VII-7 and VII-8 become:

$$\frac{\bar{\sigma}_z}{\sigma_\infty} = 0.61\left[\left(\frac{N}{N_\infty}\right)_t - \left(\frac{N}{N_\infty}\right)_r\right] \qquad \text{(VII-9)}$$

$$\frac{\bar{\Sigma} - \sigma_\infty}{\sigma_\infty} = 2.44\left(\frac{N}{N_\infty}\right)_t - 1.44\left(\frac{N}{N_\infty}\right)_r \qquad \text{(VII-10)}$$

These equations can now be used to evaluate the stresses along the axes, using the results of the transmission and reflection tests for $(N/N_\infty)_t$ and $(N/N_\infty)_r$.

3. Stresses along the x Axis

Equation VII-9 provides a way of estimating the average value of σ_z in terms of the transmission and reflection fringe orders. Using in equation VII-9 the results plotted in figures 23 and 30 for $(N/N_\infty)_r$ and $(N/N_\infty)_t$, the experimental values of $\overline{\sigma}_z/\sigma_\infty$ were determined along the x-axis, and are plotted in figure 31. For comparison, the results of the Alblas analysis [25] are also plotted in terms of the distance along the x-axis. The Alblas result is represented by the dashed curve in figure 31. This curve is the same as that given by figure 20, with only a change in the distance-related variable, from r/a in figure 20 to a^2/r^2 in figure 31. For generalized plane stress, $\overline{\sigma}_z/\sigma_\infty$ is zero by definition. This value is also shown in figure 31 for comparison with the experiment. The results show, once again, good agreement between the experiment and the three-dimensional analysis over the whole distance range, whereas the agreement with the two-dimensional analysis is good only at large distances away from the hole.

For reference, equation VII-10 was also used to determine the sum of the principal stresses at the two points of intersection of the hole boundary with the x-axis. At these points, the Alblas analysis gives:

$$(\overline{\sigma}_x + \overline{\sigma}_y)/\sigma_\infty = 3.02$$

$$\bar{\sigma}_z/\sigma_\infty = 0.17$$

From these results, the left-hand side in equation VII-10 is found to be:

$$\frac{\bar{\Sigma} - \sigma_\infty}{\sigma_\infty} = 2.19 \qquad \text{(VII-11)}$$

The generalized plane stress theory, on the other hand, would give:

$$(\sigma_x + \sigma_y)/\sigma_\infty = 3.00$$

$$\sigma_z = 0$$

and hence:

$$\frac{\bar{\Sigma} - \sigma_\infty}{\sigma_\infty} = 2.00 \qquad \text{(VII-12)}$$

Using the experimental values of the fringe orders in equation VII-10, the experimental result is found to be:

$$\frac{\bar{\Sigma} - \sigma_\infty}{\sigma_\infty} = 2.23$$

The nominal experimental value is indeed very close to the result of the three-dimensional analysis. However, the uncertainty on this experimental value will be seen to be very large (see the following section D), so that the range of uncertainty might also include the result of the two-dimensional analysis, equation VII-12. So, the experimental determination of $\bar{\Sigma}$ cannot be considered to be conclusive, as far as the comparison between the two- and three-dimen-

sional analyses is concerned. The result of the determination of $\bar{\sigma}_z/\sigma_\infty$ is much better and can be used more usefully to explain the problem of the validity of the generalized plane stress hypotheses, which will be done in the next section.

C. A Condition of Validity for the Generalized Plane Stress Hypotheses

Two interferograms, obtained by reflection and transmission holographic interferometry for a circular hole in a plate, have been analyzed in Chapters IV and VI. In both cases, the results were found to be consistent with the generalized plane stress analysis in the far-field region, however, a three-dimensional analysis was necessary to account for the observed fringe orders close to the hole boundary. These observations are in agreement with the assumption that is often made in the analysis of relatively thin plates subjected to in-plane loading [27]. In these cases, the hypotheses of generalized plane stress are usually considered to be valid away from regions of stress concentrations (i.e., holes, notches, cracks, etc.); but in regions close to stress concentrations, the generalized plane stress hypotheses becomes more and more doubtful when the plate thickness increases. The validity of these hypotheses can be checked analytically only by comparison to the results of a complete three-dimensional analysis. But such results are available only in a very limited number of cases. The technique developed in the present work provides a useful way for testing the generalized plane stress

analysis experimentally. The criterion that is retained involves the average z-stress ($\overline{\sigma}_z$). Satisfaction of this criterion, however, will be seen to constitute only one necessary condition for the hypotheses of plane stress to be valid. The practical testing methods using this criterion will then be explained in the case of either transparent or reflecting materials. The circular hole data will finally be used to illustrate the application of these techniques.

1. The Average z-Stress Criterion

As it has been stated previously, the basic assumptions for generalized plane stress analysis are that all the stresses involving the z coordinate (in the thickness direction) be zero, and that the in-plane stresses be constant through the thickness (i.e., independent of z):

$$\sigma_z = \tau_{xz} = \tau_{yz} = 0 \qquad \text{(VII-14)}$$

$$\sigma_x = \sigma_x (x,y) \qquad \text{(VII-15)}$$

$$\sigma_y = \sigma_y (x,y) \qquad \text{(VII-16)}$$

$$\tau_{xy} = \tau_{xy} (x,y) \qquad \text{(VII-17)}$$

Among these six stress components, the holographic interferometry technique is sensitive only to the three normal stresses σ_x, σ_y and σ_z. The fringe orders in reflection and transmission are related to the through-thickness average value of these stresses, equations

VII-1 and VII-6. Although the fringe order depends on σ_x and σ_y, this dependence cannot be used to check the validity of equations VII-15 and VII-16, because a knowledge of $\overline{\sigma}_x$ and $\overline{\sigma}_y$ does not give any information on the distribution of these stresses in the thickness direction. The only useful information that can be obtained about the validity of equations VII-14 to VII-17 comes thus from σ_z. If $\sigma_z = 0$, in equation VII-14, then $\overline{\sigma}_z = 0$. The condition $\overline{\sigma}_z = 0$ is thus a necessary but not sufficient condition for the generalized plane stress hypotheses to be valid. The distance from the stress concentration, within which a three dimensional analysis is necessary is thus greater than or equal to the distance where $\overline{\sigma}_z$ becomes zero. The practical ways to determine where this condition is satisfied is now going to be examined for the cases of transparent and nontransparent materials.

2. Case of a Transparent Material

In the case of a transparent material, both the reflection and transmission techniques can be used, the specimen being painted for the reflection test. The procedure described in the last section, B, can be used directly to estimate $\overline{\sigma}_z$, as was done for the circular hole problem (figure 1).

3. Case of a Nontransparent Material

The aforementioned direct procedure, however, cannot be used with a reflecting specimen, because the transmission fringe order is not available as no transmission test can be made with the sample. The quantity $(N/N_\infty)_t$ in equation VII-7 thus remains unknown, and $\overline{\sigma}_z$

cannot be evaluated directly. However, it is still possible to make a transparent model of the actual specimen to run a transmission test. It can be shown that the result of such a transmission test can be used for the present purpose, provided that the transparent specimen is thin enough. The transmission fringe order equation (equation VII-1) is recalled to be:

$$\left(\frac{N}{N_\infty}\right)_t = \frac{\bar{\Sigma} - \sigma_\infty}{\sigma_\infty} + \frac{H}{F}\,\frac{\bar{\sigma}_z}{\sigma_\infty}$$

When $\bar{\sigma}_z = 0$, this equation becomes:

$$\left(\frac{N}{N_\infty}\right)_t = \frac{\bar{\Sigma} - \sigma_\infty}{\sigma_\infty}$$

Likewise, the reflection equation (VII-6), when $\bar{\sigma}_z = 0$, becomes:

$$\left(\frac{N}{N_\infty}\right)_r = \frac{\bar{\Sigma} - \sigma_\infty}{\sigma_\infty}$$

The condition $\bar{\sigma}_z = 0$ is thus equivalent to the condition that the normalized fringe orders in reflection and transmission be equal:

$$\left(\frac{N}{N_\infty}\right)_r = \left(\frac{N}{N_\infty}\right)_t \qquad \text{(VII-18)}$$

The reflection and transmission tests are thus made and the fringe orders are compared. As soon as the stress concentration is approached closely enough for the fringe orders to be different, then $\bar{\sigma}_z$ is no longer zero for at least one of the samples. It then remains to make sure that the departure from $\bar{\sigma}_z = 0$, when approaching

the stress concentration, occurs first in the reflection specimen. This can be achieved by making the transparent model much thinner than the actual specimen. In other words, the transmission fringe order for the thin model can then be considered to give the generalized plane stress fringe order. This value is the same in reflection and transmission. Comparison with the reflection fringe order shows the point of departure from plane stress in the reflection sample. This method will be used in chapter VIII in the case of a cracked sample. The aforementioned method of direct evaluation of σ_z is now going to be illustrated by the circular hole example.

4. Application to the Circular Hole Problem

The possibility of using a zero-value test on $\bar{\sigma}_z$ was envisioned in the beginning of this section as a possible method for determining the regions where the generalized plane stress analysis is valid. It was seen that a necessary condition for this validity is that $\bar{\sigma}_z$ be equal to zero. The practical ways of performing the test were discussed in the case of either a transparent or a non-transparent material. The results that have been obtained for the circular hole problem can be readily used for an example of application to a transparent material. The value of $\bar{\sigma}_z/\sigma_\infty$ has been determined experimentally along the x-axis, and are shown in figure 31. This determination shows that $\bar{\sigma}_z$ is zero in the far field, for $r/a > 2$. A comparison of the fringe orders in reflection and transmission gives the same result:

$$\left(\frac{N}{N_\infty}\right)_r = \left(\frac{N}{N_\infty}\right)_t$$

for $r/a > 2$, as can be seen from figures 23 and 30. The same result is thus obtained from both testing procedures, either direct determination of $\overline{\sigma}_z$, or comparison of the reflection and transmission fringe orders. This common result agrees with the Alblas three-dimensional analysis, whose results become identical to the generalized plane stress analysis at $r/a > 2$. The test for the zero-value of $\overline{\sigma}_z$ seems thus to give a good estimate of the regions of generalized plane stress, at least in the particular case that was studied. In this case, the condition that $\overline{\sigma}_z = 0$ seems to be not only necessary, but also sufficient. In the next section, the generalized plane stress analysis will thus be assumed to be exact for $r/a > 2$. The results obtained from this assumption will be used for a more accurate evaluation of N_∞, in order to define the stresses close to the hole more precisely. An estimate of the confidence interval on the displacements and stresses will also be given.

D. Data Processing with Self-Calibration

In chapter IV (sections E and G), it was emphasized that the expected relationship between $(N/N_\infty)_r$ and a^2/r^2 was a straight line through the origin, with a slope of two. The linearity and slope were observed to be fairly well satisfied. The zero value for the intercept at $a^2/r^2 = 0$ (that is, at $r = \infty$), however, could not be verified independently, and had to be forced by the adjustment of an otherwise unknown constant (η_c) during data processing. Together with the intercept, the slope of the linear portion of the curve in the

far-field region is now going to be forced to assume its theoretical value. The legitimacy of this procedure is supported by the identity of the results of both analyses in this region, and by the fairly good agreement of the experimental results with these two analyses. The very slight discrepancy between theories and experiment can thus be attributed to experimental errors. The largest of these is expected to be the systematic error on N_∞, introduced by the independent calibration or computation for N_∞. This systematic error can be reduced by determining N_∞ directly from the fringe pattern. The remaining error in the far-field region is then assumed to be only a random experimental error. The random experimental error on the fringe order in the linear (far field) part of the N/N_∞ versus a^2/r^2 curve is also used, to determine a confidence interval on the slope of this linear part. This, in turn, provides the confidence interval on the new value of N_∞.

This data processing procedure will be used to analyze both the reflection and transmission test results. The new values of N_∞ obtained by forcing the slopes will be used to reprocess the data presented in figures 23, 30 and 31. The confidence intervals on N_∞ will also be used to determine the confidence intervals on the new experimental results, for fringe orders (figures 32 and 33) or stresses (figure 34). In the case of the reflection hologram, first, the aforementioned procedure gives the following results.

1. Self-Calibration for the Reflection Test

The numerical values plotted in figure 23 are reported in table 4. The points used to force the slope are the points beyond

$r/a = 2$ along the x-axis ($\theta = 0,\pi$). From table 4-a, the coordinates of these points are:

r/a	a^2/r^2	$(N/N_\infty)_r$
2.02	0.245	0.508
2.28	0.192	0.411
2.37	0.178	0.371
2.77	0.130	0.286
3.00	0.111	0.244

The best fitting straight line through these points has a slope of 1.97, which is indeed fairly close to the slope 2.00 that is expected. The value of N_∞ used in the original data processing of chapter IV is $N_\infty = 3.5$. In order for the slope to be forced to assume its theoretical value of 2.00, N_∞ has to be readjusted to $N_\infty \simeq 3.45$. The entire data processing procedure of chapter IV is then repeated with the new value of N_∞, for the points along the x-axis. The new coordinates of the remote points are:

r/a	a^2/r^2	$(N/N_\infty)_r$
2.02	0.245	0.488
2.28	0.192	0.389
2.37	0.178	0.349
2.77	0.130	0.262
3.00	0.111	0.220

The slope of the best fit straight line through these points is now 1.995, and the 95% confidence interval on the slope is 0.15 (i.e., 7.5% of the nominal value of the slope). This, in turn, gives a 95% confidence interval on N_∞ of approximately 0.25. The self-calibration procedure therefore gives:

$$N_\infty = 3.45 \pm 0.25 \qquad \text{(VII-19)}$$

The results obtained with this nominal value and confidence interval on N_∞ are plotted in figure 32.

2. Self-Calibration for the Transmission Test

The slope forcing procedure for the transmission test is roughly similar to the reflection one. In the far field ($r/a > 2$), the fringe orders are given by the five last values presented in table 6:

r/a	a^2/r^2	| N |
2.02	0.245	2.90
2.28	0.192	2.29
2.37	0.178	2.15
2.77	0.130	1.56
3.00	0.111	1.31

The resulting slope with a 95 percent confidence interval is:

$$\frac{\Delta N}{\Delta(\frac{a}{r}^2)} = 11.84 \pm 0.49$$

The slope of the normalized fringe order is forced to be:

$$\frac{\Delta(\frac{N}{N_\infty})}{\Delta(\frac{a}{r}^2)} = 2.00$$

This condition requires that:

$$N_\infty = 5.92 \pm 0.25 \qquad \text{(VII-20)}$$

The results of figure 30 are thus processed again with this value of N_∞, and plotted in figure 33, along with the two- and three-dimensional analytical results. The new reflection and transmission data with slope forcing can now be compared for the determination of $\overline{\sigma}_z$.

3. Comparison of Reflection and Transmission Data

The comparison of the fringe orders to determine $\overline{\sigma}_z$ is exactly the same as described in chapter VII.B.3. Equation VII-9 is used again:

$$\frac{\overline{\sigma}_z}{\sigma_\infty} = 0.61 \left[\left(\frac{N}{N_\infty}\right)_t - \left(\frac{N}{N_\infty}\right)_r \right]$$

The only change that is introduced is in the numerical values of the fringe order. These results can be expected to be more accurate, assuming that the far-field analytical solutions are exact. The new results obtained by this method are shown in figure 34, with their confidence interval. The analytical results are also plotted on this graph.

4. Conclusions

From figure 34, it is seen that the results of the Alblas analysis are clearly within the 95% confidence interval for the experimental result, whereas the generalized plane stress result is not within that interval in the near field. This provides more evidence for the failure of the generalized plane stress analysis to predict the stresses close to the hole. As far as the three-dimensional analysis is concerned, its results are fairly close to the measured ones. Considering the uncertainty on the experimental measurements, the agreement can be considered to be quite good. Within their accuracy, the set of data that were obtained can thus be considered to be quite consistent with the Alblas analysis.

CHAPTER VIII. APPLICATION OF HOLOGRAPHIC INTERFEROMETRY TO FRACTURE MECHANICS

A. Introduction

A new technique of stress analysis by holographic interferometry has been developed in this work, and an example of its use has been given in the case of a circular hole in a plate. This example was chosen because of the availability of complete two- and three-dimensional solutions that were used for comparison with the experimental results. The good agreement between the experimental and analytical results demonstrates the reliability of the technique. However, other experimental stress analysis methods could indeed have been used for the same problem. Among the most straightforward possibilities, strain gages can provide useful informations. Photoelasticity can also be used; the "stress freezing" technique has long been proven to be a valuable tool for the study of three-dimensional stress distributions. In some problems, however, the experimental requirements are so severe that the conventional techniques can give only very doubtful results, if any. The analysis of stresses around crack is most typical in this regard, because of the very high strain gradients that are involved. It would thus be particularly interesting to investigate possible applications of holographic interferometry to problems in fracture mechanics. This is the purpose of the present chapter.

Before fracture mechanics applications are investigated, a brief comparison between holographic interferometry and other techniques will be presented. Then, special questions in the stress analysis of crack will be reviewed. It will be seen which ones of these questions can or cannot be possibly answered by holographic interferometry. Among the results that can be obtained are the distribution of the out-of-plane surface displacements, and the minimum extent of the region where a plane stress analysis is not sufficient. The experimental results that were obtained for these problems will be presented.

B. Comparison of Holographic Interferometry with Other Techniques

Among the available methods of experimental stress analysis, strain gages and photoelasticity are the most commonly used. It is apparent at once that because of their physical size, strain gages are inadequate in regions of high strain gradient. Photoelasticity, on the other hand, is indeed much more interesting. Furthermore, its feature of producing fringe patterns, as in interferometry, invites a comparison of these two techniques. The comparison will be particularly aimed at the nature of the measurements that can be made, the materials requirements, and the sensitivity of both methods.

The nature of the measurements, first of all, is quite different. It has been seen that the basic output of reflection holographic interferometry is a surface displacement. Emphasis has been

placed on the out-of-plane component in the present work, however, in-plane components can be measured as well [9,10,11]. In transmission, holographic interferometry provides a means for measuring a linear combination of the average stresses through the thickness. This combination turns out to be the sum of the principal stresses when the conditions of generalized plane stress are satisfied. The use of the reflection and transmission techniques in combination allows one to determine the average values (through-the-thickness) of the normal stress (σ_z), and of the sum of the three principal stresses. Photoelasticity, on the other hand, gives basically the difference of the principal stresses and their directions. One of its great advantages is its ability to provide measurements within the thickness of a specimen, by the use of the "stress-freezing" technique, whereas holographic interferometry can provide only surface, or through-the-thickness average measurements. However, photoelasticity places a severe restriction on the mechanical properties of the material.

These restrictions on the materials for photoelastic tests are commanded by the requirement that the material must indeed have a proper stress-optical behavior. A model of the piece to be tested has thus to be made from a photoelastic material. This procedure can sometimes be a serious handicap, when the mechanical or geometric properties of the model cannot match those of the actual piece properly. A mechanical mismatch is especially likely when the Poisson's ratios of the piece and the model are different, which can

alter the stress distribution. This restriction is particularly drastic when the stress freezing technique is used, because the Poisson's ratio of photoelastic materials at their critical temperature is usually very close to 0.5. Mechanical problems arise also when local yielding occurs, in regions of high stress concentrations. Besides these mechanical problems, geometric difficulties can also be raised. Besides the uncertainties inherent to any modeling, some features of the actual piece can be difficult or impossible to reproduce. This is especially true when cracks are involved. It is very difficult to produce a sharp crack in most photoelastic materials, and relatively blunt notches have to be machined instead. Even more specific features of a crack, such as its tunneling, are practicably impossible to reproduce. Although some interesting results can indeed be obtained in fracture mechanics by photoelastic methods [28], these results remain subjected to the aforementioned restrictions.

A considerable advantage of holographic interferometry is that it is free of these restrictions, at least as far as the reflection technique is concerned. The tests can be performed directly on the pieces of interest, which removes all the problems arising from modeling. This feature is indeed of great interest when the crack behavior is expected to depend on features that cannot be reproduced on a model, such as the nature of the material or some details of the crack geometry. Holographic interferometry can then provide some information that could not be obtained from photoelasticity. Another advantage of holographic interferometry also comes from its sensitivity, which will now be compared to the sensitivity of photoelasticity.

The sensitivities of both techniques can be compared from two view points. The first one is the number of fringes that are obtained at a given stress level. The second one is the distribution of these fringes in the regions of interest, which is related to the ease of data processing in these regions. The sensitivity in terms of fringe numbers can be defined as the number of fringes per unit stress, for a unit thickness of the material. This quantity will thus be expressed in fringe -in/lb (fringe -m/N). The greater that number, the more fringes are produced. The sensitivity of photoelastic materials is typically of the order of magnitude of 0.01 fringe - in/lb (0.1 fringe - m/N). For holographic interferometry in transmission with PMMA, it was seen to be 0.034 fringe - in/lb (0.30 fringe - m/N). In reflection, it is close to 0.01 fringe - in/lb (0.1 fringe - m/N) for PMMA and of the order of 0.001 fringe - in/lb (0.01 fringe - m/N) for aluminum. These figures show that the sensitivities for the two techniques have the same order of magnitude for PMMA and photoelastic materials. The absolute sensitivity is lower in aluminum, but this lower value is compensated by the higher stress levels that are applied on metal specimens. Both techniques thus can be expected to perform about equally for the number of fringes that are produced. However, the distribution of the fringes is quite different from one method to the other. In first approximation, the holographic interferometry fringes, or isopachs, are lines of constant sum of the principal stresses. The photoelastic fringes, or isochromatics, are lines of constant difference of these stresses. This property of

the photoelastic fringes is rather unfortunate in the study of crack problems. A most interesting region to study in these problems is around the direction where the crack is most likely to propagate. But the principal stresses usually turn out to be almost equal in that direction. Since the fringe orders in photoelasticity are proportional to the difference of principal stresses, very few fringes are usually produced in the direction of crack propagation. In mode I type of loading [28] in particular, no fringes at all are produced on the line of expected crack extension. Just the opposite happens in holographic interferometry. In mode I loading, the directional gradient of the fringe order at a given distance away from the crack tip turns out to be maximum in the direction of expected crack propagation.

Summarizing the comparison of photoelasticity and holographic interferometry, it thus appears that those methods are complementary. Holography has the shortcoming of providing only thickness-averaged quantities, whereas stress-freezing photoelasticity has the ability to yield measurements inside the specimen. But this ability cannot be utilized without a severe restriction being imposed on the type of material to be used for modeling. The sensitivities of both techniques are of the same order of magnitude. But the fringe distribution is different in the two techniques: photoelasticity is better suited to measure shear stresses, whereas holography is most sensitive to tensile stresses. Together with the information expected from the experiment, these characteristics of both methods have to be taken into

account in the choice of the technique to be used. It appears, however, that holographic interferometry has the potential of providing some measurements in fracture mechanics that could not be made by other methods. Before examples of applications are given, however, it is suitable to review briefly some relevant parts of the background for the analytical study of crack problems.

C. Analytical Solutions of Crack Problems

The tests that were performed in the case of a plate with a circular hole provided a useful way to evaluate the validity and the accuracy of measurements made by holographic interferometry. The available results from two- and three-dimensional analyses gave a useful basis for comparison with experimental results. The situation is quite different in fracture mechanics problems, because of the lack of adequate analytical solutions. The solutions that are available are basically of three types, two-dimensional analyses, using either plane strain or generalized plane stress hypotheses, and some three-dimensional (plane stress) analyses. Unfortunately, it turns out that all of the aforementioned analyses fail to give a useful prediction of the quantity measured by reflection holographic interferometry; that is, basically a whole field measurement of the out-of-plane surface displacement. The reasons why the analytical methods fail to provide this quantity will be examined for each analysis separately.

The plane strain, two-dimensional analysis, first of all, is obviously not suitable for the present purpose. Its basic assumption is that the strain in the thickness direction is zero. If it would hold rigorously, this would in turn give a zero normal surface displacement over the whole field, and no fringes at all would be observed. The fringes that are actually observed reveal some departure from the plane strain condition. This departure may originate only in a thin surface layer close to the crack tip. But it probably also extends into the thickness of the specimen when the distance from the crack tip increases.

The stress and displacements analysis can also be made by using the hypotheses of generalized plane stress. This assumption is usually considered to be quite valid for thin specimens, at a sufficient distance from the crack tip. But it is unrealistic close to the crack tip, where the actual conditions are close to plane strain. The plane stress analysis thus cannot give a whole field solution. Furthermore, no theoretical criterion is available to determine the distance from the crack tip where the plane stress analysis can become acceptable. Finally, even with the generalized plane stress hypothesis, the analytical solution is still quite complicated and exact solutions are available only for very few geometric configurations.

Between the generalized plane stress region away from the crack tip, and the near-tip region of nearly plane strain, no two-dimensional analysis can be used. A three-dimensional approach would

then be necessary, but no analysis of this type has yet been made in this region. The only three-dimensional analyses available still assume the strain in the thickness direction to be zero [29], and are applicable only in the very near-tip region, as is the two-dimensional plane strain analysis. The difference between the analyses is that the stresses are assumed to be constant through the thickness in the two-dimensional plane strain analysis, whereas they are functions of the thickness coordinate in the three-dimensional analysis. In either case, however, the out-of-plane surface displacement would be expected to be zero, from the basic hypothese used in the analysis. Small displacements that could however be induced in a thin surface layer are physically expected, but not predicted quantitatively from the analysis.

From this brief overview of the analytical solutions of crack problems, it thus appears that the analyses, whether two- or three-dimensional, that assume a state of plane strain, cannot be used to predict out-of-plane surface displacements. They would necessarily predict a zero surface displacement, except for the unpredictable influence of a thin "boundary layer". Furthermore, these analyses are restricted to a very small near-tip region. The generalized plane stress solution, on the other hand, can be used throughout the far field for relatively thin plates. But generalized plane stress solutions are available only for a limited number of geometric configurations. Furthermore, these solutions fail to be valid when the crack tip is approached, and their range of validity is not defined.

A generalized plane stress solution is valid "far" from the crack tip, but one does not know how far. This information could be obtained by comparison to a complete three-dimensional analysis. But no complete solution is available that would give the three-dimensional stress distribution at any distance from the crack tip. The holographic interferometry technique seems quite suitable to obtain some experimental informations about this problem, that could be used in further developments of analytical solution. An example of the type of results that can be obtained will be presented in the next section.

D. Experimental Results

The fracture mechanics application that was made involved a single-edge cracked aluminum sample. Two sets of informations were to be obtained from this specimen. The first goal was to determine the out-of-plane surface displacement along the expected line for crack extension. The second one was to estimate the distance from the crack tip where the generalized plane stress analysis becomes valid. For this second step, a transparent PMMA model of the aluminum sample had to be made and tested. The procedures and results of the reflection test will be presented first. These results provide the surface displacements. The results of the transmission test will be presented next and will be compared to those from the reflection test. According to the procedure described in chapter VII.C, the results from the two tests will be used to estimate the extent of the

three-dimensional effect from the crack tip along the line of crack extension.

1. The Reflection Test

The geometry of the specimen used for the reflection test is represented in figure 35. The material is a 7075-T6 aluminum alloy, the mechanical properties of which are reported in table 1. Interferograms were made at several different loads, and the results were again normalized with respect to the fringe order at infinity. The expression for this fringe order is the same as for the circular hole problem, equation IV-21:

$$N_\infty = \frac{\nu P}{2b \lambda E}$$

where P is the applied load variation, and b is the half-width of the specimen. From the data of table 1 and of figure 35:

$$\frac{N_\infty}{P} = 0.823 \times 10^{-3} \text{ fringe/lb.} = 0.185 \times 10^{-3} \text{ fringe/N.}$$

The normalized fringe order in reflection is thus:

$$\left(\frac{N}{N_\infty}\right)_r = \frac{N}{P \times 0.823 \times 10^{-3}} = \frac{N}{P} \times 1214$$

Interferograms were recorded for various values of the load P. An example of these interferograms is given in figure 36. For every value of P, the fringe order was normalized according to equation VIII-2, and plotted versus the distance to the crack tip (figure 37). The distance r was normalized with respect to the crack length a. Most of the corrections introduced for the circular hole were not

necessary in the crack problem, because the region of interest is very small and close to the optical axis. The terms η_r and η_t given in equations IV-10 and IV-11 are thus negligibly small. The only correction that was made was for the uniform shift η_c of the fringes. The fringe order is known again only within an unknown additive constant. The sets of data points obtained for each load were thus shifted vertically in figure 37, so that all these sets might fit a single smooth curve as well as possible. Figure 37 thus gives the profile of the out-of-plane surface displacement along the crack line extension. The absolute displacement is given only within an unknown additive constant. This displacement is normalized with respect to its value "at infinity", that would be induced by the applied stress at infinity in conditions of generalized plane stress.

2. The Transmission Test

The geometry of the PMMA model used for the transmission test is represented in figure 35. The crack length-to-width ratio was chosen to be the same as that of the aluminum sample, but the thickness-to-width ratio is smaller for the PMMA model ($h/2b = 0.10$ versus $h/2b = 0.17$) than for the aluminum specimen. The PMMA that was used is the same as that for the circular hole. Its mechanical properties are given in table 1. One interferogram was made which is shown in figure 38. The fringe order was normalized with respect to its value at infinity given by equation V-9:

$$N_\infty = F h \sigma_\infty \qquad \text{(VIII-3)}$$

where

$$\sigma_\infty = \frac{P}{2b\,h}$$

Equation VIII-3, thus gives:

$$N_\infty = \frac{FP}{2b}$$

Numerically, $F = -0.034$

$2b = 1.00$

Therefore,

$$\frac{N_\infty}{P} = -0.034 \quad \text{fringe/lb.}$$

The interferogram was made with a load variation P = -22 lbs, which gives N_∞ = 0.748 fringe. The resulting normalized fringe orders are plotted in figure 39, versus the normalized distance r/a. This graph can now be used for comparison to the results of the reflection test, given in figure 37.

3. Comparison of Reflection and Transmission Results

The normalized fringe orders on figures 37 and 39 can now be compared, according to the procedure described in chapter VII.C.3. Following that procedure, the normalized reflection and transmission fringe orders whould be equal in the remote field and are expected to deviate from one another close to the crack tip. In the comparison of the two fringe orders, however, it must be remembered that both of them are known within an additive constant. The two curves can thus be legitimately shifted with respect to one another. If the

argument about the equality of the fringe orders away from the crack tip is correct and assuming that the behavior of the material is lineraly elastic, then both curves should fit closely for a certain amount of vertical shift. It is seen that this actually happens, as shown in figure 40, where the experimental point of figure 37 and the smooth curve of figure 39 are shown simultaneously. As expected also, it is seen that the fringe orders depart considerably from one another close to the crack tip. It is noteworthy that whereas a proper fit can be obtained in the far field, it would not be possible to determine any vertical shift of the curves that would make them overlap in the near field. The point where the reflection fringe order departs from the transmission one is seen to be located at about ten percent of the crack length. It can thus be estimated that within that distance from the crack length, the normal stress σ_z assumes a significant value compared to the other stresses. Beyond ten percent of the crack length, this stress, or at least its average value through the thickness, becomes practically negligible. It is not known for sure that the condition of generalized plane stress are satisfied beyond this distance. But it can be concluded that these conditions are certainly not satisfied at distances closer than ten percent of the crack length.

It should be noted, however, that the aforementioned results were obtained for relatively low loads. The experimental results of figure 37 were obtained at loads ranging from twenty to thirty percent of the expected failure load. At such low loads, the overall response

of the specimen (load versus displacement between grips) can be considered to be lineraly elastic. When the failure load is approached, however, the load versus displacement curve may become non-linear for some materials. When such a non-linearity occurs, its characteristics depend on the material that is used. Then the experimental curves obtained with various materials might be quite different in the region close to the crack tip.

CHAPTER IX. CONCLUSIONS AND SUGGESTIONS FOR FURTHER RESEARCH

A. Conclusions

The possibility of using holographic interferometry for stress analysis has been known and developed for a number of years. The technique was soon recognized to have the theoretical possibility for measuring a number of quantities. For the analysis of plates with in-plane loading, these quantities are the three components of surface displacements for reflecting specimens and a compound quantity involving the change in thickness and the average z-stress for transparent specimens. The transmission technique was developed first, because it is the easier one to work out experimentally. The theoretical possibility of measuring in-plane displacement components on reflecting specimens was demonstrated next, starting with very thin or soft samples, in order to alleviate problems from rigid body displacements [9]. The range of applicability of the technique was then extended to thicker and stiffer specimens. The use of multiple hologram techniques and computer data processing allowed one to average out the unwanted rigid body displacement components. Although good results could be obtained by this method for the in-plane displacement components, a considerable amount of data processing was involved and satisfactory results could not be obtained for the out-of-plane displacement component. The fringe compensation technique developed in the present work makes it possible to measure this out-of-plane displacement, thus making one of the earliest recognized potentialities of the technique practicable.

Experimental measurements of the normal surface displacement being made possible, a further investigation was made to get as much information as possible from this quantity, by relating it to other available data. An interesting result of this investigation was the demonstration of the possibility to evaluate the average z-stress through the thickness of specimens close to stress concentrations in plates. This average z-stress can be evaluated explicitly for transparent samples. In the case of metallic samples, it is possible at least to detect the existence of such z-stresses, thereby locating regions where the generalized plane stress conditions fail to be valid.

The aforementioned techniques were applied to the experimental analysis of stresses around a circular hole in a plate in uniaxial tension. The experimental results were compared to those of the generalized plane stress analysis and to the three-dimensional analysis made by Alblas. These two analyses give identical results in the far-field region ($r/a > 2$). But they are significantly different close to the hole boundary. In the tests that were made, three quantities were evaluated experimentally. The out-of-plane surface displacement was obtained from a reflection test. A linear combination of the stresses was evaluated by a transmission test. Finally, the average z-stress was evaluated by comparing the results of the reflection and transmission tests. These three measurements were found to be in good agreement with both theories in the far-field region (where the theories agree). In the near-field region, the

experimental results departed consistently from the generalized plane stress analysis; but they were always in good agreement with the three-dimensional analysis. The small amount of discrepancy that was observed can be attributed to experimental errors. The three-dimensional analysis is thus quite satisfactory to account for the experimental results. The two-dimensional analysis, on the other hand, though satisfactory in the far-field region, clearly fails to be consistent with the measured stresses and displacements close to the hole.

Possible applications of similar techniques to some problems in fracture mechanics were finally examined. Holographic interferometry appears to be a particularly suitable tool in this field. Its high resolution is interesting in regions of stress concentration. Furthermore, it can give results with specimen made from any material. As an example of application, the surface displacement was measured along the line of crack extension in an aluminum single-edge cracked specimen. The result of this reflection test was compared to a transmission test performed with a thin PMMA model of the aluminum specimen. Comparison of these results provided an estimate of the minimum extent of the region where a three-dimensional analysis would be required to account for the observed results close to the crack tip.

B. Suggestions for Further Research

The results that were obtained in this work suggest a number of other possible investigations of interest in three different

directions: (1) further improvements of holographic interferometry, (2) development of more refined stress analysis techniques, and (3) application of the technique already developed in its present form to new problems. As far as the holographic technique is concerned, the fringe compensation technique might possibly be used in the determination of in-plane components of the displacements also. Although some other methods are already available for this purpose, a fringe compensation procedure would probably reduce considerably the amount of data processing that is presently required.

When it comes to applications of these methods to stress analysis of plates, various further improvements are also expected to be possible. A combination of the technique in its present state with photoelasticity would seem to be of particular interest. Reflection and transmission holography were shown to provide two independent equations for the average value of the normal stresses. Two-dimensional photoelasticity is known to give a third equation relating the in-plane stresses. Transmission holography has already been used extensively as a method of "separation of the stresses" in connection with photoelasticity. In a plane stress analysis, transmission holography gives the sum of the principal stresses, and photoelasticity gives their difference, thus making it possible to know both principal stresses separately. The introduction of a third equation from reflection holography should not only give the average third normal stress in the z-direction, but also make it possible to determine the average x- and y-stresses, taking into account the departure from generalized plane stress.

Without any further improvement, the technique in its present form could be applied to a great variety of other problem, especially in fracture mechanics. The problem of three-dimensional distribution of stresses associated with cracks is still under investigation and no completely satisfactory solution is known. An experimental investigation of the effect of the plate thickness on the average z-stress distribution would be of great interest for the further development of analytical solutions. The techniques that were developed in this work would probably be very well suited for the solution of this problem. The few results that are presented in relation to fracture mechanics problems suggest that the holographic interferometry technique has interesting potential applications in this area.

Table 1. Optical and Mechanical Properties of the Materials Used in the Investigation

Object	Nature of the Constant	Symbol	English Units		S.I. Units		Origin of Figures
			Nominal	Tolerance	Nominal	Tolerance	
Laser Light	light wavelength	λ	2.491×10^{-5} in		0.6328 μm		Manufacturer
PMMA	Poisson's Ratio	ν	0.33	± 0.02	0.33	± 0.02	Strain Gage Test
	Elastic Modulus	E	3.3×10^{5} psi	$\pm 0.2 \times 10^{5}$	2.28×10^{3} MPa	$\pm 0.15 \times 10^{3}$	
	Index of Refraction	n_o	1.50	± 0.02	1.50	± 0.02	Manufacturer
	Transmission Fringe Constant	F	0.034 fringe - in/lb	± 0.003	0.30 fringe - m/N	± 0.03	Calibration Test
Aluminum	Poisson's Ratio	ν	0.32	± 0.02	0.32	± 0.02	Ref* & Strain Gage Test
	Elastic Modulus	E	10.4×10^{6} psi	$\pm 0.5 \times 10^{6}$	72×10^{3} MPa	$\pm 4 \times 10^{3}$	Ref*

* Aluminum Standards and Data 1972-73

Table 2. Correction Factors for Radial Displacement Along the x- and y-Axes, for the Circular Hole in Reflection

$\frac{r}{a}$	$\theta = 0, \pi$ (x-axis)		$\theta = \frac{\pi}{2}, \frac{3\pi}{2}$ (y-axis)	
	$rf_h(r)$	$(\frac{\eta_r}{N_\infty})_h$	$rf_v(r)$	$(\frac{\eta_r}{N_\infty})_v$
1.0	-2.000	0.018	6.000	-0.053
1.1	-2.369	0.021	6.651	-0.059
1.2	-2.697	0.024	7.286	-0.064
1.3	-2.998	0.027	7.923	-0.070
1.4	-3.312	0.029	8.571	-0.076
1.5	-3.564	0.032	9.239	-0.082
1.6	-3.840	0.034	9.930	-0.088
1.7	-4.117	0.036	10.65	-0.094
1.8	-4.398	0.039	11.40	-0.101
1.9	-4.684	0.041	12.18	-0.108
2.0	-4.978	0.044	13.00	-0.115
2.2	-5.590	0.049	14.73	-0.130
2.4	-6.241	0.055	16.62	-0.147
2.6	-6.935	0.061	18.65	-0.165
2.8	-7.675	0.068	20.84	-0.184
3.0	-8.462	0.075	23.18	-0.205

Table 3. Correction Factors for Radial Displacements Around the Quarter-Circle $r = a\sqrt{2}$, for the Circular Hole in Reflection

θ	$rf_c(\theta)$	$(\frac{\eta_r}{N_\infty})_{a\sqrt{2}}$
0	-3.330	0.029
10	-2.968	0.026
20	-1.926	0.017
30	-0.330	0.003
40	1.628	-0.014
50	3.712	-0.033
60	5.670	-0.050
70	7.266	-0.064
80	8.308	-0.074
90	8.670	-0.077

Table 4-a. Results for the Circular Hole in Reflection, along the x-Axis

$N^{(o)}$	$x > 0$; $\theta = 0$							$x < 0$; $\theta = \pi$						
	$\frac{r}{a}$	η_t	$N^{(1)}$	$\frac{N^{(1)}}{N_\infty}$	$\frac{\eta_r}{N_\infty}$	$\frac{N^{(2)}}{N_\infty}$	$(\frac{N}{N_\infty})_r$	$\frac{r}{a}$	η_t	$N^{(1)}$	$\frac{N^{(1)}}{N_\infty}$	$\frac{\eta_r}{N_\infty}$	$\frac{N^{(2)}}{N_\infty}$	$(\frac{N}{N_\infty})_r$
5.0	1.03	-0.032	4.968	1.419	0.019	1.438	1.333	1.01	0.031	5.031	1.437	0.018	1.455	1.350
4.5	1.13	-0.035	4.465	1.276	0.022	1.298	1.193	1.11	0.034	4.534	1.296	0.021	1.317	1.212
4.0	1.25	-0.039	3.961	1.132	0.025	1.157	1.052	1.23	0.038	4.038	1.154	0.025	1.179	1.074
3.5	1.41	-0.044	3.456	0.988	0.029	1.017	0.912	1.36	0.042	3.542	1.012	0.028	1.040	0.935
3.0	1.58	-0.049	2.951	0.843	0.034	0.877	0.772	1.52	0.047	3.047	0.871	0.032	0.903	0.798
2.5	1.78	-0.055	2.445	0.699	0.038	0.737	0.632	1.7	0.053	2.553	0.729	0.036	0.765	0.660
2.0	2.02	-0.062	1.938	0.554	0.044	0.598	0.493	1.93	0.060	2.060	0.589	0.042	0.631	0.526
1.5	2.37	-0.073	1.427	0.408	0.053	0.461	0.356	2.28	0.071	1.571	0.449	0.052	0.501	0.396
1.0	3.00	-0.093	0.907	0.259	0.075	0.334	0.229	2.77	0.086	1.086	0.310	0.066	0.376	0.271

Table 4-b. Results for the Circular Hole in Reflection, along the y-Axis

$N^{(o)}$	$y > 0$; $\theta = \pi/2$							$y < 0$; $\theta = 3\pi/2$						
	$\frac{r}{a}$	η_t	$-N^{(1)}$	$-\frac{N^{(1)}}{N_\infty}$	$-\frac{\eta_r}{N_\infty}$	$-\frac{N^{(2)}}{N_\infty}$	$-(\frac{N}{N_\infty})_r$	$\frac{r}{a}$	η_t	$-N^{(1)}$	$-\frac{N^{(1)}}{N_\infty}$	$-\frac{\eta_r}{N_\infty}$	$-\frac{N^{(2)}}{N_\infty}$	$-(\frac{N}{N_\infty})_r$
4.0	1.06	0.048	3.952	1.129	0.056	1.185	1.290	1.04	-0.047	4.047	1.156	0.056	1.212	1.317
3.5	1.18	0.053	3.447	0.985	0.063	1.048	1.153	1.15	-0.052	3.552	1.015	0.061	1.076	1.191
3.0	1.32	0.059	2.941	0.840	0.071	0.911	1.026	1.27	-0.057	3.057	0.873	0.068	0.941	1.046
2.5	1.48	0.067	2.433	0.695	0.081	0.776	0.881	1.42	-0.064	2.564	0.733	0.077	0.810	0.915
2.0	1.65	0.074	1.926	0.550	0.091	0.639	0.744	1.60	-0.072	2.072	0.592	0.088	0.680	0.785
1.5	1.95	0.088	1.412	0.404	0.111	0.515	0.620	1.86	-0.084	1.584	0.452	0.105	0.557	0.662
1.0	2.30	0.104	0.897	0.256	0.137	0.393	0.498	2.21	-0.099	1.099	0.314	0.131	0.445	0.550
0.5	2.86	0.129	0.371	0.106	0.190	0.296	0.401	2.67	-0.120	0.620	0.177	0.172	0.349	0.454

Table 5. Results Around the Quarter-Circle $r = a\sqrt{2}$, for the Circular Hole in Reflection

$N^{(o)}$	θ (degrees)	η_t	$N^{(1)}$	$\frac{N^{(1)}}{N_\infty}$	$\frac{\eta_r}{N_\infty}$	$-\frac{\eta_c}{N_\infty}$	$(\frac{N}{N_\infty})_r$
3.0	13	0.028	3.028	0.865	0.023	-0.105	0.783
2.5	21	0.018	2.518	0.719	0.015	-0.105	0.629
2.0	28	0.009	2.009	0.574	0.006	-0.105	0.475
1.5	34	0.001	1.501	0.429	-0.005	-0.105	0.320
1.0	39	-0.006	0.994	0.284	-0.013	-0.105	0.166
0.5	44	-0.013	0.487	0.139	-0.022	-0.105	0.011
0.0	49	-0.019	-0.019	-0.006	-0.031	-0.105	-0.142
-0.5	54	-0.026	-0.526	-0.150	-0.041	-0.105	-0.296
-1.0	59	-0.029	-1.029	-0.294	-0.048	-0.105	-0.447
-1.5	65	-0.035	-1.535	-0.439	-0.057	-0.105	-0.601
-2.0	72	-0.047	-2.047	-0.585	-0.066	-0.105	-0.756
-2.5	81	-0.059	-2.559	-0.731	-0.074	-0.105	-0.910

Table 6. Results along the Axes for the Circular Hole in Transmission, Using the Calibration Test ($N_\infty = 5.95$) and the Self-Calibration ($N_\infty = 5.92$)

$\frac{r}{a}$	$\lvert N \rvert$ average	$(N/N_\infty)_t$	
		$N_\infty = 5.95$	$N_\infty = 5.92$
1.01	10.20	1.714	1.723
1.03	9.80	1.647	1.655
1.04	9.66	1.624	
1.06	9.47	1.592	
1.11	8.64	1.452	1.460
1.13	8.41	1.413	1.421
1.15	8.10	1.361	
1.18	7.78	1.308	
1.23	7.18	1.207	1.213
1.25	6.88	1.156	1.162
1.27	6.65	1.118	
1.32	6.22	1.045	
1.36	5.93	0.997	1.002
1.41	5.55	0.933	0.938
1.52	4.84	0.813	0.818
1.58	4.53	0.761	0.765
1.70	3.96	0.666	0.669
1.78	3.62	0.608	0.612
1.93	3.06	0.514	0.517
2.02	2.90	0.487	0.490
2.28	2.29	0.385	0.387
2.37	2.15	0.361	0.263
2.77	1.56	0.262	0.264
3.00	1.31	0.220	0.221

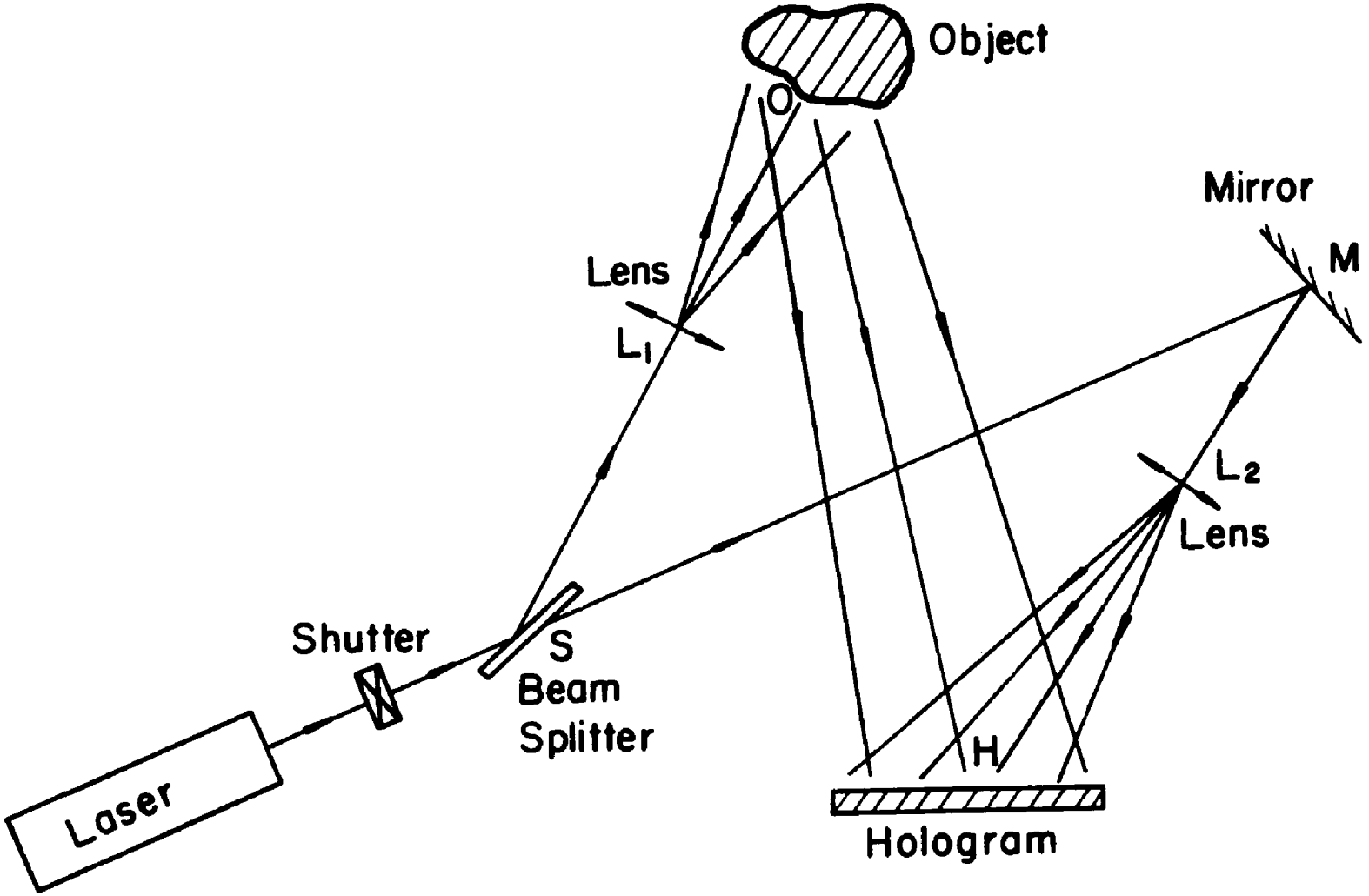

Figure 1. Basic Setting for a Reflection Hologram

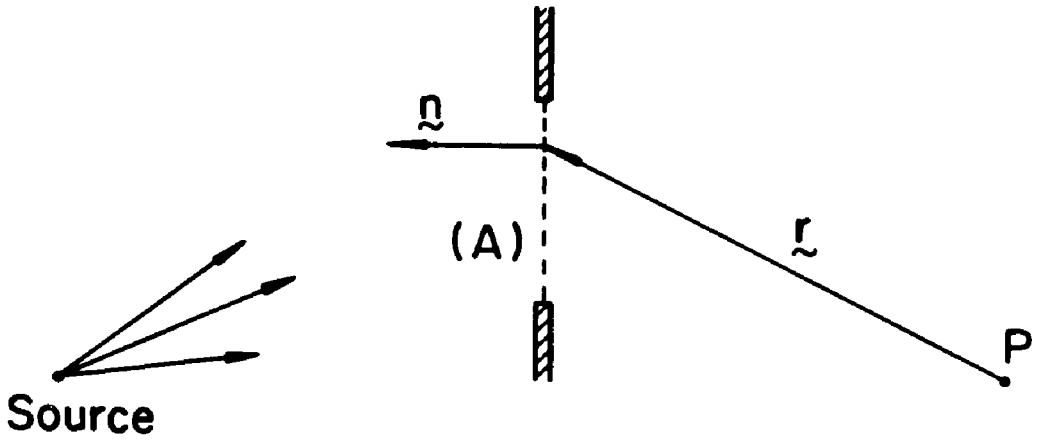

Figure 2. Diffraction of Light from a Source S to a Point P, Through an Aperture (A)

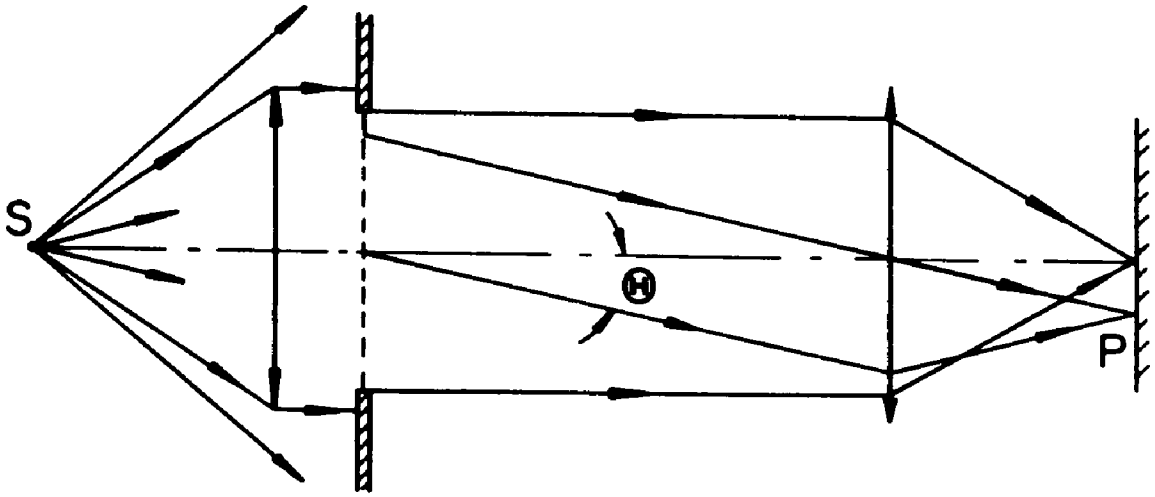

Figure 3. Diffraction of a Collimated Beam Through a Circular Aperture

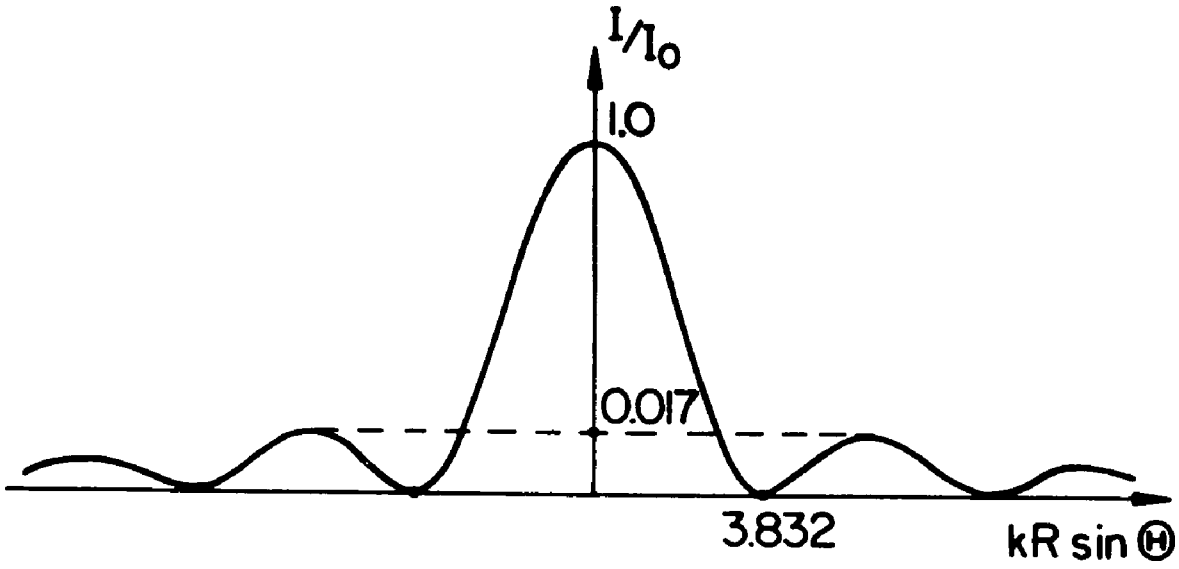

Figure 4. Distribution of the Intensity of Light Diffracted Through a Circular Aperture

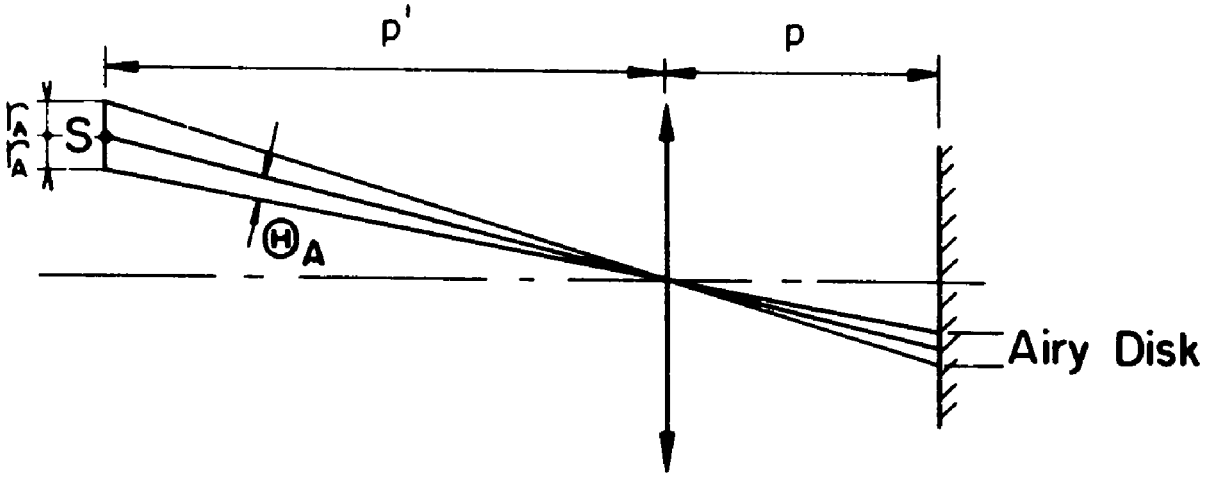

Figure 5. Relation Between the Airy Disk and the Apparent Angular Radius of the Source

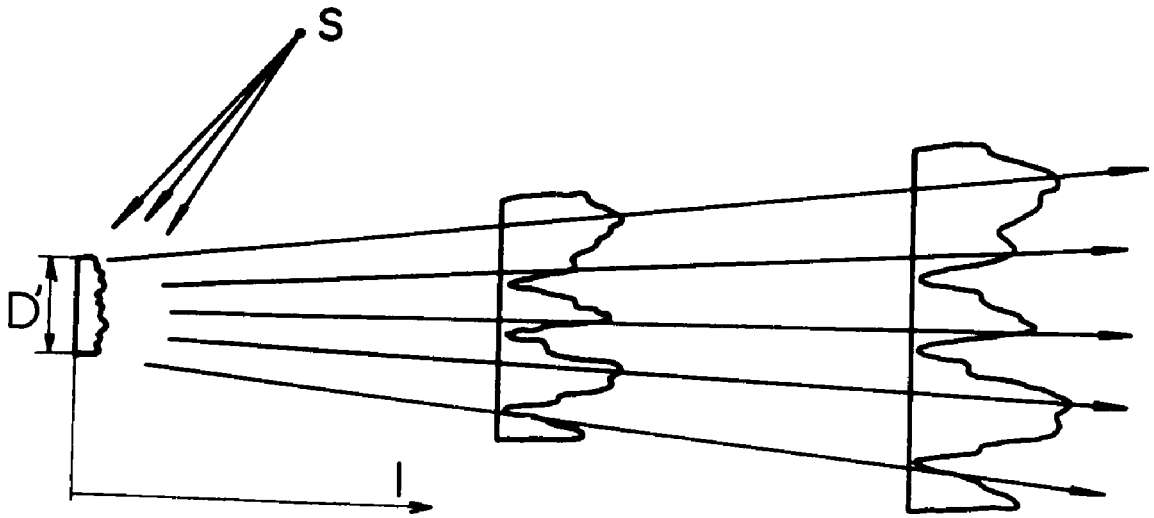

Figure 6. Phase Distribution of the Light Reflected by a Diffusing Object

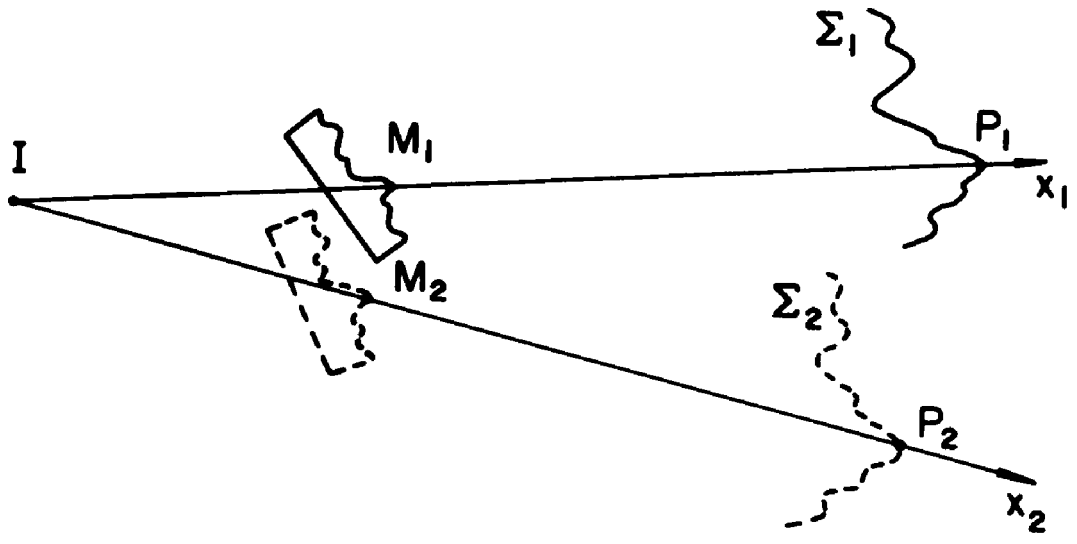

Figure 7. Homologous Rays and Fringe Localization

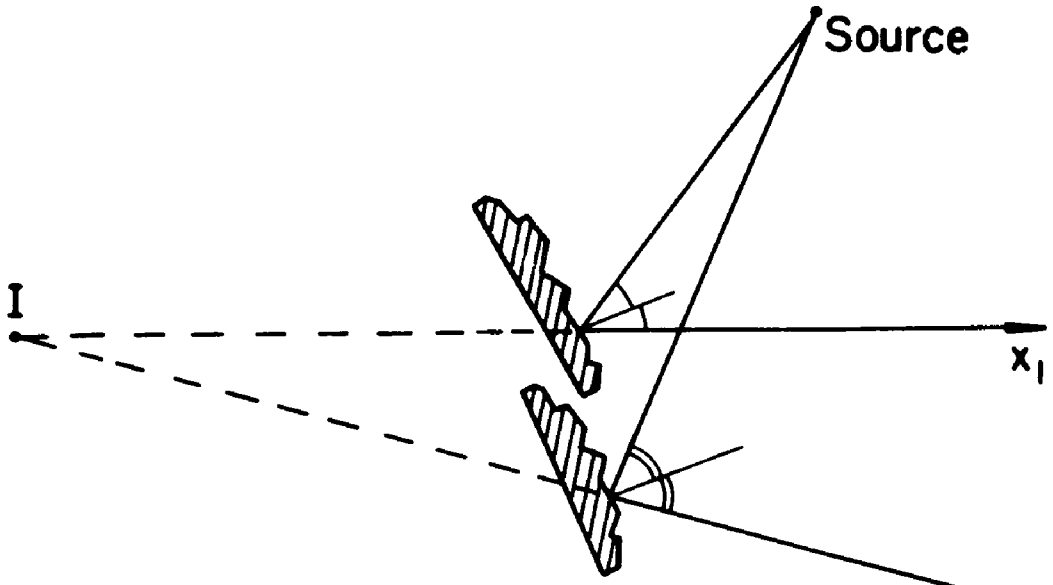

Figure 8. Geometric Construction of Homologous Rays

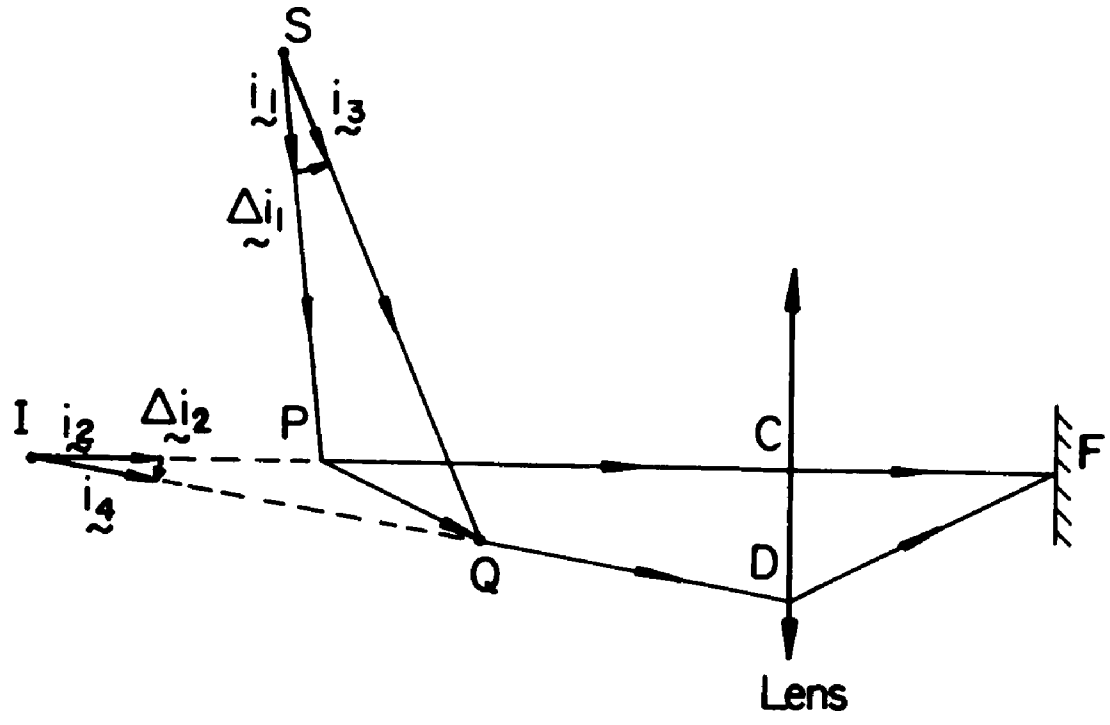

Figure 9. Determination of the Path Difference in the Fringe Formation

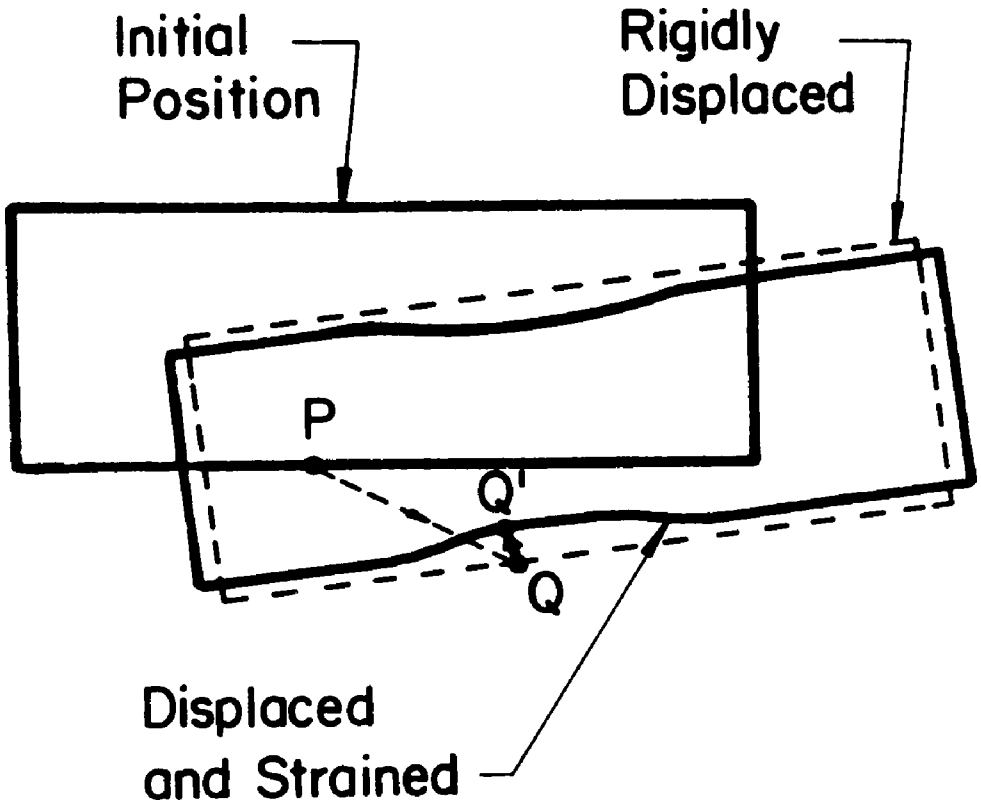

Figure 10. Two Steps from the Initial State to the Final State: Rigid Body Displacement, Followed by Straining

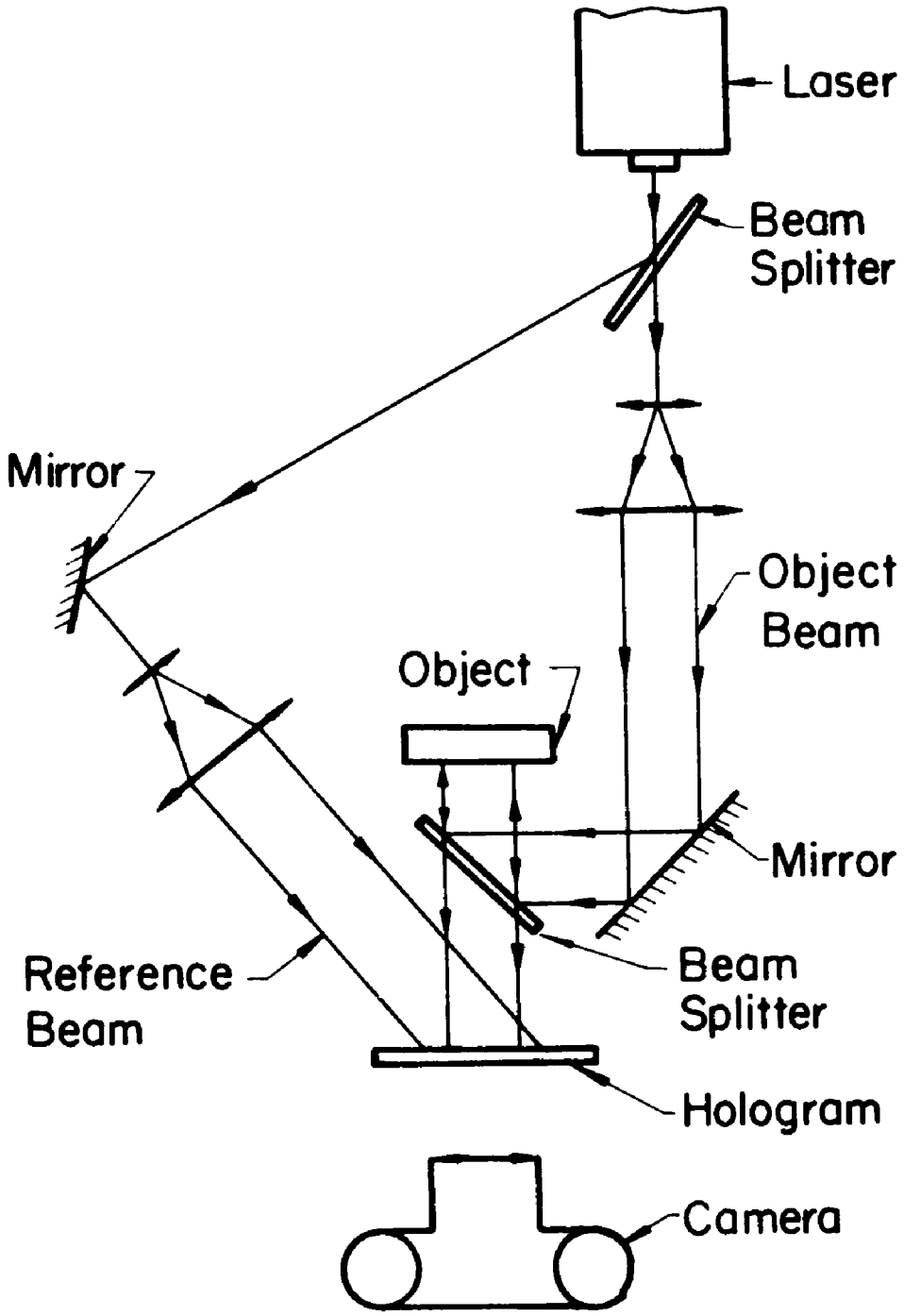

Figure 11. Sketch of the Complete Interferometer

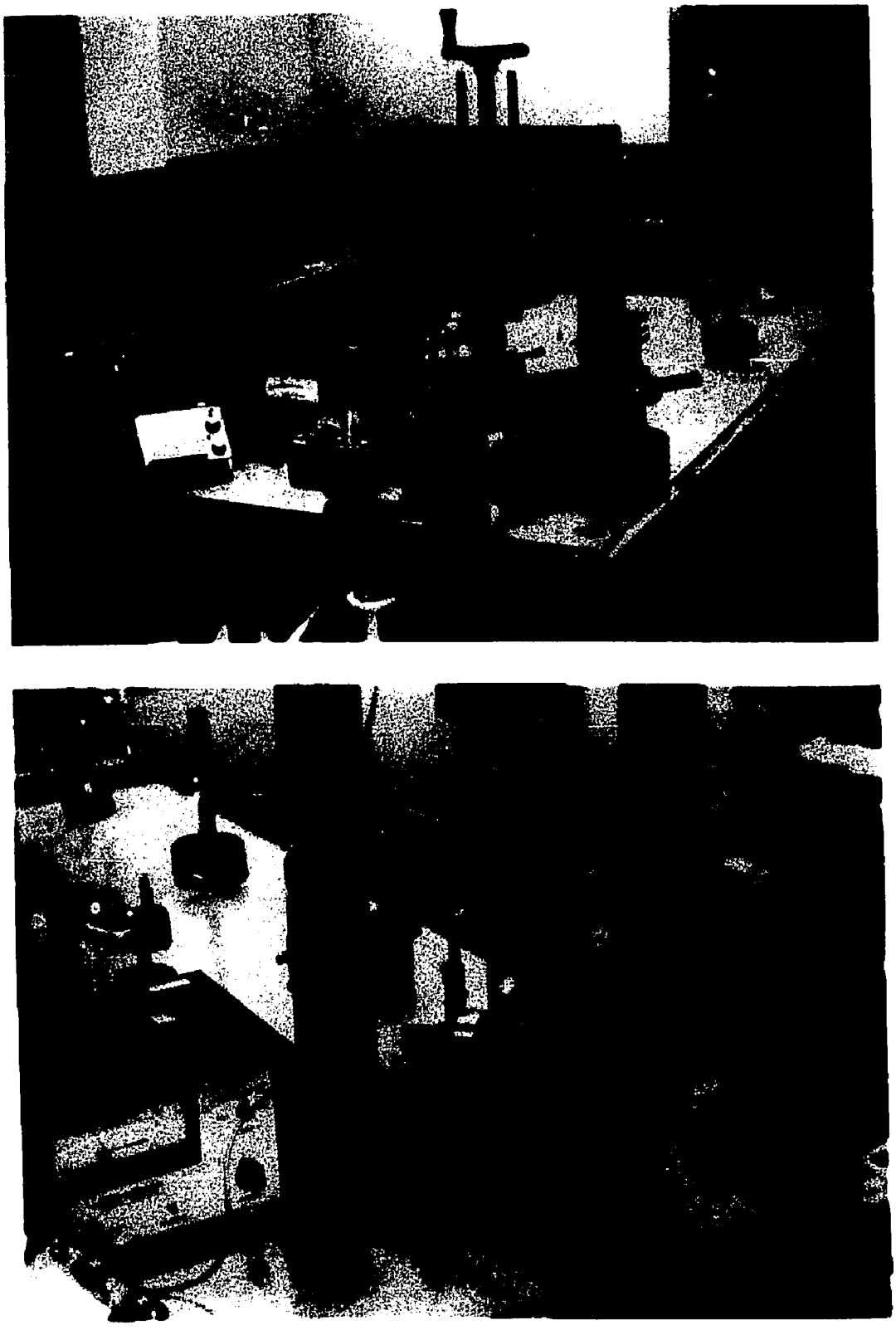

Figure 12. Photograph of the Set-Up for Reflection Holographic Interferometry

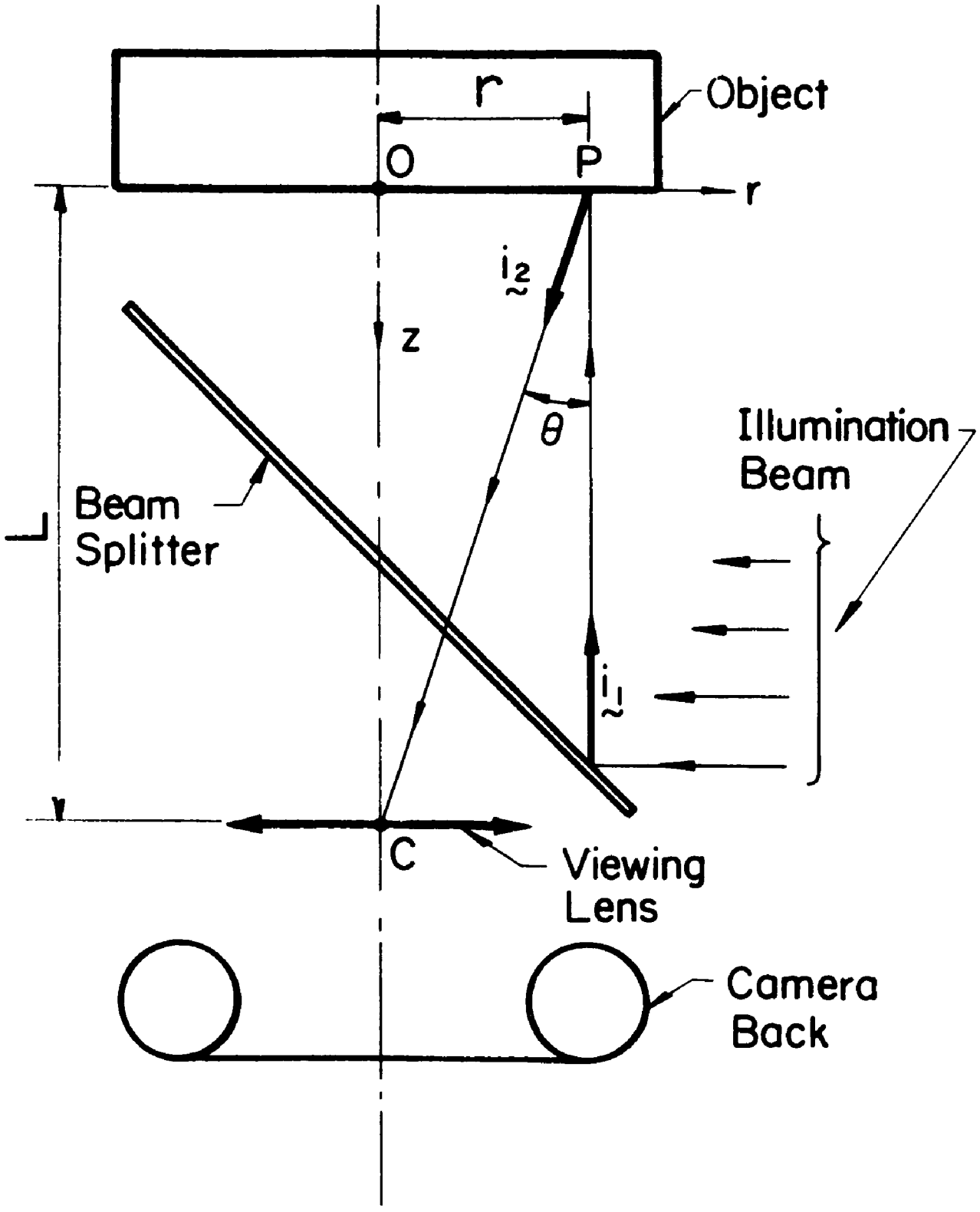

Figure 13. Initial Geometry of the System

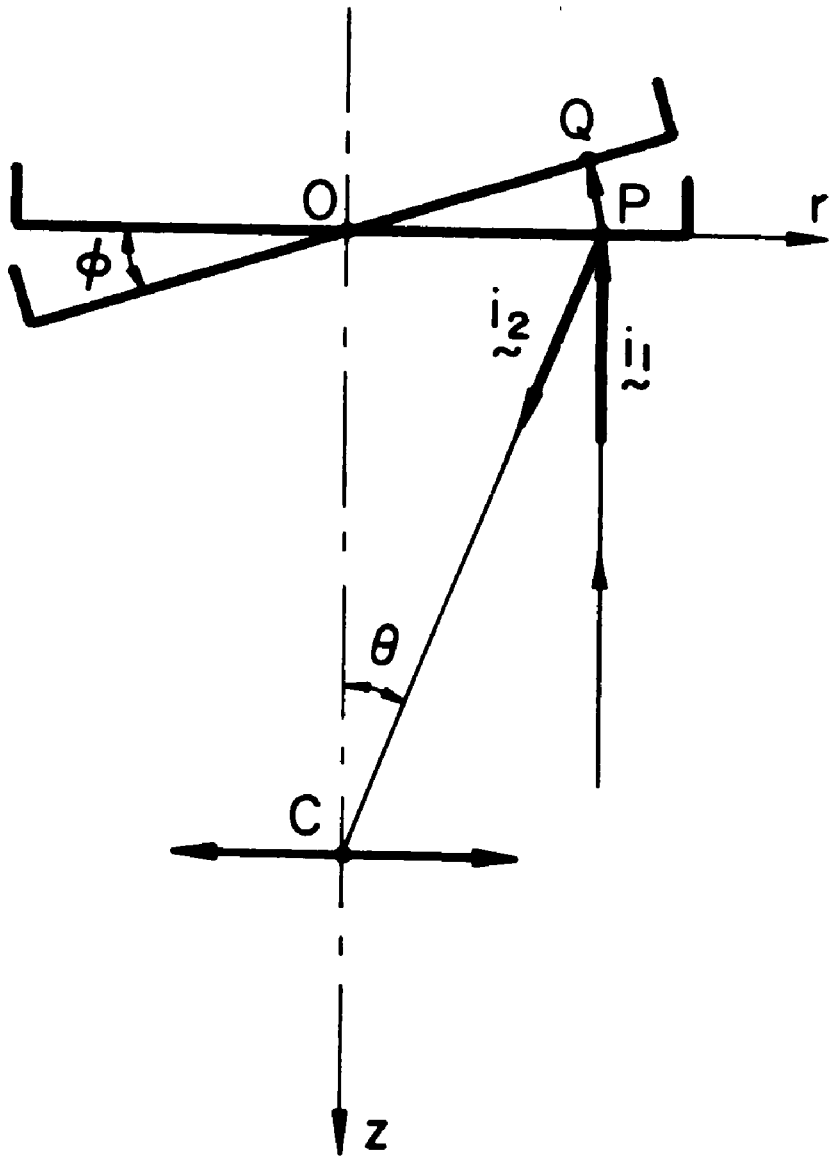

Figure 14. Rotation of the Object Without Straining

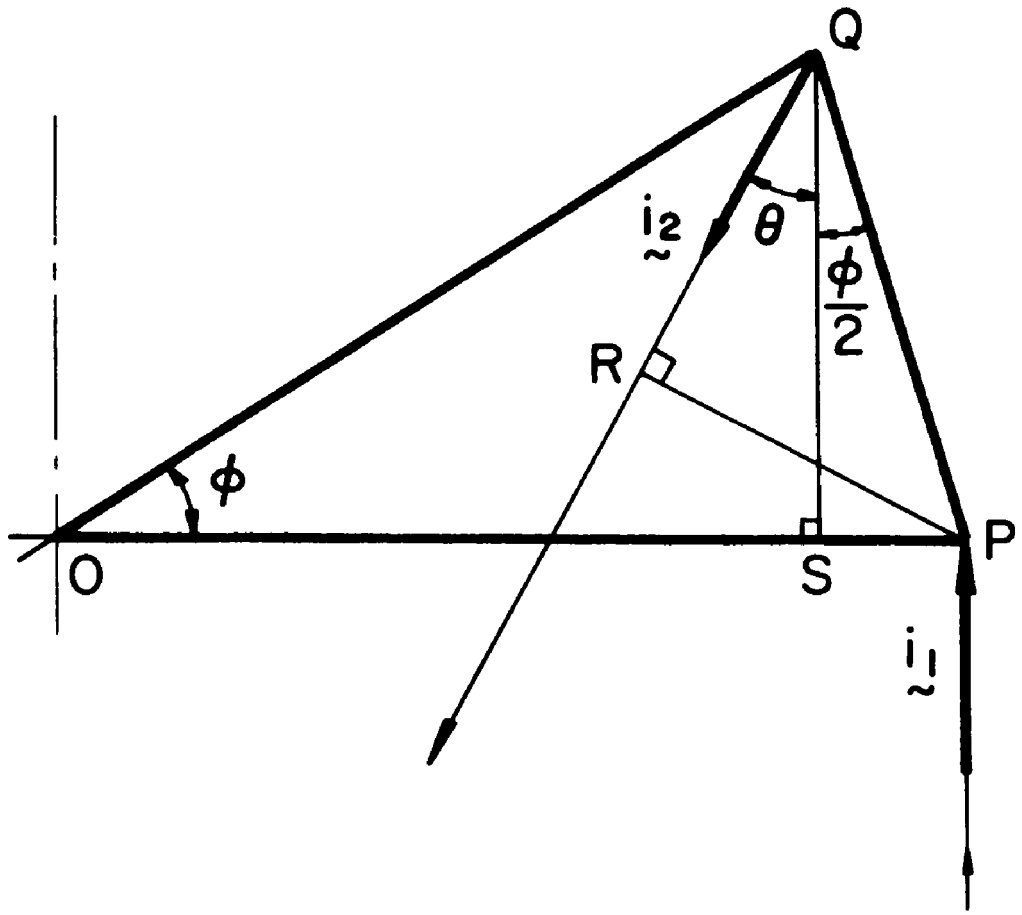

Figure 15. Path Difference for Rotation Without Straining

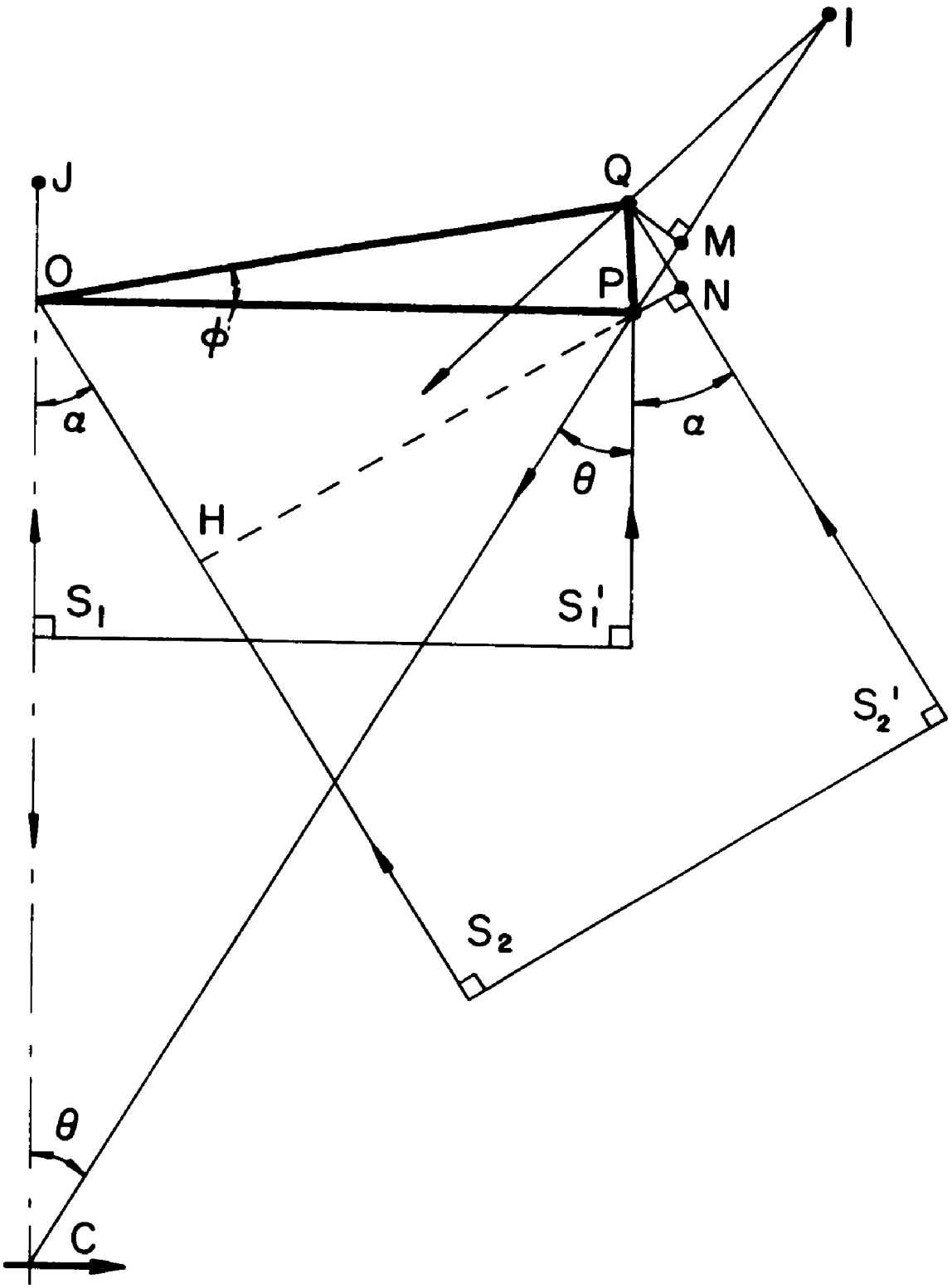

Figure 16. Modified Geometry of the System after Compensation for Rigid-Body Rotation

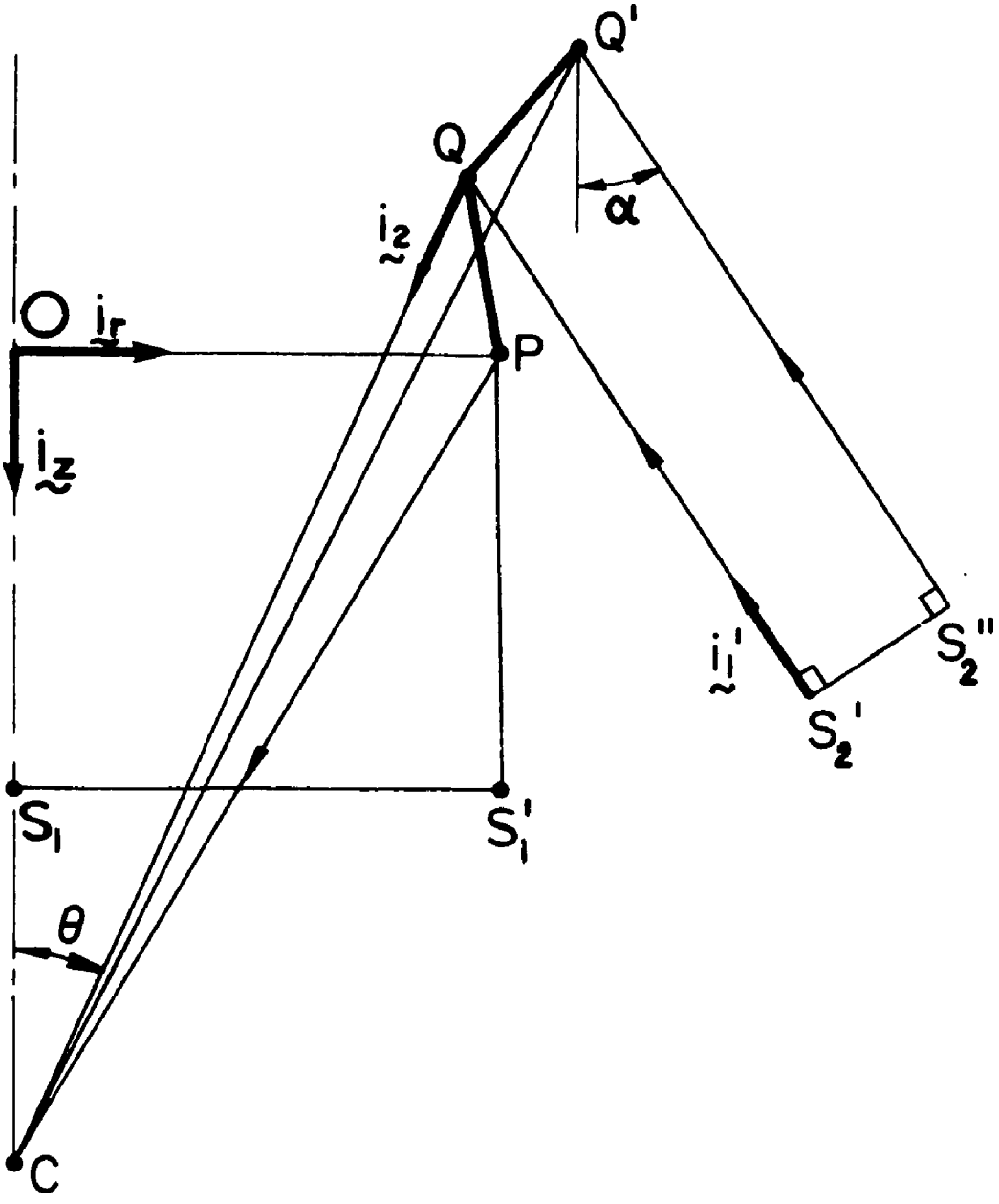

Figure 17. Modified Geometry for Combined Strain and Displacement

Figure 18a. Reflection Holographic Interferogram Around a Circular Hole in a Plate under Tension (Loading Axis is Indicated by the Arrow); Magnification X5.6.

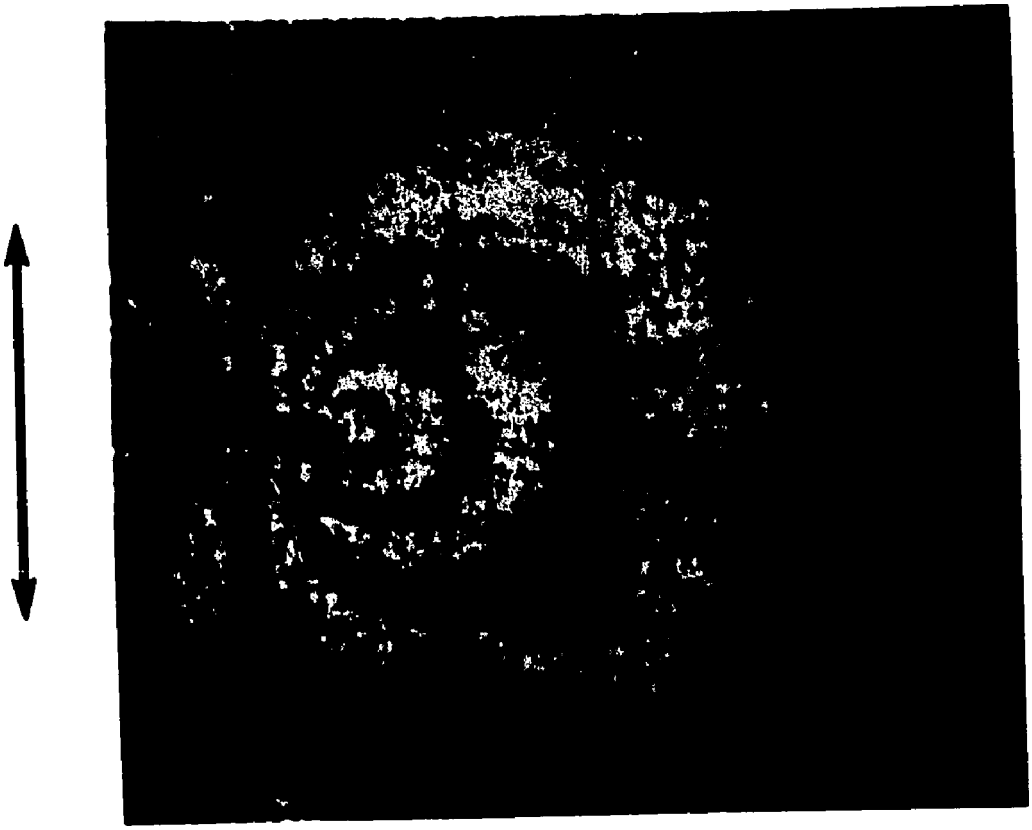

Figure 18.b Reflection Holographic Interferogram Close to the Tip of a Notch in a Plate under Tension (Loading Axis is Indicated by the Arrow); Magnification X6.75.

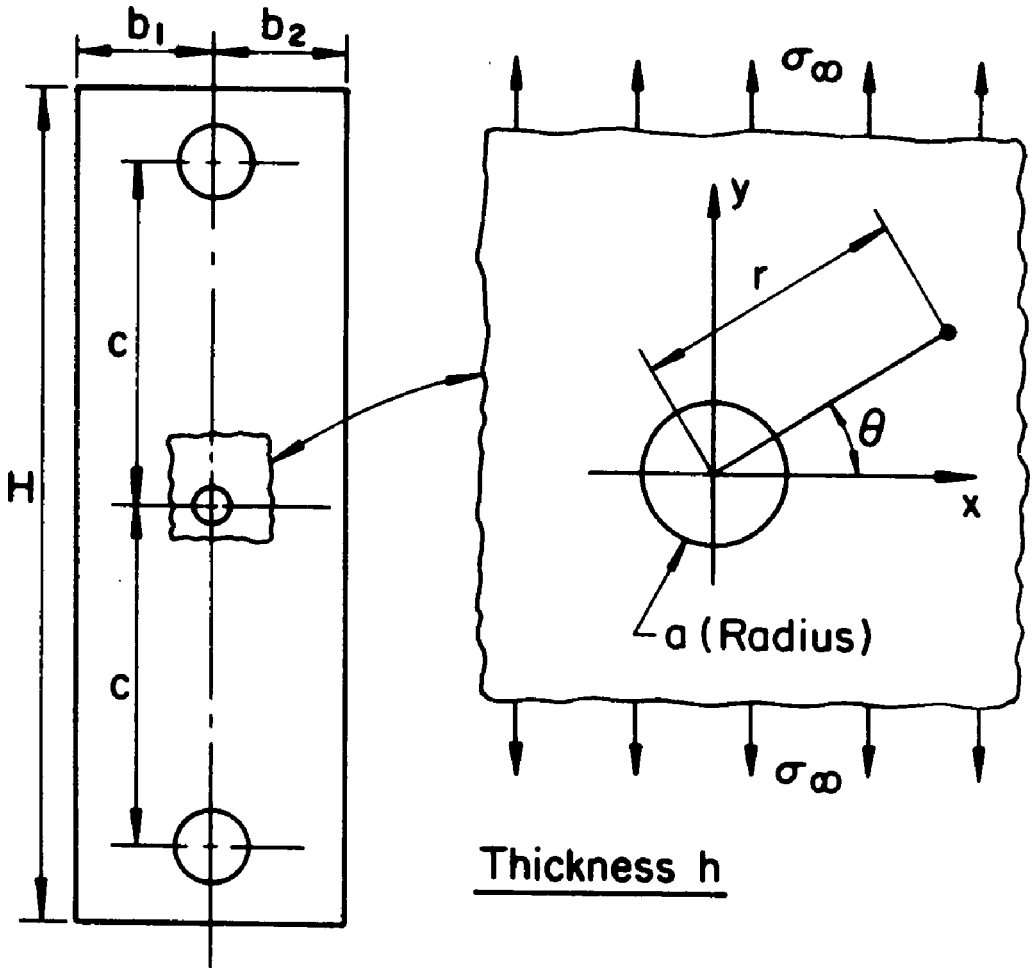

TABLE OF DIMENSIONS				
	Dimensions, in.		Dimensions, mm	
	Nominal	Tolerance	Nominal	Tolerance
a	0.125	0.002	3.18	0.05
b_1, b_2	1.000	0.005	25.4	0.13
c	2.38	0.01	60.3	0.25
h	0.25	0.01	6.37	0.25
H	6.00		152.4	
$b_1 = b_2 \pm 0.001$ in.			(±0.03mm)	

Figure 19. Geometry of the PMMA Plate

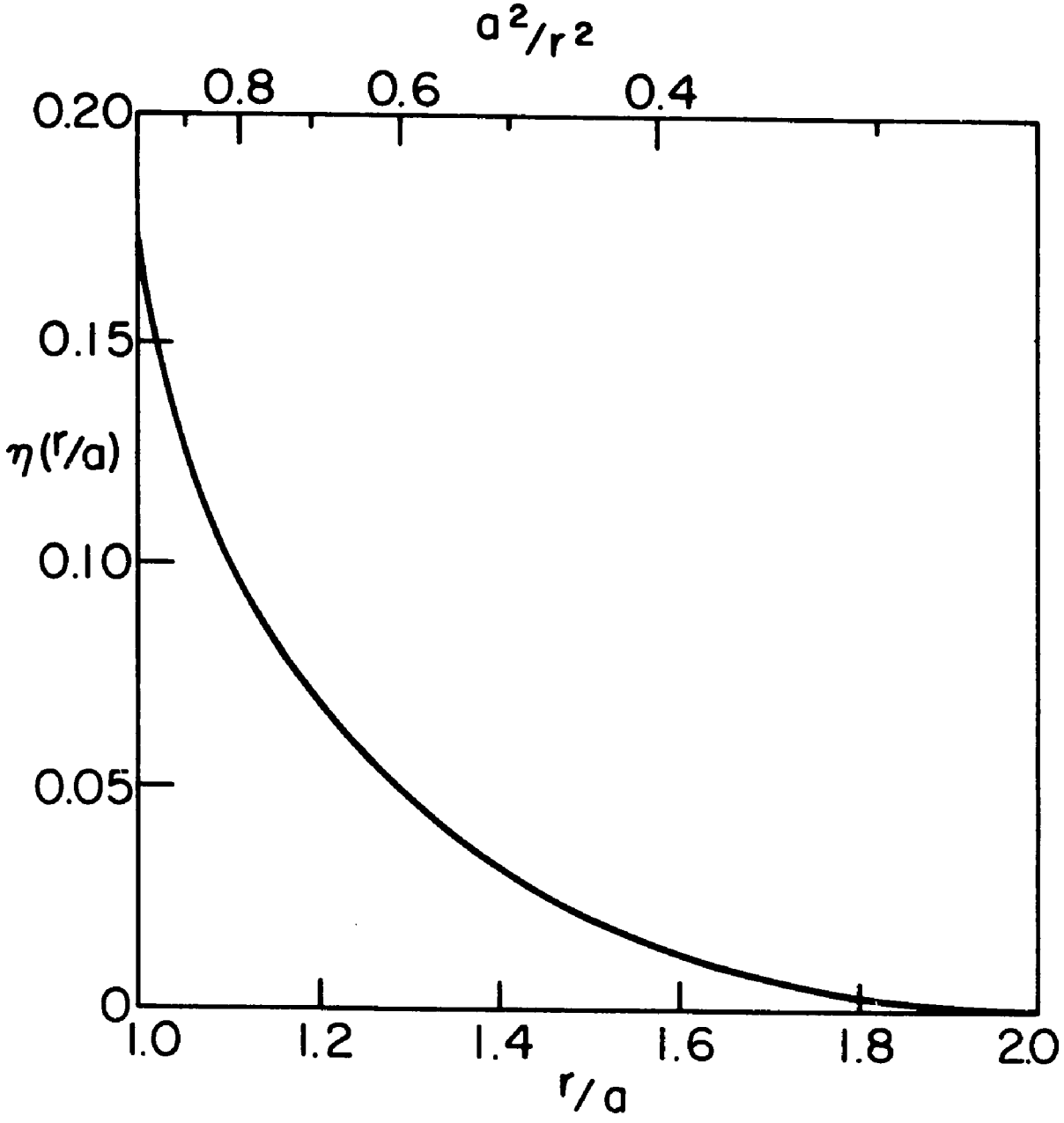

Figure 20. Distribution of the Average z-Stress in Terms of the Distance (after Alblas, reference [25])

$$\eta\left(\frac{r}{a}\right) = \frac{\bar{\sigma}_z}{\sigma_\infty \cos 2\Theta}$$

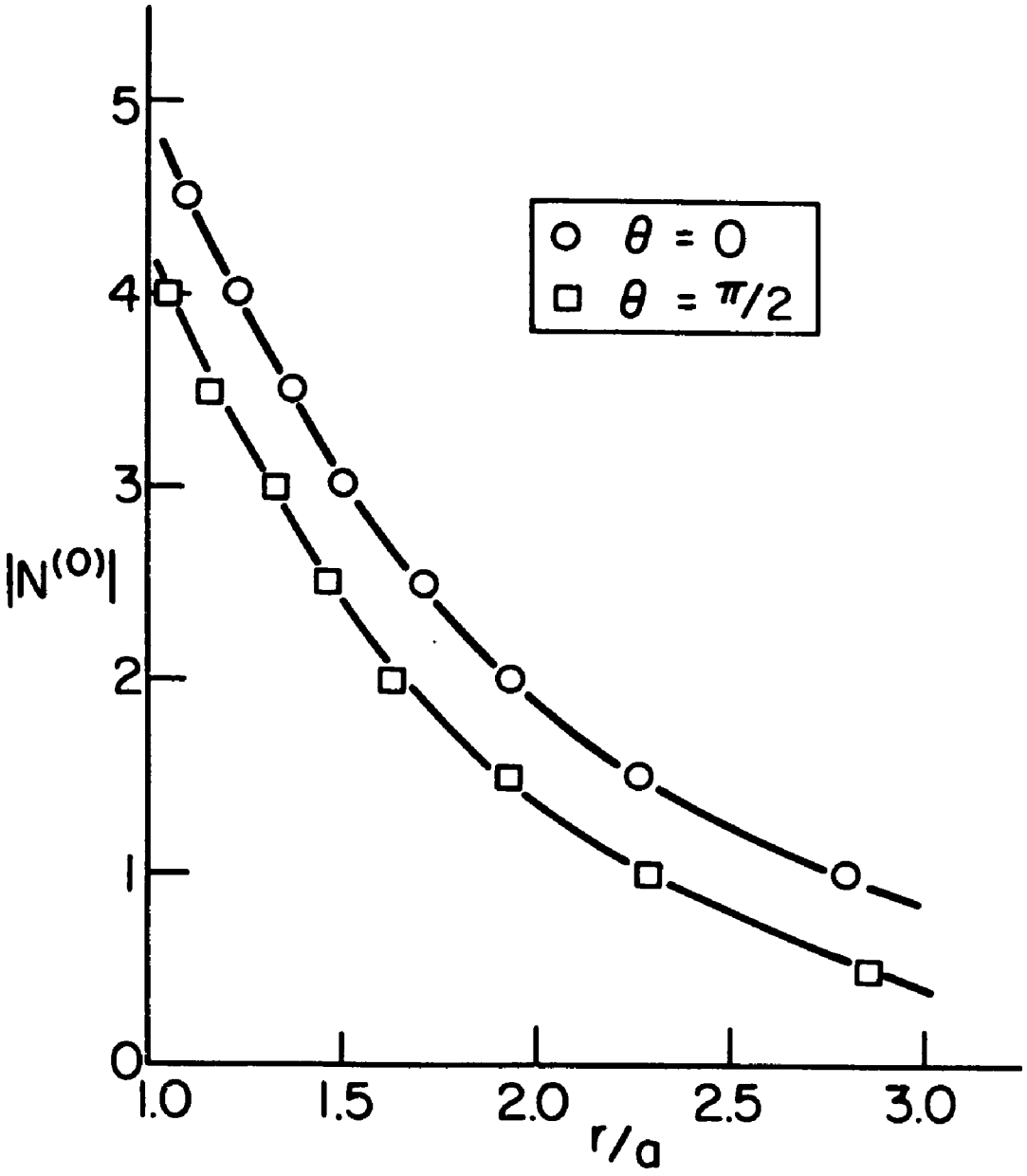

Figure 21.a Fringe Order Distribution along the Semi-Axes ($x > 0$, $y > 0$), as Obtained from the Interferogram

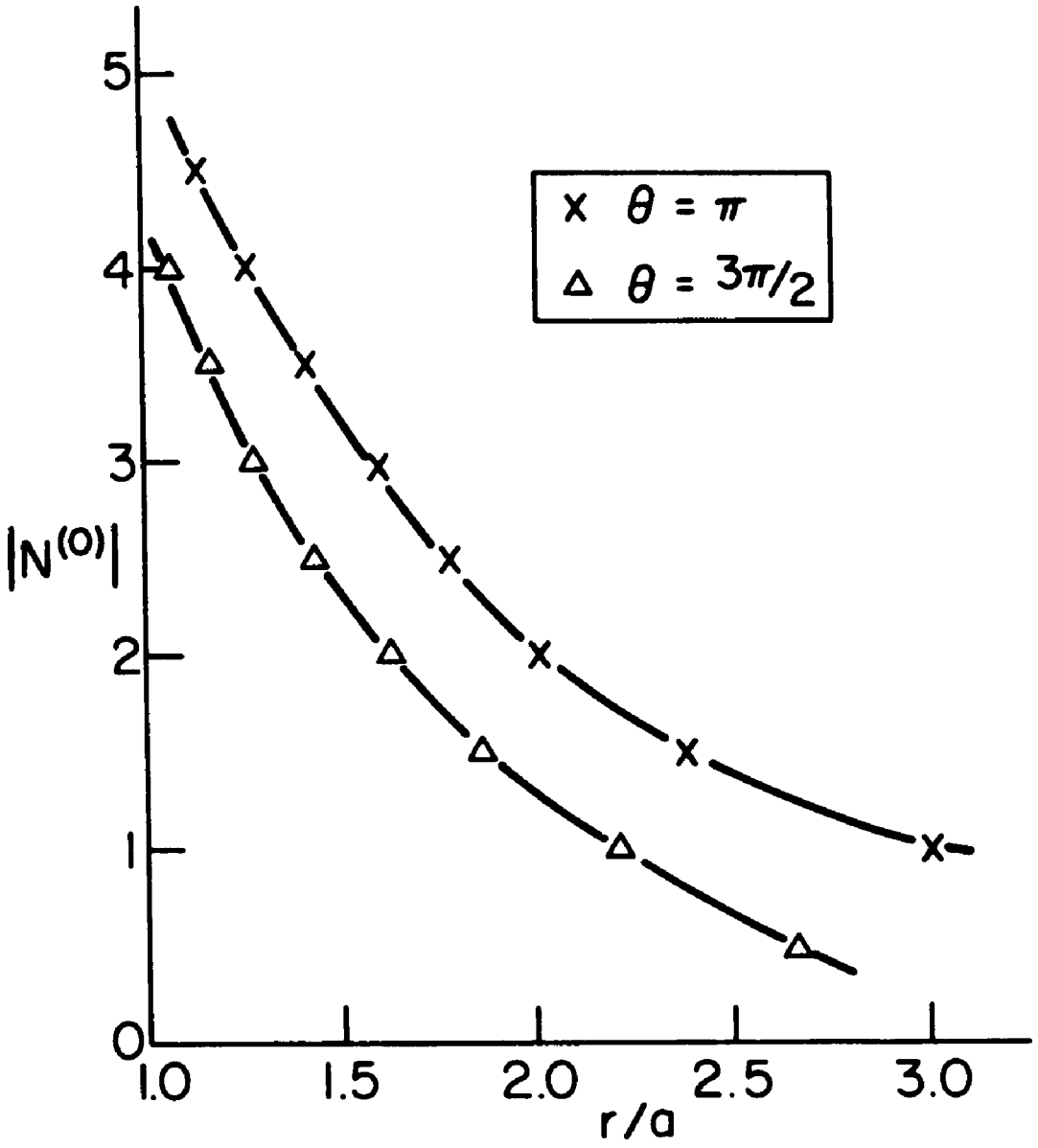

Figure 21.b Fringe Order Distribution along the Semi-Axes ($x < 0$, $y < 0$), as Obtained from the Interferogram

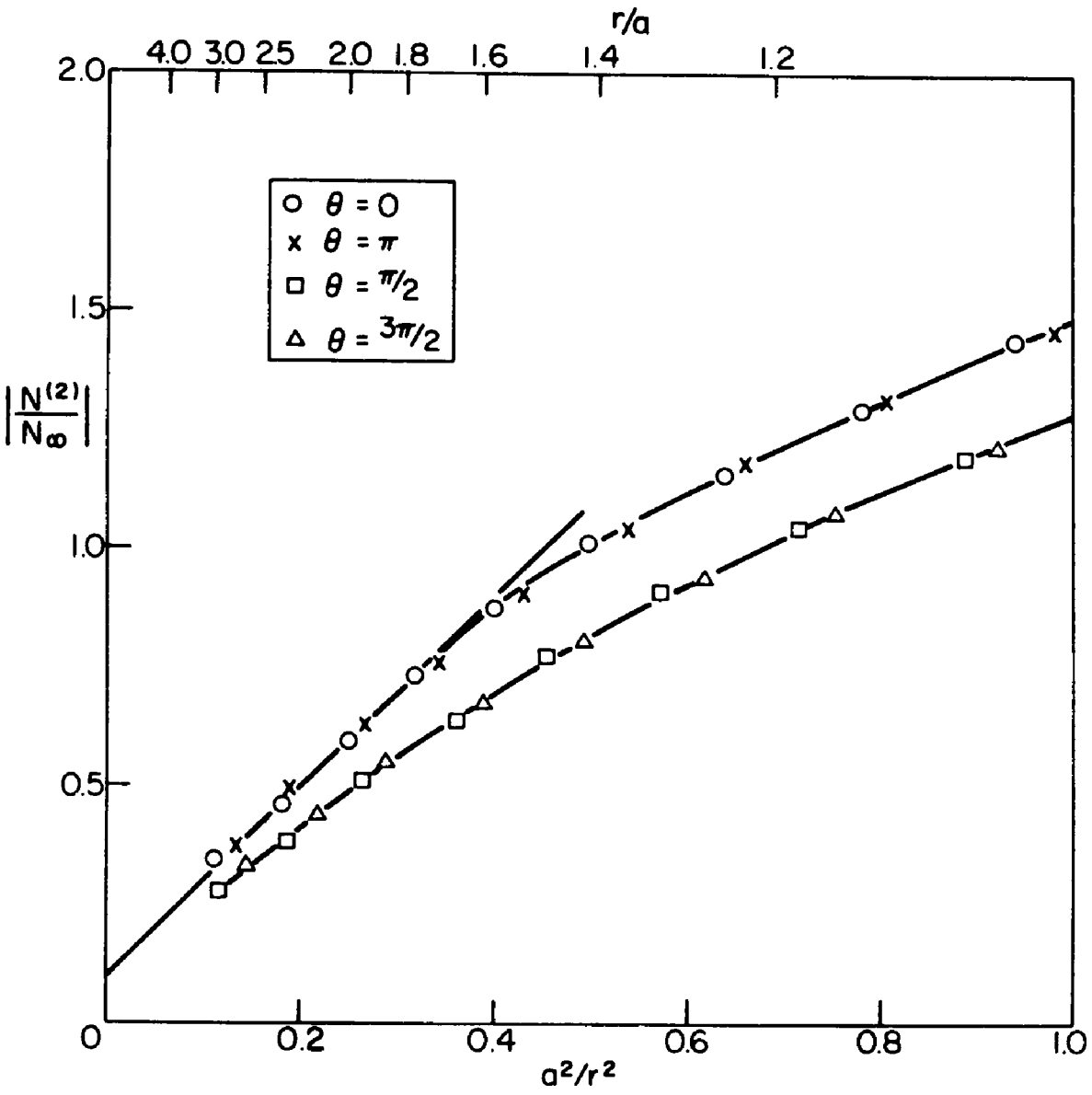

Figure 22. Normalized Reflection Fringe Order Distribution Along the Axes after Correction for Tilt Angles and Radial Displacement

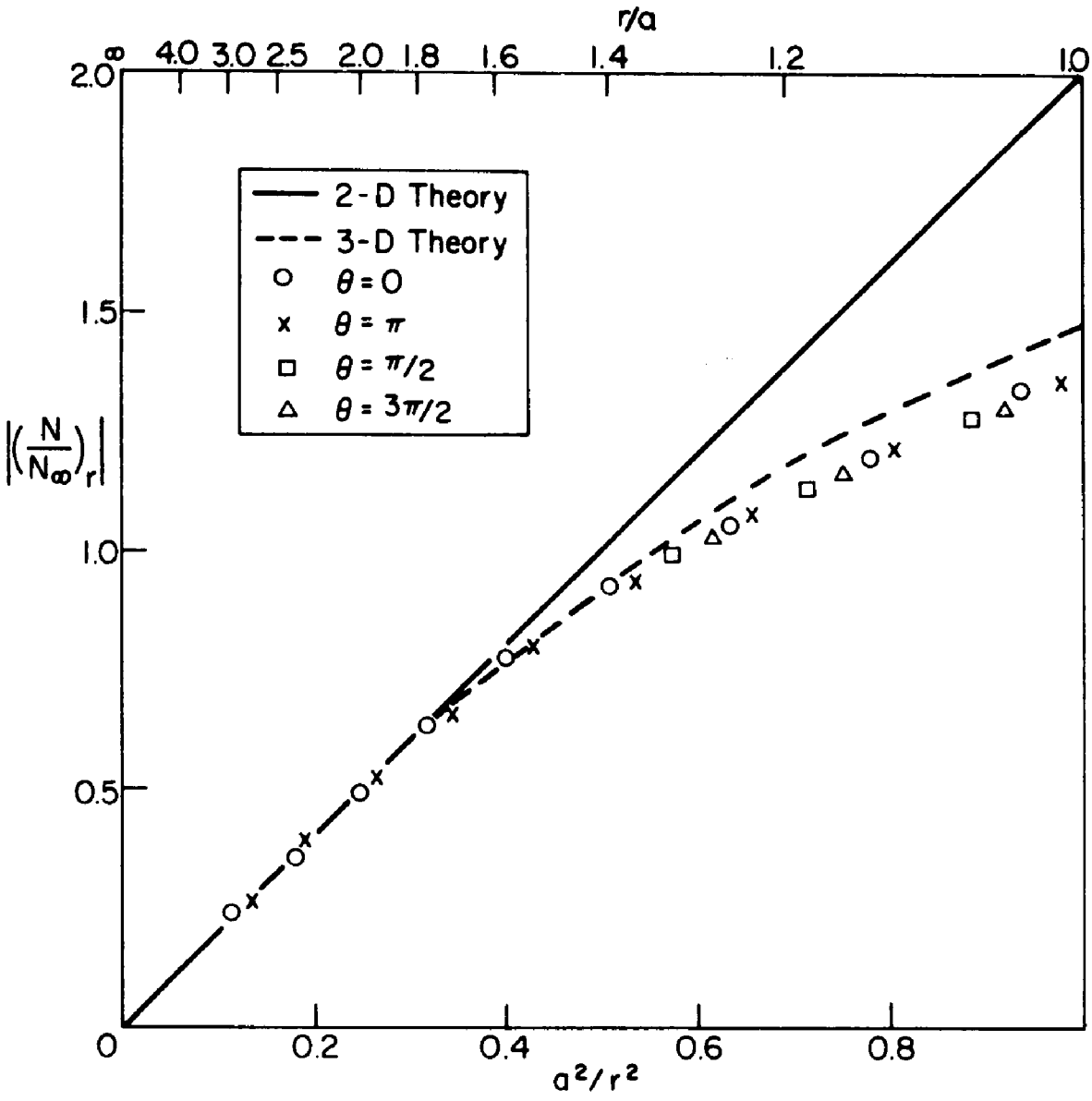

Figure 23. Normalized Reflection Fringe Order Distribution Along the Axes after all Corrections

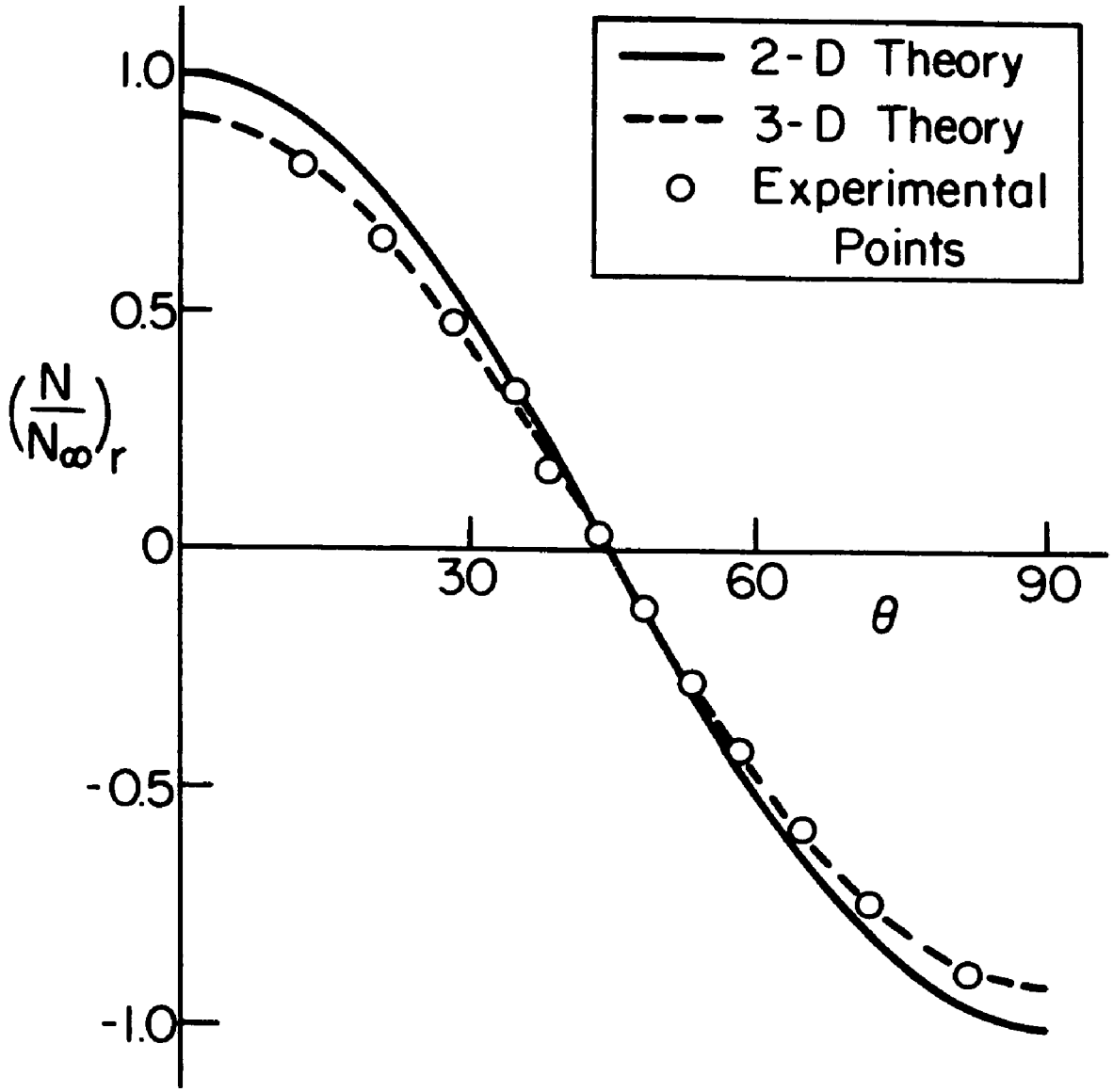

Figure 24. Normalized Reflection Fringe Order Distribution Around the Quarter Circle $r = a\sqrt{2}$; $0 < \theta < \pi/2$

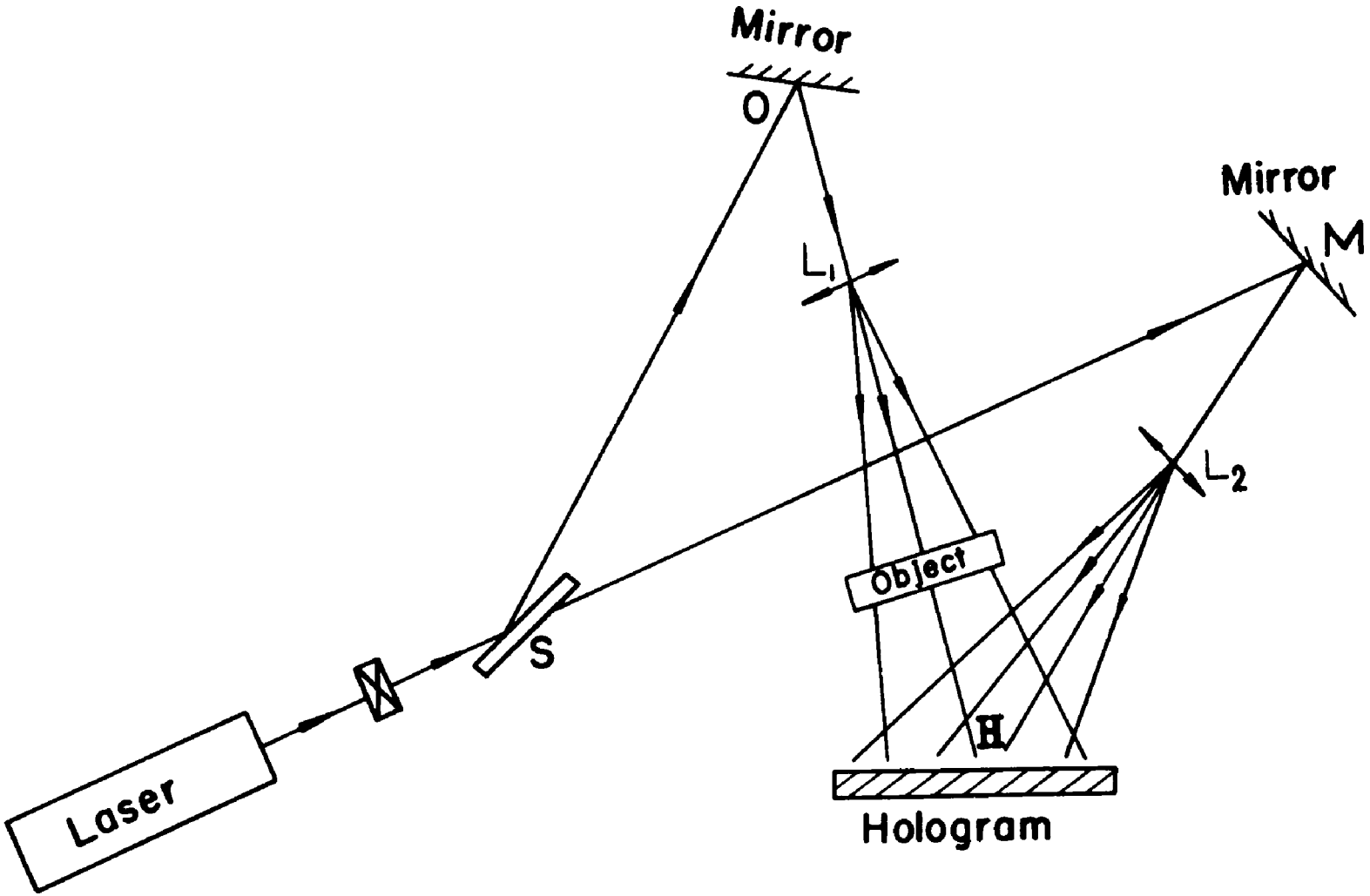

Figure 25. Basic Setting for a Transmission Hologram

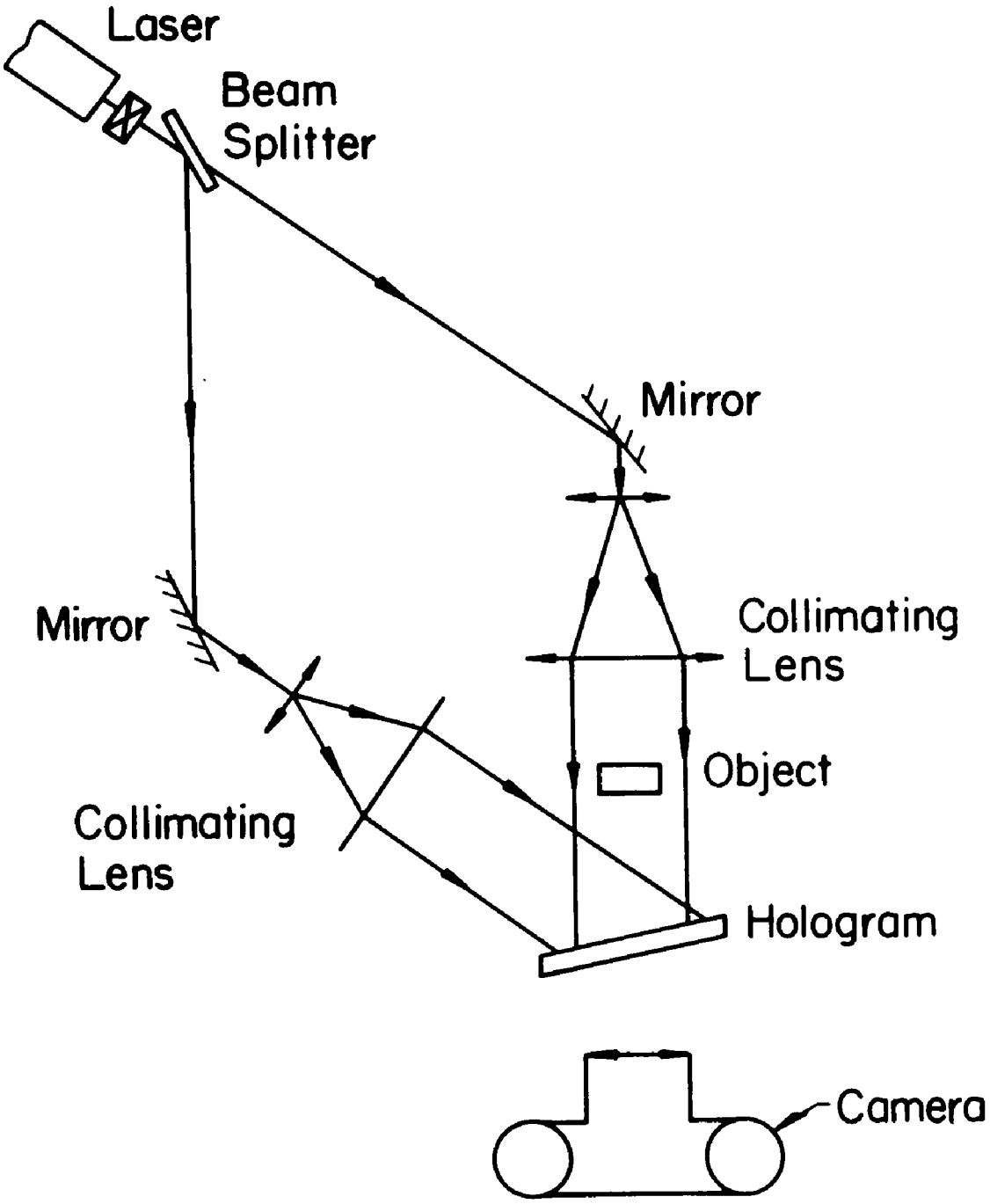

Figure 26. Geometry of a Transmission Holographic Interferometer

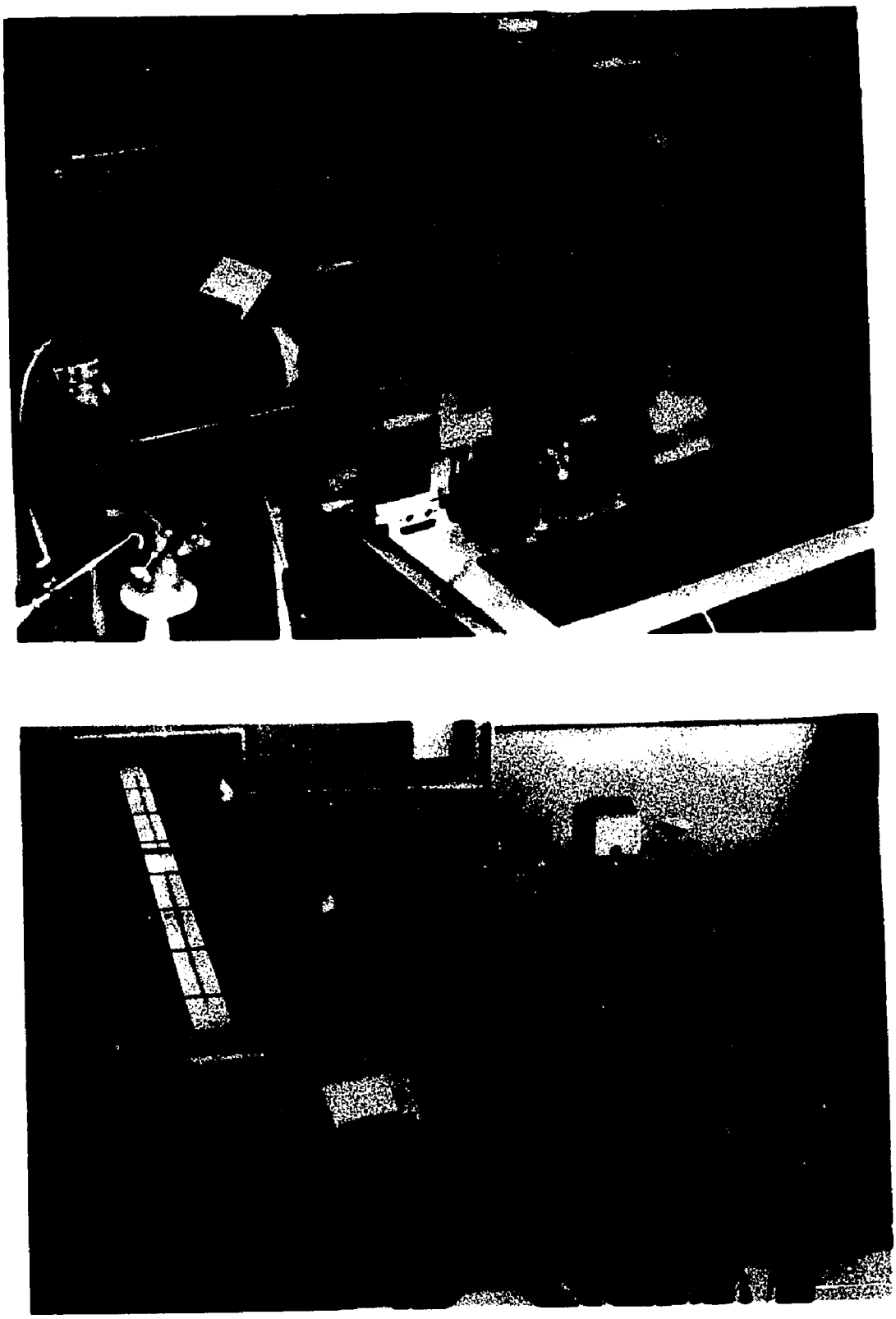

Figure 27. Photograph of the Transmission Holographic Interferometer

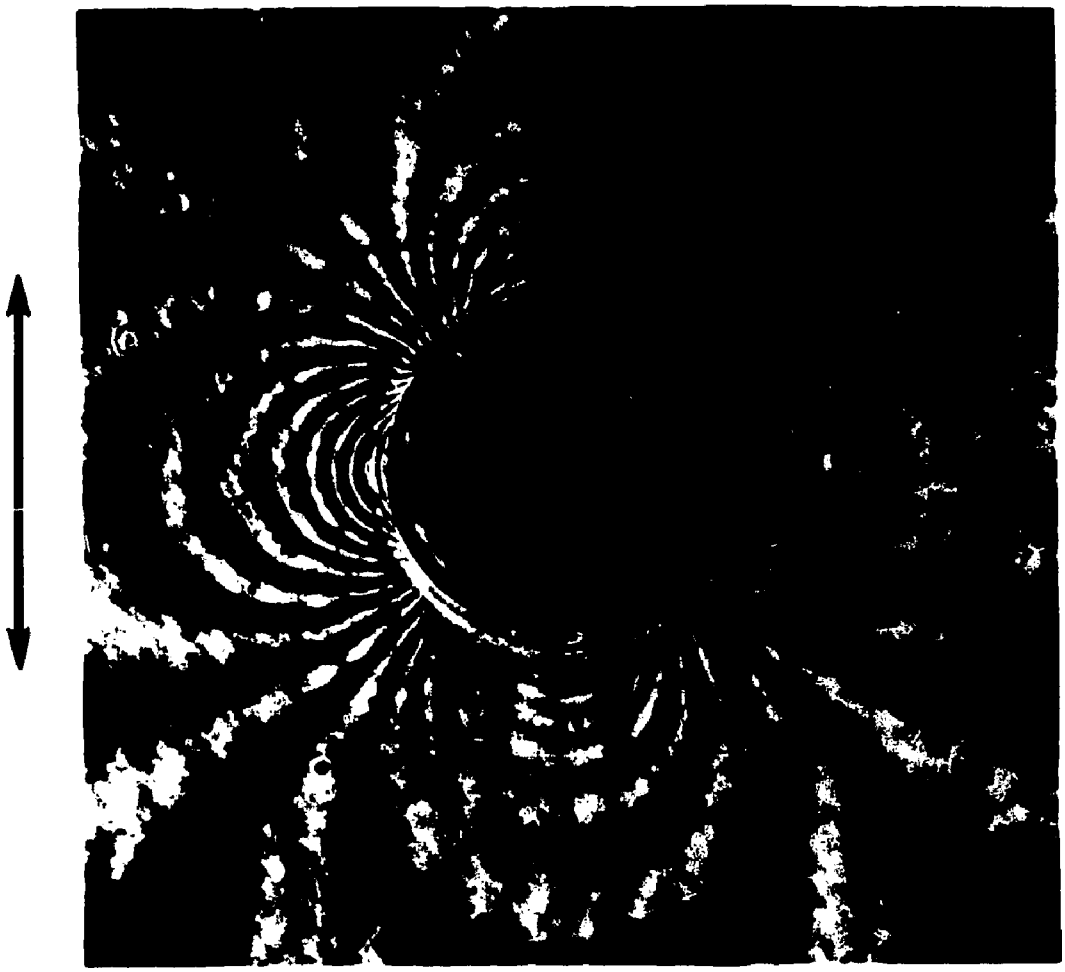

Figure 28. Transmission Holographic Interferogram for a PMMA Plate with a Central Hole under Tension; Magnification X6.4.

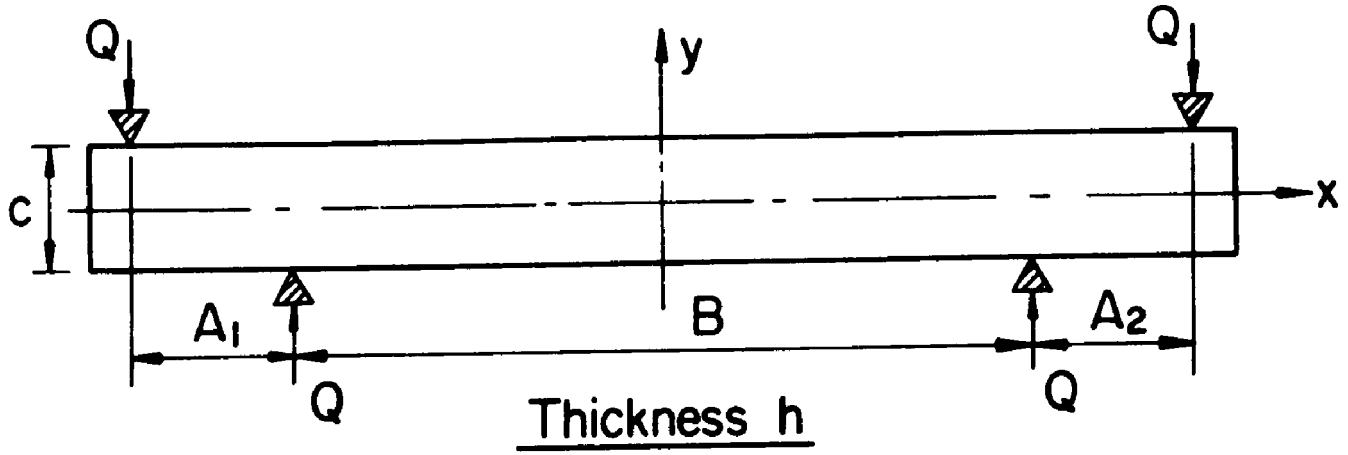

TABLE OF DIMENSIONS				
	Dimensions, in.		Dimensions, mm.	
	Nominal	Tolerance	Nominal	Tolerance
A_1, A_2	1.00	0.02	25.4	0.5
B	5.00	0.05	127.0	1.3
C	1.000	0.005	25.40	0.13
h	0.25	0.01	6.37	0.25

Figure 29. Geometry of the Four-Point Bending Calibration Specimen (PMMA)

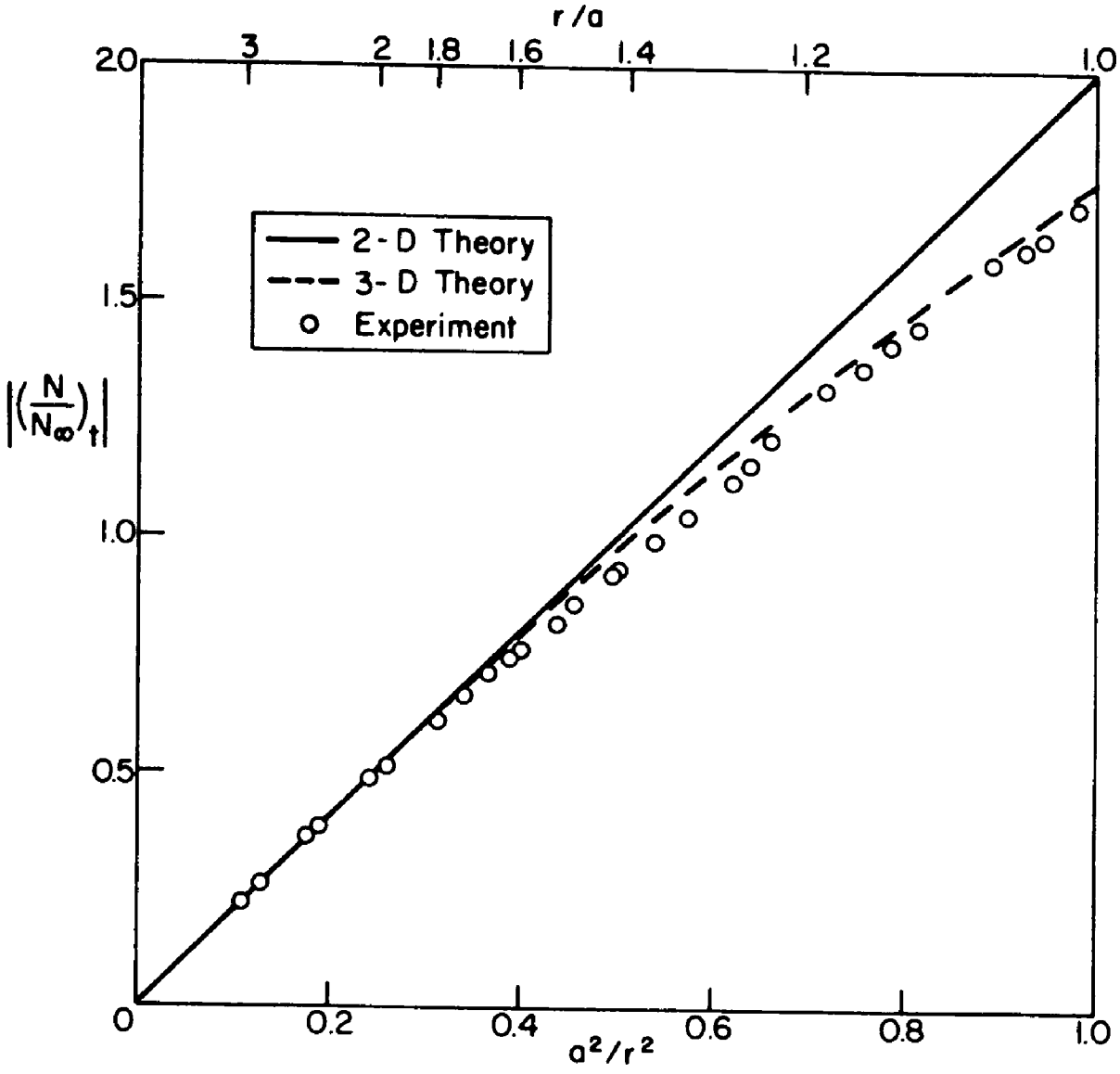

Figure 30. Normalized Transmission Fringe Order Distribution along the Axes

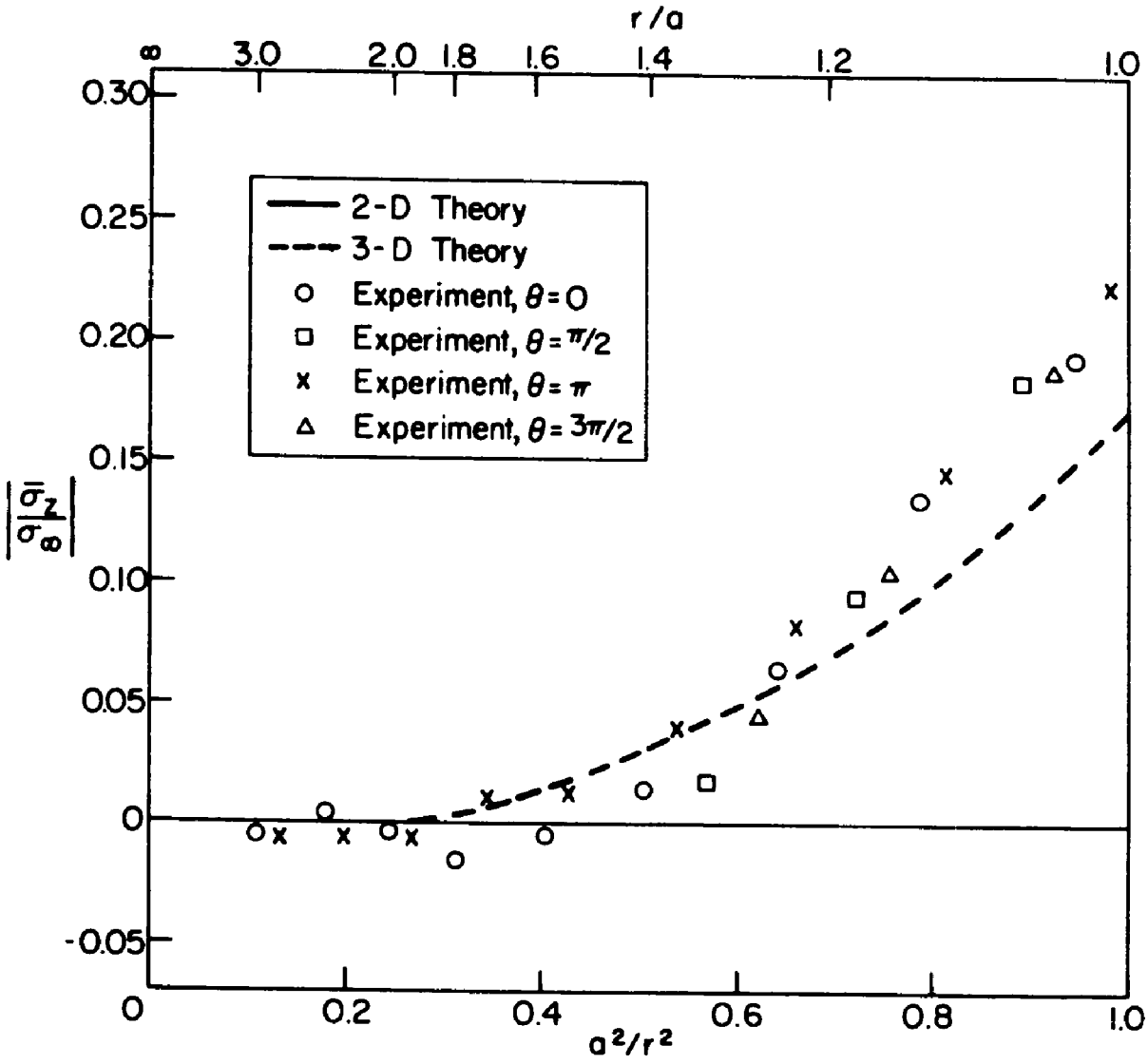

Figure 31. Distribution of the Average z-Stress along the Axes in Terms of the Distance

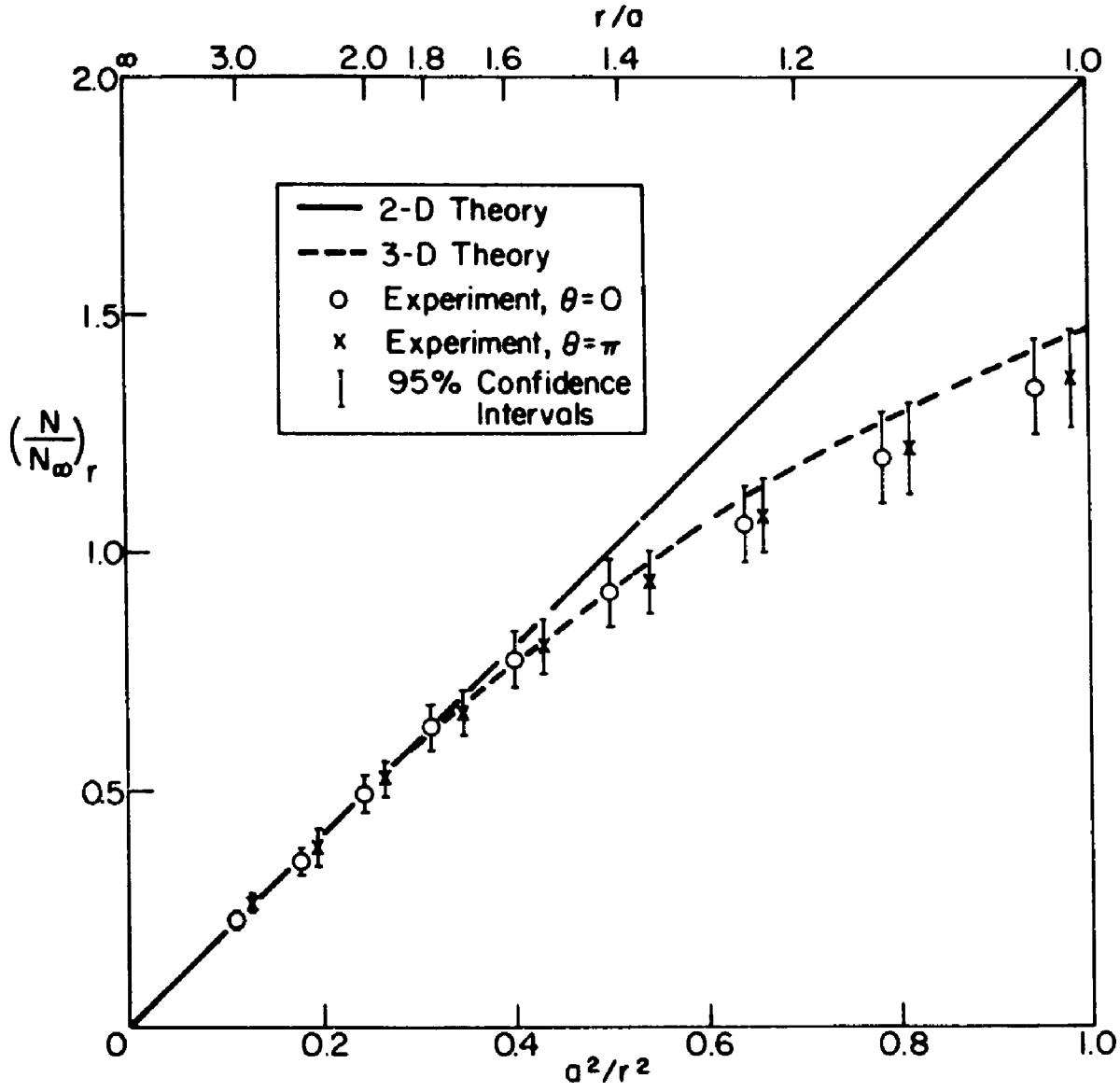

Figure 32. Normalized Reflection Fringe Order Distribution with Self-Calibration

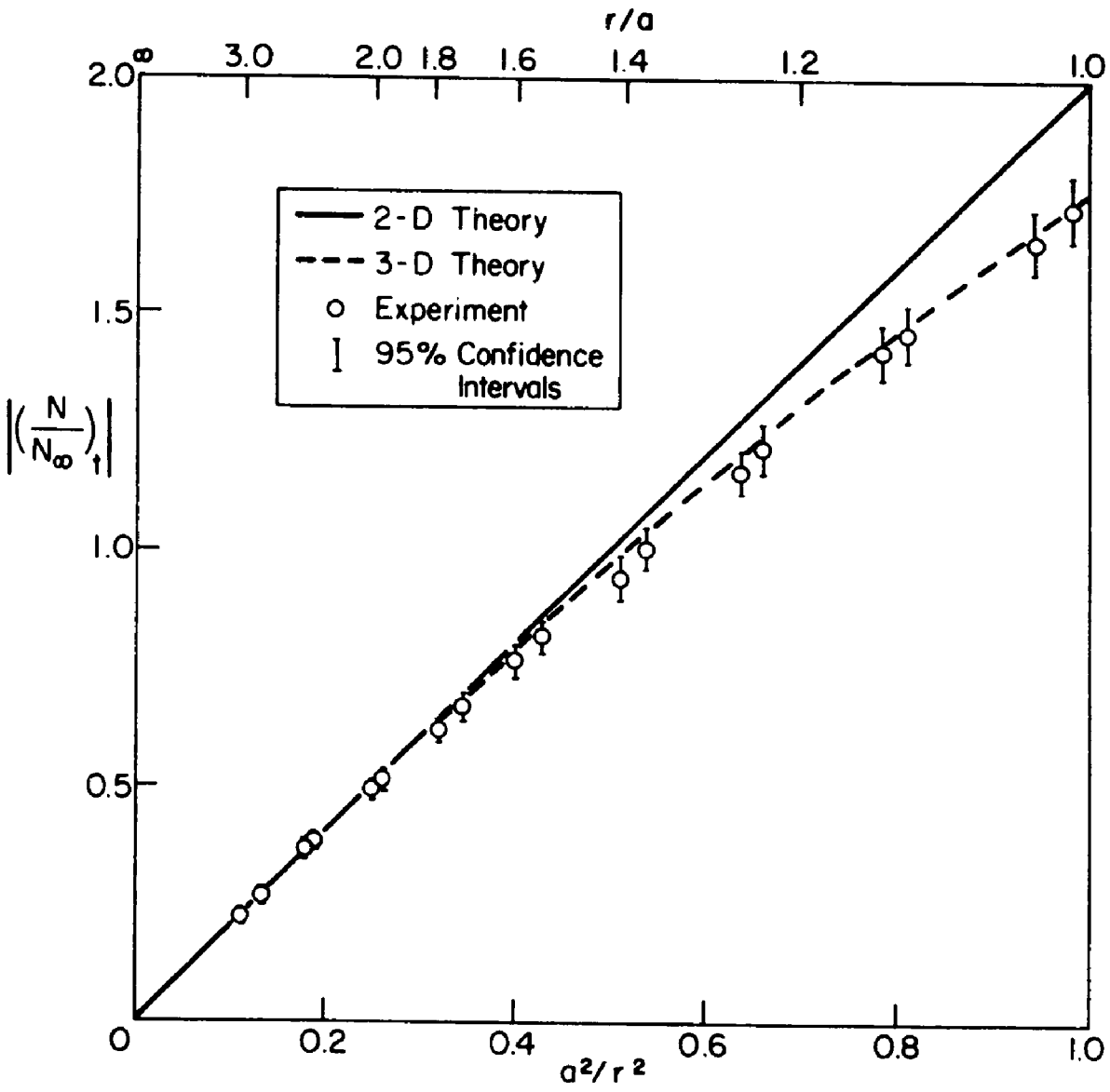

Figure 33. Normalized Transmission Fringe Order Distribution with Self-Calibration

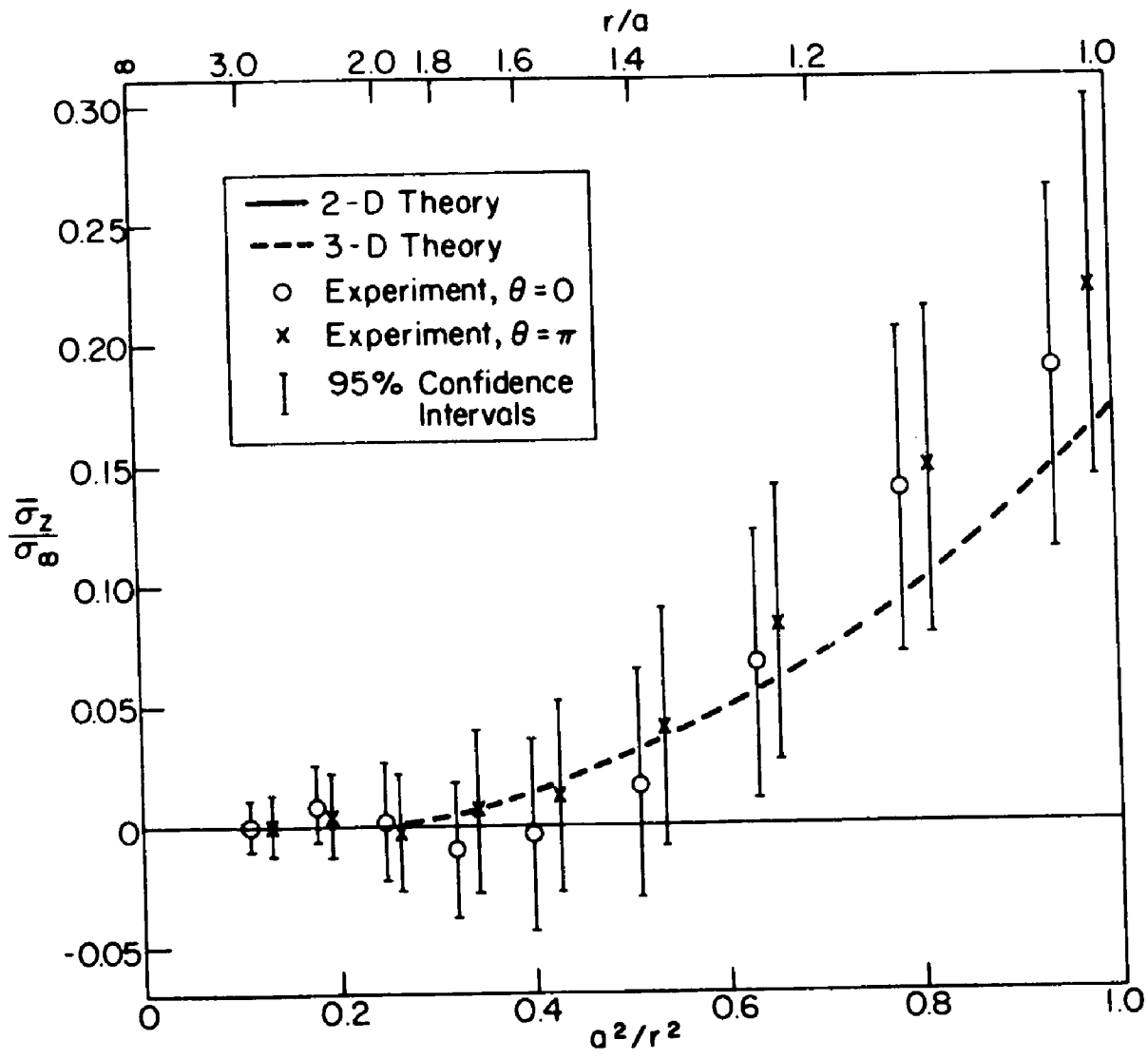

Figure 34. Distribution of the Average z-Stress Along the x-Axis in Terms of the Distance

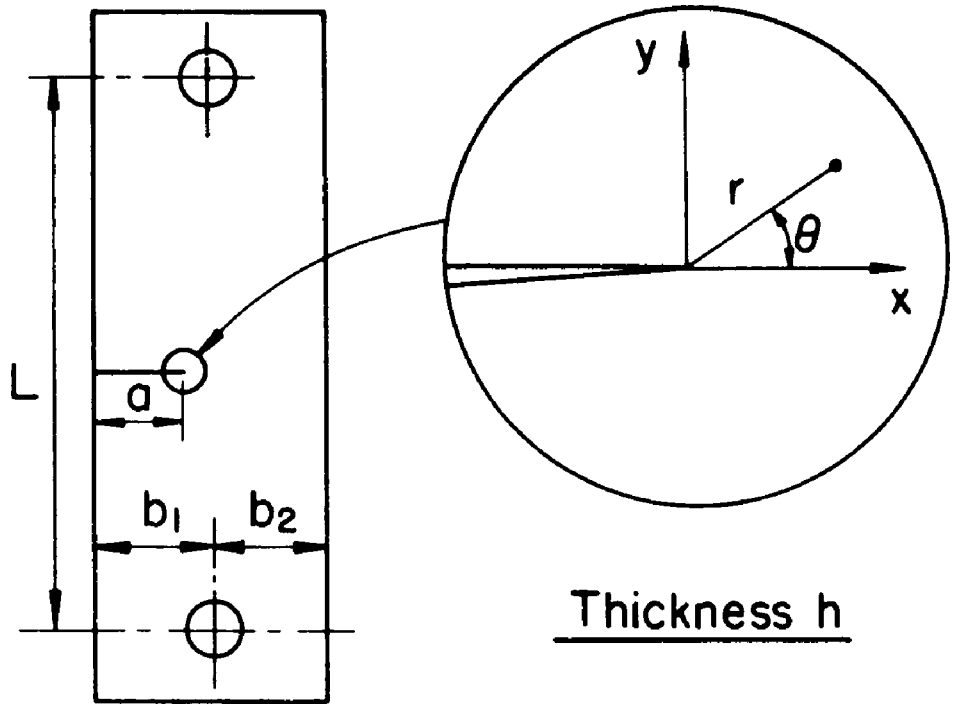

TABLE OF DIMENSIONS					
		Dimensions, in.		Dimensions, mm	
		Nominal	Tolerance	Nominal	Tolerance
aluminum	a	0.58	0.01	14.7	0.25
	b_1, b_2	0.750	0.005	19.05	0.13
	h	0.250	0.005	6.35	0.13
	L	3.00	0.01	76.2	0.25
	$b_1 = b_2 \pm 0.001$ in.				
PMMA	a	0.39	0.01	9.91	0.25
	b_1, b_2	0.500	0.005	12.7	0.13
	h	0.100	0.005	2.54	0.13
	L	2.00	0.01	50.8	0.25
	$b_1 = b_2 \pm 0.001$ in.				

Figure 35. Geometry of the Cracked Specimens (Aluminum and PMMA)

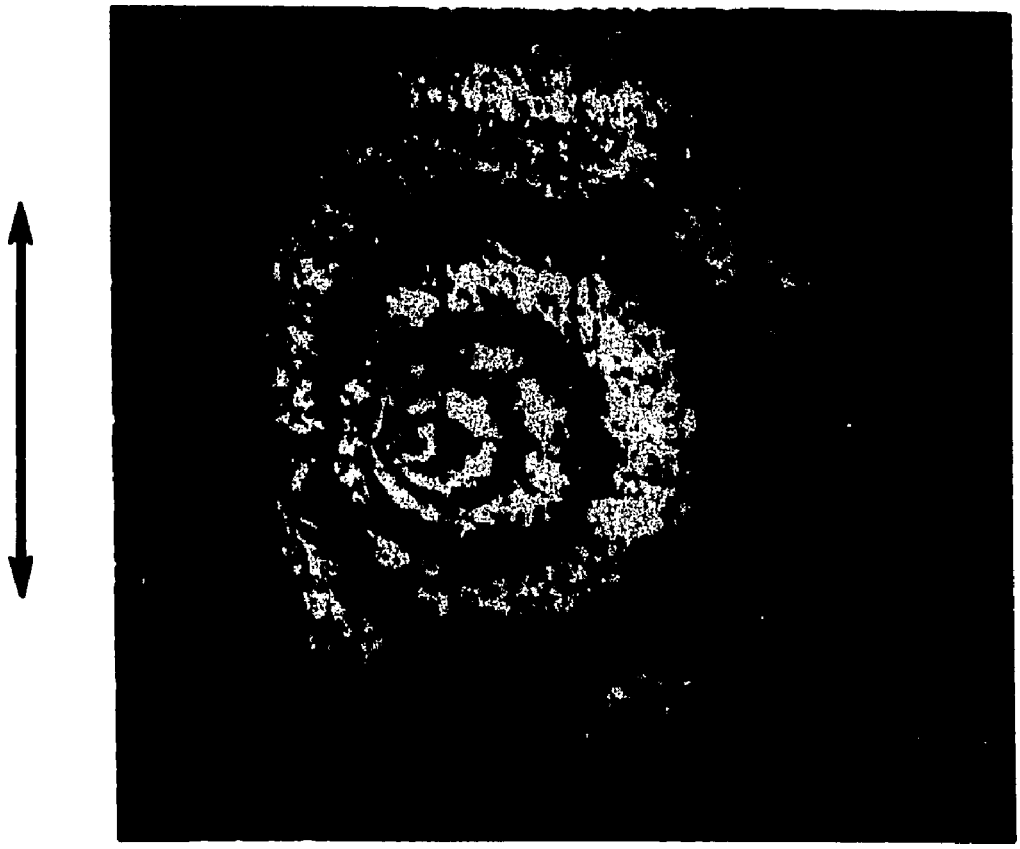

Figure 36. Reflection Holographic Interferogram for a Cracked Aluminum Plate under Tension; Magnification X6.25.

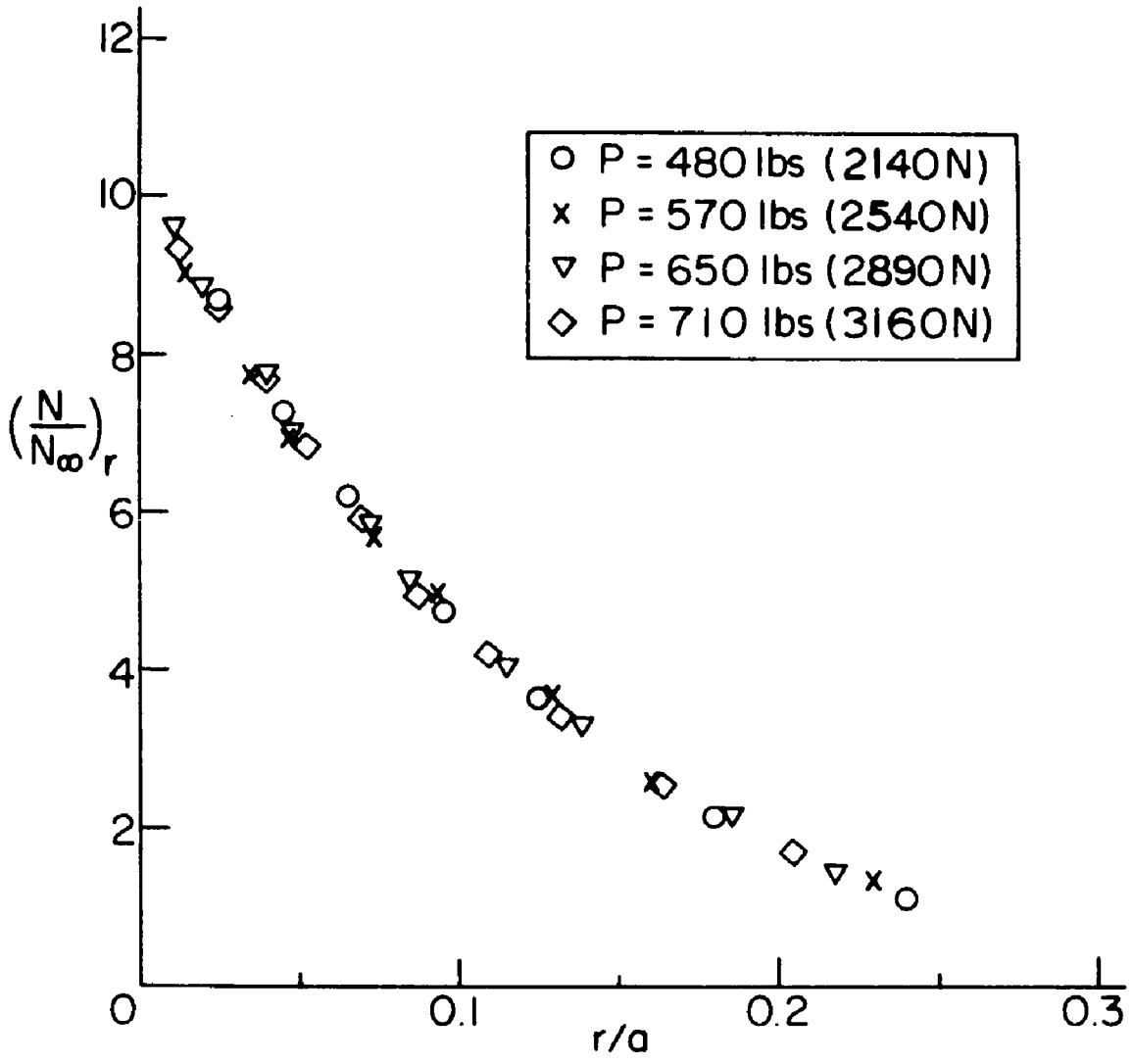

Figure 37. Normalized Reflection Fringe Order Distribution along the Crack Line Extension

Figure 38. Transmission Holographic Interferogram of a Cracked PMMA Plate under Tension; Magnification X38.

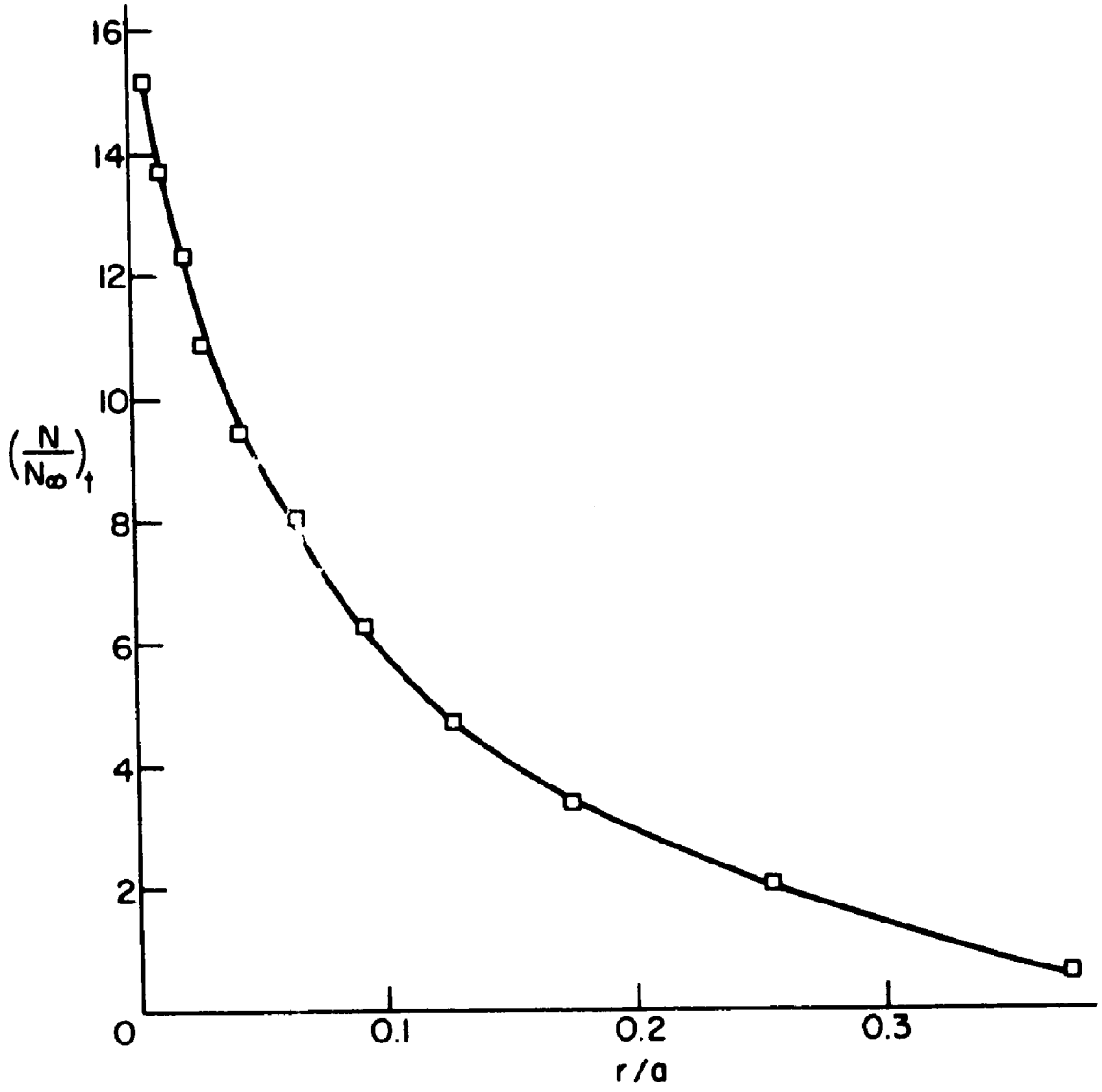

Figure 39. Normalized Transmission Fringe Order Distribution along the Crack Line Extension

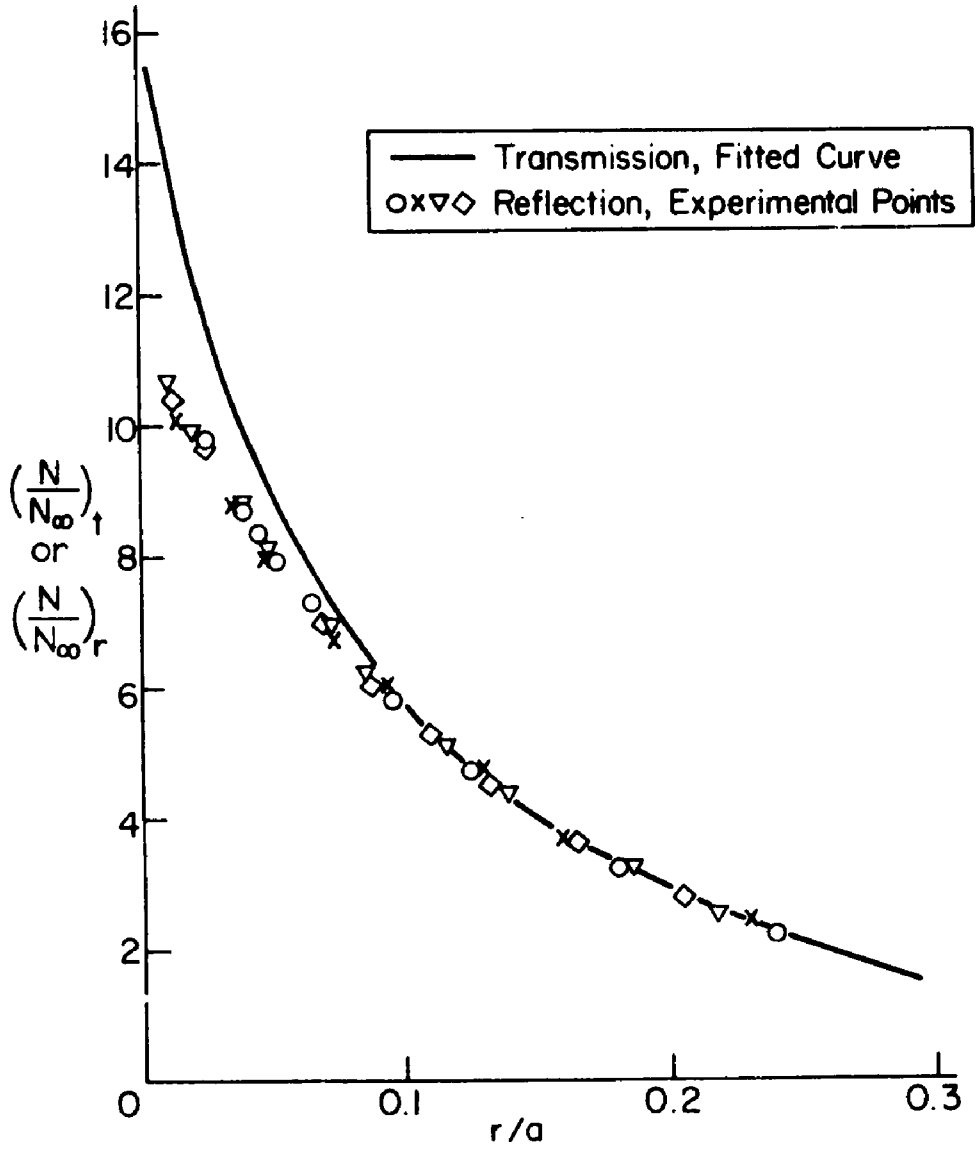

Figure 40. Superposition of the Reflection and Transmission Normalized Fringe Orders

REFERENCES

1. D. Gabor, "A New Microscopic Principle," Nature 161, 777 (1948).

2. E. Leith and J. Upatnieks, "Reconstructed Wavefronts and Communication Theory," J. Opt. Soc. Am. 52, 1123 (1962).

3. B. P. Hildebrand and K. A. Haines, "Interferometric Measurements Using the Wavefront Reconstruction Technique," Applied Optics 5, 172 (1966).

4. R. L. Powell and K. A. Stetson, "Interferometric Vibration Analysis by Wavefront Reconstruction," J. Opt. Soc. Am. 55, 1593 (1965).

5. M. Nisida and H. Saito, "A New Interferometric Method of Two-Dimensional Stress Analysis," Experimental Mechanics 4(12) 366-376 (1964).

6. R. O'Reagan and T. D. Dudderar, "A New Interferometer for Stress Analysis," Experimental Mechanics 11(6), 241-247 (1971).

7. T. D. Dudderar and R. O'Reagan, "Measurement of the Strain Field Near a Crack Tip in Polymethylmethacrylate by Holographic Interferometry," Experimental Mechanics 11(2), 49-56 (1971).

8. K. Shibayama and H. Uchiyama, "Measurement of Three-Dimensional Displacements by Holographic Interferometry," Applied Optics 10(9), 2150 (1971).

9. A. D. Wilson, "Inplane Displacement of a Stressed Membrane with a Hole Measured by Holographic Interferometry," Applied Optics 10(4), 908 (1971).

10. A. E. Ennos, "Measurement of In-Plane Surface Strain by Hologram Interferometry," Journal of Scientific Instruments, Series 2, Volume 1, 731 (1968).

11. C. A. Sciammarella and J. A. Gilbert, "Strain Analysis of a Disk Subjected to Diametial Compression by Means of Holographic Interferometry," Applied Optics 12(8), 1951 (1973).

12. J. E. Sollid, "A Comparison of Out-of-Plane Deformation and In-Plane Translation Measurements made with Holographic Interferometry," Proceedings of the Society of Photo-Optical Instrumentation Engineers: "Developments in Holography", 171-176 (1971).

13. E. B. Champagne, "Proceedings of the Society of Photo-Optical Instrumentation Engineers -- Developments in Holography," Boston, 1971.

14. L. A. Kersch, "Advanced Concepts of Holographic Non-Destructive Testing," in Optical and Acoustical Holography, 277-302, Plenum Press (1972).

15. G. Devore et R. Annequin, "Cours de Physique - Optique II," Librairie Vuibert (1966).

16. R. J. Collier, C. B. Burckhardt and L. H. Lin, "Optical Holography," Academic Press (1972).

17. K. A. Haines and B. P. Hildebrand, "Surface Deformation Measurement using the Wavefront Reconstruction Technique," Applied Optics 5, 595 (1966).

18. G. R. Fowles, "Introduction to Modern Optics," Wolf, Rinehart, Winstron, Ed. (1968).

19. F. D. Adams and G. E. Maddux, "On Speckle Diffraction Interferometry for Measuring Whole Field Displacements and Strains," AFFDL-TR-73-123 (1973).

20. J. Ch. Vienot, Cl. Froehly, J. Monneret and J. Pasteur, "Surface Displacement Fringe Analysis," in Engineering Uses of Holography, Cambridge University Press, 133 (1970).

21. S. Walles, "Visibility of Fringes in Holographic Interferometry of Diffusely Reflecting Surfaces," Arkiv fur Fysik 40, 299 (1970).

22. B. J. Howell, "Holographic Interferometry as a Means of Measuring Small Linear and Angular Displacements," in NASA SP 248, 147 (1970).

23. E. B. Aleksandrov and A. B. Bonch-Bruevich, "Investiation of Surface Strains by the Hologram Technique," Soviet Physics 12, 258 (1967).

24. J. E. Sollid, "Holographic Interferometry Applied to Measurements of Small Static Displacements of Diffusely Reflecting Surfaces," Applied Optics 8, 1587 (1969).

25. J. B. Alblas, "Theorie van de Driedimensionale Spanningstoestand in een Doorboorde Plaat," H. J. Paris - Amsterdam (1957).

26. M. M. Frocht, Photoelasticity, John Wiley and Sons, Inc. (1948).

27. Timoshenko and Goodier, Theory of Elasticity, McGraw-Hill (1970).

28. G. Villareal, "Photoelastic Investigation of a Thick Plate with a Through Thickness Crack," Ph.D. Dissertation, Lehigh University (1973).

29. G. C. Sih, "A Review of the Three-Dimensional Stress Problem for a Cracked Plate," International Journal of Fracture Mechanics 7, 1 (1971).

APPENDIX I. ANALYTICAL RESULTS AROUND A CIRCULAR HOLE IN A PLATE

The purpose of this appendix is to derive the equations giving the normalized out-of-plane surface displacement $(W_\infty - W)/W_\infty$ (equation IV-3) around a circular hole is a plate under tension. The derivation is made using two different analyses. The first one uses the hypotheses of generalized plane stress. The second is the three-dimensional analysis made by Alblas [25].

A. Results of the Generalized Plane Stress Analysis

For the set of coordinates shown in figure 19, the stresses computed from the two-dimensional analysis are:

$$\sigma_z = \tau_{xz} = \tau_{yz} = 0 \quad \text{(basic assumption)}$$

$$\sigma_r = \frac{\sigma_\infty}{2}\left(1 - \frac{a^2}{r^2}\right) - \frac{\sigma_\infty}{2}\left(1 - \frac{4a^2}{r^2} + \frac{3a^4}{r^4}\right)\cos 2\theta$$

$$\sigma_\theta = \frac{\sigma_\infty}{2}\left(1 + \frac{a^2}{r^2}\right) + \frac{\sigma_\infty}{2}\left(1 + \frac{3a^4}{r^4}\right)\cos 2\theta \qquad \text{(A-1)}$$

$$\tau_{r\theta} = \frac{\sigma_\infty}{2}\left(1 - \frac{2a^2}{r^2} - \frac{3a^4}{r^4}\right)\sin 2\theta$$

The normal surface displacement $w(\frac{h}{2})$ is referred to as W:

$$w\left(\frac{h}{2}\right) = W = -\frac{h\nu}{2E}(\sigma_r + \sigma_\theta)$$

$$W = -\frac{h\nu}{2E}\,\sigma_\infty\left[1 + \frac{2a^2}{r^2}\cos 2\theta\right]$$

At "infinity", the normal stresses are $\sigma_y = \sigma_\infty$; $\sigma_x = \sigma_z = 0$. This gives a surface displacement W_∞:

$$W_\infty = -\frac{h\nu}{2E}\sigma_\infty \qquad \text{(A-2)}$$

The normalized surface displacement is thus:

$$\frac{W_\infty - W}{W_\infty} = \frac{2a^2}{r^2}\cos 2\theta \qquad \text{(A-3)}$$

B. Results of the Three-Dimensional Analysis

An estimate of the three-dimensional effect was obtained by using some results from the analysis by Alblas [25]. This Alblas analysis gives the variation of all the stress components through the thickness of the plate. The results are identical to those of the plane stress analysis at large distances from the hole; but the analyses differ significantly close to the hole boundary. The influence of this discrepancy on the change in thickness was evaluated numerically. For this evaluation, only the σ_z component of stresses was taken into account. The difference in σ_r and σ_θ between the two theories appears to have a negligible effect on the change in thickness. At the hole boundary, the stress σ_r is zero in both cases, and the average value of σ_θ through the thickness is given in figure 6 of Alblas' paper. This result for the average value of σ_θ from the three-dimensional analysis turns out to be the same as in the two-dimensional theory, within two or three percent. When multiplied by the Poisson's ratio, the final influence of this discrepancy on the change in thickness is less than one percent, which can be neglected.

The influence of the σ_z component is evaluated from the data given in figure 3 of Alblas' paper. This figure is reproduced here as figure 20 and gives the average value of σ_z ($\bar{\sigma}_z$) through the thickness as a function of position through the quantity $\eta(\frac{r}{a})$.

$$\eta(\frac{r}{a}) = \frac{\bar{\sigma}_z}{\sigma_\infty \cos 2\theta} \tag{A-4}$$

where

$$\bar{\sigma}_z = \int_{-\frac{h}{2}}^{\frac{h}{2}} \sigma_z \, dZ$$

The strain in the z-direction is:

$$\epsilon_z = \frac{1}{E} [\sigma_z - \nu(\sigma_r + \sigma_\theta)]$$

At a large distance from the hole, the z-strain is:

$$\epsilon_{z\infty} = -\frac{\nu}{E} \sigma_\infty \tag{A-5}$$

$$\epsilon_z - \epsilon_{z\infty} = \frac{1}{E} [\bar{\sigma}_z - \nu(\bar{\sigma}_r + \bar{\sigma}_\theta - \sigma_\infty)] \tag{A-6}$$

Averaging through the thickness:

$$\overline{\epsilon_z - \epsilon_{z\infty}} = \frac{1}{E} [\sigma_z - \nu(\sigma_r + \sigma_\theta - \sigma_\infty)] \tag{A-7}$$

Since the average value of σ_r and σ_θ is very close to what it is in the two-dimensional analysis:

$$\bar{\sigma}_r + \bar{\sigma}_\theta - \sigma_\infty \simeq \frac{2a^2}{r^2} \sigma_\infty \cos 2\theta$$

Also using equation A-4, equation A-7 becomes:

$$\overline{\epsilon_z - \epsilon_{z\infty}} = -\frac{\sigma_\infty}{E}\left[2\nu\,\frac{a^2}{r^2} - \eta\left(\frac{r}{a}\right)\right]\cos 2\theta$$

The normal surface displacement W, referred to its value "at infinity", is thus:

$$W - W_\infty = \frac{h}{2}\left(\overline{\epsilon_z - \epsilon_{z\infty}}\right) \tag{A-8}$$

$$W - W_\infty = \frac{h\nu}{2E}\,\sigma_\infty\left[\frac{2a^2}{r^2} - \frac{1}{\nu}\,\eta\left(\frac{r}{a}\right)\right]\cos 2\theta$$

Using equation A-2, the normalized surface displacement is:

$$\frac{W - W_\infty}{W_\infty} = \left[\frac{2a^2}{r^2} - \frac{1}{\nu}\,\eta\left(\frac{r}{a}\right)\right]\cos 2\theta \tag{A-9}$$

APPENDIX II. CORRECTION FACTORS FOR PROCESSING THE REFLECTION DATA

Three correction factors η_t, η_r and η_c are introduced in the processing of reflection interferometic data. The numerical values of the first two, η_t and η_r are computed in this appendix.

A. Correction for Tilt Angle (η_t)

The correction factor η_t is given by equation IV-10:

$$\eta_t(x,y) = -\frac{r}{\lambda}(\alpha - 2\varphi) \tag{A-10}$$

where $(\alpha - 2\varphi)$ is the component of the uncorrected tilt about an axis perpendicular to Or. Its use over the whole plane requires the rotation components about two different axes to be known. Along the x and y axes:

$$\eta_t(x,0) = -\frac{x}{\lambda}(\alpha - 2\varphi)_y$$

$$\eta_t(0,y) = -\frac{y}{\lambda}(\alpha - 2\varphi)_x \tag{A-11}$$

From the symmetry of the plate, $W(x,0) = W(-x,0)$. In equation IV-12, N_∞ and η_c are constants, and $\eta_r(x,0) = \eta_r(-x,0)$. Writing equation IV-12 at the points (x,0) and (-x,0), the following result is obtained by sustraction:

$$\eta_t(x,0) = -\frac{1}{2}\left[N^{(o)}(x,0) - N^{(o)}(-x,0)\right] \tag{A-12}$$

Together with equation A-11, equation A-12 yields:

$$\frac{(\alpha - 2\varphi)_y}{\lambda} = \frac{N^{(o)}(x,0) - N^{(o)}(-x,0)}{2x} \tag{A-13}$$

A similar expression would be readily obtained for $(\alpha - 2\varphi)_x$. In equation A-13, the best possible estimate of $(\alpha - 2\varphi)_y$ is to be obtained from the available experimental data. This is done by computing the mean value of the right-hand side of equation A-13 over the range of available data. This range is $a < r < 3a$. The estimate can thus be taken as:

$$\frac{(\alpha - 2\varphi)_y}{\lambda} \approx \frac{1}{2a} \int_a^{3a} \frac{N^{(o)}(x,0) - N^{(o)}(-x,0)}{2x} \, dx \qquad \text{(A-14)}$$

This mean value can also be computed approximately by picking m equidistant points x_j over the range of data. Then:

$$\frac{(\alpha - 2\varphi)_y}{\lambda} \approx \frac{1}{m} \sum_{j=1}^{m} \frac{N^{(o)}(x_j,0) - N^{(o)}(-x_j,0)}{2x_j}$$

$$\frac{(\alpha - 2\varphi)_x}{\lambda} \approx \frac{1}{m} \sum_{j=1}^{m} \frac{N^{(o)}(0,y_j) - N^{(o)}(0,-y_j)}{2y_j} \qquad \text{(A-15)}$$

Once the uncorrected tilt angle $(\alpha - 2\,y)$ about the axes Ox and Oy have been computed, the correction at a point of coordinates (x,y) is simply:

$$\eta_t(x,y) = -x \frac{(\alpha - 2\varphi)_y}{\lambda} - y \frac{(\alpha - 2\varphi)_x}{\lambda} \qquad \text{(A-16)}$$

Practically, the fringe pattern is projected onto radial graph paper. The fringe order $N^{(o)}$ along the axes Ox and Oy is plotted in terms of r (i.e., x or y, when $\theta = 0, \pi/2, \pi, 3\pi/2$) in

figure 21. Smooth curves are fitted through the experimental points along the four semi-axes. The quantities that are needed for the correction are $[(\alpha - 2\varphi)_y/\lambda]$ and $[(\alpha - 2\varphi)_x/\lambda]$. They are estimated from equations A-15, where the measurement intervals are chosen to be:

$$|x_{j+1} - x_j| = |y_{j+1} - y_j| = 0.1\ a$$

The fringe orders $N^{(o)}(x_j)$ to be used in equation A-15 are taken from the fitted curve of figure 21, since there is generally no original data point at the distance x_j. Numerically, this averaging process gives:

$$\frac{(\alpha - 2\varphi)_y}{\lambda} \simeq -0.031$$
$$\frac{(\alpha - 2\varphi)_x}{\lambda} \simeq 0.045 \qquad \text{(A-17)}$$

These numerical values are used in equation IV-17 to compute the tilt angle correction.

B. Correction for Radial Displacement (η_r)

The radial displacement at a point (r,θ) is:

$$u_r = u_a + \int_a^r \epsilon_r\, dr \qquad \text{(A-18)}$$

where the displacement u_a at the hole boundary is unknown, and:

$$\epsilon_r = \frac{1}{E}(\sigma_r - \nu\sigma_\theta) \qquad \text{(A-19)}$$

Using the two-dimensional solution (equations A-1) for the stresses, equation A-19 gives:

$$\epsilon_r = \frac{\sigma_\infty}{2E}\left\{\left[\left(1 - \frac{a^2}{r^2}\right) - \left(1 - \frac{4a^2}{r^2} + \frac{3a^4}{r^4}\right)\cos 2\theta\right]\right.$$

$$\left. - \nu\left[\left(1 + \frac{a^2}{r^2}\right) + \left(1 + \frac{3a^4}{r^4}\right)\cos 2\theta\right]\right\} \qquad \text{(A-20)}$$

$$\epsilon_r = \frac{\sigma_\infty}{2E}\left\{\left[1 - \nu - (1+\nu)\cos 2\theta\right] - \frac{a^2}{r^2}\left[1 + \nu - 4\cos 2\theta\right]\right.$$

$$\left. - \frac{3a^4}{r^4}\left[(1+\nu)\cos 2\theta\right]\right\}$$

or,
$$\epsilon_r = \frac{\sigma_\infty}{2E}\left[B + C\frac{a^2}{r^2} + 3D\frac{a^4}{r^4}\right]$$

The radial displacement is then:

$$u_r = u_a(\theta) + \frac{\sigma_\infty}{2E}\left[Br + C\frac{a^2}{r^2} + D\frac{a^4}{r^4}\right]_a^r \qquad \text{(A-21)}$$

At a large distance from the hole, the displacements are the same as they would be without the hole. The stresses would then be uniform:

$$\sigma_r = \frac{\sigma_\infty}{2}\left[1 - \cos 2\theta\right]$$

$$\sigma_\theta = \frac{\sigma_\infty}{2}\left[1 + \cos 2\theta\right]$$

The radial strain would be:

$$\epsilon_r = \frac{\sigma_\infty}{2E}\left[1 - \nu - (1+\nu)\cos 2\theta\right]$$

and the displacement:

$$u_r = \frac{\sigma_\infty}{2E} [1 - \nu - (1 + \nu) \cos 2\theta] r$$

This expression gives the asymptotic behavior of u_r in equation A-21, showing that:

$$u_a (\theta) + \frac{\sigma_\infty}{2E} [B + C + D] a = 0$$

The radial displacement is thus:

$$u_r (r,\theta) = \frac{\sigma_\infty}{2E} \{ [1 - \nu - (1 + \nu) \cos 2\theta] r + [1 + \nu - 4 \cos 2\theta] \frac{a^2}{r}$$

$$+ [(1 + \nu) \cos 2\theta] \frac{a^4}{r^3} \} \qquad \text{(A-22)}$$

The data are to be collected along the horizontal and vertical diameter extensions and around the circle of radius $r = a\sqrt{2}$. The numerical values of the corrective term at these locations come as follows:

1. Diameter Extensions

Along the horizontal diameter extensions, $\theta = (0,\pi)$; $\cos 2\theta = 1$. Equation A-22 becomes:

$$u_{rh} = \frac{\sigma_\infty a^2}{2E} f_h(r) \qquad \text{(A-23)}$$

$$f_h(r) = -2\nu \frac{r}{a^2} - (3 - \nu) \frac{1}{r} + (1 + \nu) \frac{a^2}{r^3} \qquad \text{(A-24)}$$

Along the vertical diameter, $\theta = (\frac{\pi}{2} , \frac{3\pi}{2})$; $\cos \theta = -1$.

$$u_{rv} = \frac{\sigma_\infty a^2}{2E} f_v(r) \qquad \text{(A-25)}$$

where:

$$f_v(r) = 2\frac{r}{a^2} + (5 + \nu)\frac{1}{r} - (1 + \nu)\frac{a^2}{r^3} \qquad \text{(A-26)}$$

The contribution of u_r to the fringe order is given by equation IV-11:

$$\eta_r = -\frac{r\, u_r}{\lambda L} \qquad \text{(A-27)}$$

When normalized with respect to the fringe order at infinity, from equation A-2, this contribution becomes:

$$\frac{\eta_r}{N_\infty} = -\frac{r\,\frac{u_r}{\lambda L}}{h\nu\,\frac{\sigma_\infty}{\lambda E}}$$

$$\frac{\eta_r}{N_\infty} = -\frac{Er\, u_r}{\nu h L\, \sigma_\infty} \qquad \text{(A-28)}$$

Using equations A-23 and A-25:

$$\frac{\eta_r}{N_\infty} = -\frac{Er}{\nu h L} \quad \frac{a^2}{2E} f(r)$$

$$\frac{\eta_r}{N_\infty} = -\frac{a^2}{2\nu h L} rf(r) \qquad \text{(A-29)}$$

where $f(r)$ is identical to $f_h(r)$ or $f_v(r)$ along the horizontal and vertical axes (equations A-24 and A-26). For $\nu = 0.33$, the functions $[rf_h(r)]$ and $[rf_v(r)]$ are computed in terms of r. The numerical

results are given in table 2. In equation A-29, the coefficient of rf(r) is given by:

$$a = 0.125 \text{ in. } (3.18 \text{ mm})$$

$$h = 0.25 \text{ in. } (6.35 \text{ mm})$$

$$L = 10.7 \text{ in. } (272 \text{ mm})$$

$$\nu = 0.33$$

$$\frac{a^2}{2\nu hL} = 8.85 \times 10^{-3} \qquad \text{(A-30)}$$

Using this result, the normalized values of the fringe order compensation (η_r/N_∞) for radial displacement are also computed and are given in table 2.

2. Around the Circle $r = a\sqrt{2}$

Equations A-22 and A-28 give:

$$\frac{\eta_r}{N_\infty} = -\frac{a^2}{2\nu hL}\, r\, f_c(\theta) \qquad \text{(A-31)}$$

where

$$r\, f_c(\theta) = 2[1 - \nu - (1 + \nu)\cos 2\theta] + [1 + \nu - 4\cos 2\theta] + \frac{1}{2}[(1 + \nu)\cos 2\theta] \qquad \text{(A-32)}$$

$$r\, f_c(\theta) = [2(1 - \nu) + 1 + \nu] - [(2 - \tfrac{1}{2})(1 + \nu) + 4]\cos 2\theta$$

$$r\, f_c(\theta) = (3 - \nu) - \left(\frac{11}{2} + \frac{3\nu}{2}\right)\cos 2\theta \qquad \text{(A-33)}$$

For $\nu = 0.33$, this gives:

$$r\, f_c(\theta) = 2.67 - 6.00 \cos 2\theta \qquad \text{(A-34)}$$

Using also the result of equation A-30, the numerical values of the correction factor are computed in terms of θ, and given in table 3. As expected, comparison of the results of tables 2 and 3 shows that they both give the same results when their entries are the same:

$$\left[\left(\frac{\eta_r}{N_\infty} \right)_{a\sqrt{2}} \right]_{\theta = 0} = \left[\left(\frac{\eta_r}{N_\infty} \right)_h \right]_{r = a\sqrt{2}} = 0.029$$

$$\left[\left(\frac{\eta_r}{N_\infty} \right)_{a\sqrt{2}} \right]_{\theta = \frac{\pi}{2}} = \left[\left(\frac{\eta_r}{N_\infty} \right)_v \right]_{r = a\sqrt{2}} = 0.077$$

APPENDIX III. CALIBRATION OF THE MATERIAL IN TRANSMISSION

This appendix describes the procedure for calibrating the material in transmission, using a four-point bending specimen (figure 29). The bending moment along the central section of the specimen in uniform and is equal to:

$$M = QA \tag{A-35}$$

where Q is the common value of all four loading forces, and A is the distance between the points of application of the forces at each end of the beam. In the central part of the beam, the state of stress is one of pure tension or compression in the x direction. At a point of ordinate y, the stresses are:

$$\begin{aligned} \sigma_y &= \sigma_z = 0 \\ \sigma_x &= My/I \end{aligned} \tag{A-36}$$

I is the moment of inertia of the cross-section of the beam about the plane of symmetry (x Oz):

$$I = \frac{h\,(2C)^3}{12} \tag{A-37}$$

where h and (2C) are the thickness and width of the beam, respectively, equations V-15 and A-36 then give:

$$N = Fh\,\frac{My}{I} = \frac{FhA}{I}\,Qy \tag{A-38}$$

The fringe order is thus seen to be a linear function of both y and the load Q. The fringes should therefore be equidistant straight lines parallel to the x-axis. Their spacing should be inversely proportional to the load Q. This is what is observed indeed. The total number of fringes from the upper to the lower edge of the beam is:

$$N\ (C) - N\ (-C) = \frac{2FhA}{I} \quad QC \tag{A-39}$$

The absolute value of the calibration constant is thus given by:

$$|\ F\ | = \frac{|\ N\ (C) - N\ (-C)\ |}{QC} \quad \frac{I}{2hA} \tag{A-40}$$

Using equation A-37:

$$|\ F\ | = \frac{|\ N\ (C) - N\ (-C)\ |}{Q} \quad \frac{C^2}{3A}$$

Numerically:

$$A = 1.00 \text{ in.} \quad (25.4 \text{ mm})$$

$$C = 0.5 \text{ in.} \quad (12.7 \text{ mm})$$

which gives:

$$F = \frac{|\ N\ (C) - N\ (-C)\ |}{12\ Q} \tag{A-41}$$

A count of the fringe number at various values of the load Q gives the following results:

Q (lbs)	2	4	6	8	10	12	14	16
| N (C) - N (-C) |	1	1.5	2.5	3.5	4	5	6	6.5

The slope of the curve N (C) - N (-C) versus Q is thereby found to be:

$$\frac{\Delta \mid N\ (C) - N\ (-C) \mid}{\Delta Q} = 0.411 \pm 0.0032 \quad \text{fringe/lb.}$$

$$= 0.0924 \pm 0.0072 \quad \text{fringe/N.}$$

Using equation A-41, this gives:

$$\mid F \mid = 0.0342 \pm 0.0027 \quad \text{fringe - in/lb}$$

$$= 0.303 \pm 0.024 \quad \text{fringe - m/N.}$$

VITA

Paul M. de Larminat was born in Rouen, France, the son of Mr. and Mrs. Henri de Larminat on February 29, 1948. He received his primary and secondary education from the "Ecole St. Vincent" in Rennes and "Ecole St. Stanislas" in Nantes, France, and obtained his "Baccalaureat" with honors in 1965. He obtained his Engineer degree from the "Ecole Nationale Superieure de Mecanique" (Nantes) in 1971. He then came to the United States to continue his education in the Department of Mechanical Engineering and Mechanics at Lehigh University. In June 1973, the author was graduated from Lehigh University with the degree of Master of Science in Applied Mechanics. He is currently an associate member of the Sigma Xi society.